UNIVERSITY OF CALIFORNIA
RIVERSIDE

Erythrocyte-Derived Optical Constructs for Biomedical Imaging and Phototherapy

A Dissertation submitted in partial satisfaction
of the requirements for the degree of

Doctor of Philosophy

in

Bioengineering

by

Joshua Michael Burns

December 2018

Dissertation Committee:
Dr. Bahman Anvari, Chairperson
Dr. Meera Nair
Dr. Valentine Vullev

The Dissertation of Joshua Michael Burns is approved:

_____

_____

_____

Committee Chairperson

University of California, Riverside

Acknowledgements

I would like to thank the following individuals:

My beautiful wife, Shaina, for her devotion, patience and support.

My family and friends for their support.

My committee members, Meera Nair and Valentine Vullev, for their guidance and assistance.

My lab members, Ravi, Jenny, Jack, Thompson and Taylor, for the helpful discussions.

My co-authors, Rolf Saager, Boris Majaron, Wangcun Jia and J. Stuart Nelson, for the direction and helpful discussions.

Lastly, I would like to thank my advisor, Bahman Anvari, whose tutelage has developed me as a scientist and communicator. Thank you for your guidance.

My funding sources: National Institute of Health (NIH-1R01-AR068067-01A1), National Science Foundation (NSF-CBET-1509218), University of California Cancer Research Coordinating Committee (5-441894-34912), and UC Riverside Office of Research & Economic Development.

The text of this dissertation, in part or in full, is a reprint of the material as it appears in Nanotechnology 2017, Journal of Biomedical Optics 2018, and ACS Applied Materials and Interfaces 2018.

ABSTRACT OF THE DISSERTATION

Erythrocyte-Derived Optical Constructs for Biomedical Imaging and Phototherapy

by

Joshua Michael Burns

Doctor of Philosophy, Graduate Program in Bioengineering
University of California, Riverside, December 2018
Dr. Bahman Anvari, Chairperson

Light-activated theranostic materials offer a potential platform for biomedical imaging and phototherapeutic applications. We have engineered constructs derived from erythrocytes, which can be doped with the FDA-approved near infrared (NIR) dye, indocyanine green (ICG). We refer to these constructs as **N**IR **e**rythrocyte-mimicking **t**ransducers (NETs) since once activated by NIR light, NETs can transduce the absorbing photons energy to generate heat, emit fluorescence, or mediate production of reactive oxygen species.

In a series of studies, we examined the phototheranostic capabilities of NETs for phototherapy of port wine stains and fluorescence imaging and phototherapy of cancer. Specifically, we measured and sequentially used the optical properties of NETs to theoretically investigate the effectiveness of NETs in mediating photothermal destruction of port wine stain blood vessels. Next, we investigated the phototheranostic capabilities of NETs for fluorescence imaging and photodestruction of SKBR3 breast cancer cells and

subcutaneous xenograft tumors in mice. Lastly, we present ovarian tumor imaging using NETs and spatially modulated illumination.

The optical characterization and mathematical modeling results can be used in guiding the fabrication of NETs with patient-specific optical properties to allow for personalized treatment based on the depth and size of blood vessels and pigmentation of the individual's skin. Whereas, our *in vitro* and *in vivo* results provide support for the effectiveness of NETs as theranostic agents for structured fluorescence imaging and photodestruction of tumors.

Our results demonstrate that for a given NETs diameter, absorption increased over the approximate spectral band of 630–860 nm with increasing ICG concentration and that changing the ICG concentration minimally affected the scattering characteristics. Our simulation results indicated that blood vessels containing micron- or nano-sized NETs and irradiated at 755 nm had higher levels of photothermal damage as compared to blood vessels without NETs irradiated at 585 nm.

In response to continuous wave 808 nm laser irradiation at intensity of 680 mW/cm^2 for 10−15 min, NETs mediated the destruction of cancer cells and tumors in mice through synergistic photochemical and photothermal effects. Our spatially modulated illumination imaging results demonstrated enhanced contrast and through the use of various frequency modulations.

Table of Contents

List of Figures

Chapter 2

Page 51. Figure 3.8 Damage profiles shown in red ($\Omega \geq 1$) for blood vessels containing μNETs, or nNETs at f_{NETs} = 25% with $\mu_{a,BV}$ = 18 mm^{-1}, and located at depths of (a, b) 500, and (c, d) 800 μm below skin surface. Heavy skin pigmentation (f_{mel} = 50%), λ = 755 nm, D_{th} = 3 J/cm^2.

Page 53. Figure 3.9 Three-dimensional rendering of (a) human PWS obtained by OCT, and (b-f) damage profiles to PWS blood vessels. Red regions correspond to values of $\Omega \geq 1$. Panels (b,c) present damage profiles in response to 585 nm laser irradiation without NETs for light (f_{mel} = 4%), and moderate (f_{mel} = 15%) pigmentation levels, respectively. Panels (d-f) present damage profiles in response to 755 nm laser irradiation in presence of μNETs for light (f_{mel} = 4%), moderate (f_{mel} = 15%), and heavy (f_{mel} = 50%) pigmentation levels, respectively. Parameters for patient PWS blood vessels containing μNETs were $\mu_{a,BV}$ = 6 mm^{-1}, f_{NETs} = 10% for panel (d), and $\mu_{a,BV}$ = 18 mm^{-1}, f_{NETs} = 25% for panels (e, f).

Page 55. Figure 3.10 Two-dimensional *x-z* cross section of (a) human PWS obtained by OCT, and (b-f) damage to PWS blood vessels. Red regions correspond to values of $\Omega \geq 1$. Panels (b,c) present damage profiles in response to 585 nm laser irradiation without NETs for light (f_{mel} = 4%), and moderate (f_{mel} = 15%) pigmentation levels, respectively. Panels (d-f) present damage profiles in response to 755 nm laser irradiation in presence of μNETs for light (f_{mel} = 4%), moderate (f_{mel} = 15%), and heavy (f_{mel} = 50%) pigmentation levels, respectively. Parameters for patient PWS blood vessels containing μNETs were $\mu_{a,BV}$ = 6 mm^{-1}, f_{NETs} = 10% for panel (d), and $\mu_{a,BV}$ = 18 mm^{-1}, f_{NETs} = 25% for panels (e, f).

Chapter 4

Page 70. Figure 4.1 Characterization of NETs. (a) Hydrodynamic diameter distribution of NETs as determined by DLS. Circles and error bars (too small to be seen) represent the mean and standard deviations of diameters, respectively (n = 4 measurements). The estimated mean diameter as determined from the lognormal fits (solid curves) is ≈ 85 nm. (b) Absorption spectra of 13 μM free ICG, and NETs ($[ICG_{NETs}] \approx 10$ μM). (c) Normalized fluorescence emission spectra ($\chi(\lambda)$) (see equation 4.1) (circles) and Gaussian fits (solid curves) of 4 μM free ICG and NETs ($[ICG_{NETs}] \approx 2$ μM) in response to photo-excitation at 720 ± 2.5 nm. Solvent used in spectral recordings was 310 mOsm PBS.

Page 73. Figure 4.2 Photostability and $^1O_2$ generation of NETs in solution. (a) Absorption spectra of 22 μM free ICG, and NETs ($[ICG_{NETs}] \approx 18$ μM) before and after 808 nm laser irradiation (I_o = 680 mW/cm^2) for 5, 10, and 15 minutes. (b) Normalized 808 nm absorbance values for ICG and NETs as a function of 808 nm laser irradiation time. (c) Normalized 411 nm absorbance values for solutions containing 10 μM DPBF without, or

with 11 μM ICG or NETs ([ICG_{NETs}] ≈ 18 μM) as a function of 808 nm laser irradiation time. Data points and error bars in panel (c) represent the mean and SDs for n = 4 samples.

Page 74. Figure 4.3 Uptake of NETs by SKBR3 cancer cells. (a) Merged bright-field and fluorescent images of SKBR3 cancer cells following three hours of incubation at 37 °C with PBS, 44 μM free ICG or NETs ([ICG_{NETs}] ≈ 36 μM). Images are falsely colored. Red channel: NIR emission due to ICG; Gray channel: bright-field. (b) Uptake analysis of SKBR3 cells by flow cytometry. Geometric mean fluorescence intensity (n = 3 different samples) (**) $p < 0.01$. (c) Laser scanning confocal fluorescent images of a SKBR3 cell following three hours of incubation at 37 °C with NETs. Images are falsely colored. Blue channel: DAPI; Green channel: Lysotracker; Red channel: NIR emission due to ICG from NETs.

Page 76. Figure 4.4 Photo-destruction of SKBR3 cancer cell in vitro. (a) Fluorescent images of SKBR3 cancer cells incubated with PBS (negative control), 176 μM free ICG (positive control), and NETs ([ICGNETs] ≈ 144 μM) for three hours at 37°C and followed by 808 nm laser irradiation at I_o = 680 mW/cm^2 for 15 minutes. Live cells were identified by the Calcein AM stain, and falsely colored in green. Dead cells in response to laser irradiation were identified using the Ethidium homodimer-1 stain, and falsely colored in red. (b) Percentage viability of SKBR3 cells as a function of incubation agent. (c) Percentage viability of SKBR3 cells as a function of [ICG_{NETs}]. In panels (b) and (c), statistically significant differences are indicated as (*) $p < 0.05$ and (***) $p < 0.001$ (n = 3 samples for each treatment).

Page 78. Figure 4.5 Detection of ROS generation by cell imaging. We present merged bright-field and DCF fluorescence images of SKBR3 cancer cells incubated with PBS, 44 μM free ICG, or NETs ([ICG_{NETs}] ≈ 36 μM) for three hours and subsequently irradiated at 808 nm for 15 minutes at I_o = 680 mW/cm^2. Images correspond to (a) without and (b) and with application of $^1O_2$ quencher, sodium azide. Images are falsely colored. Gray channel: bright-field. Green channel: fluorescence emission from DCF.

Page 80. Figure 4.6 NIR fluorescence imaging and photo-destruction of xenograft tumors in mice. (a) NIR fluorescence images of tumors extracted 24 hours after tail injection of PBS (top panel), and NETs ([ICG_{NETs}] ≈ 980 μM) (bottom panel). Scale bar on the right corresponds to fluorescent intensity (photo-excitation at 700 ± 30 nm, and emission > 810 nm collected). (b) Temperature rise as a function of laser irradiation time as measured by a thermocouple needle probe placed ≈ 1 mm below skin surface and ≈ 2 mm outside the irradiated spot. (c) Fluorescent images of sectioned tumors by immunostaining using FITC-labeled Caspase-3 antibody. (d) Fluorescence emission intensity associated with FITC-labeled Caspase-3 antibody as the apoptosis indicator following laser irradiation. (e) Estimated relative change in tumor volumes (V) of non-orthotopic xenograft tumors in mice with respect to the volumes at time zero (V_o). Time zero is with respect to the day of laser irradiation. Mice were injected via the tail vein with either 100 μL of PBS, or NETs ([ICG_{NETs}] ≈ 980 μM). Laser Irradiation was done 24 hours

post injection of NETs or PBS. Irradiation parameters were: 808 nm; spot size = 9 mm; irradiation time = 10 min, I_o = 680 mW/cm^2. In panels (b) and (e), n = 4 mice for each administered agent. In panel (d), n = 5 images from different sections of same tumors for each administered agent (statistically significant difference at (**) $p < 0.01$).

Chapter 5

Page 91. Figure 5.1 Reflectance and fluorescence spatial frequency imaging system.

Page 99. Figure 5.2 (a) Hydrodynamic diameter distribution of NETs as determined by DLS. Squares and error bars represent mean and SD of diameters, respectively (n = 8 measurements). The estimated mean diameter as determined from log-normal fits (solid curves) was ≈ 101 nm. (b) Absorption spectrum of NETs. (c) Fluorescence spectrum of NETs in response to photo-excitation at 710 nm. Dilution factor was 1:200 for both absorption and $\chi(\lambda)$ measurements. ICG concentration used in the loading buffer to fabricate these NETs was 25 μM.

Page 100. Figure 5.3 Normalized fluence profiles as a function of depth and lateral location for mean optical properties of the chicken breast phantom (μ_a = 0.028 mm^{-1}, μ_s' = 0.179 mm^{-1}) and spatial frequencies of (a) 0, (b) 0.05, (c) 0.10, (d) 0.20 and (e) 0.40 mm^{-1}. (f) Normalized fluence profiles as a function of depth for greatest intensity of each spatial frequency.

Page 102. Figure 5.4 (a) Fluorescence intensity map of a 4 mm diameter tumor phantom at depth of 2.5 mm below the surface in response to illumination at spatial modulation frequencies of 0, 0.05, 0.10, 0.20 and 0.40 mm^{-1}. Concentration of NETs within the tumor phantom was 0.5%. Scale bar at the right corresponds to the intensity of the demodulated images. White scale bar on image corresponds to 5 mm. (b) Tumor-phantom contrast for spatial modulation frequencies of 0, 0.05, 0.10, 0.20 and 0.40 mm^{-1}.

Page 104. Figure 5.5 Representative color images and normalized fluorescent intensities for closed body (top panel, washed open body mouse (middle panel) and excised organs (bottom panel) with spatial frequencies of 0 and 0.2 mm^{-1}. Scale bar in the middle corresponds to normalized intensity of images for 0 or 0.2 mm^{-1}. Arrows indicate tumor locations. White scale bar on image corresponds to 10 mm.

Page 105. Figure 5.6 Representative color images and normalized fluorescent intensities for washed open body mouse for mice without tumors and with spatial frequencies of 0 and 0.2 mm^{-1}. Scale bar in the middle corresponds to normalized intensity of images for 0 or 0.2 mm^{-1}. White scale bar on image corresponds to 10 mm.

List of Tables

Chapter 3

Chapter 1

Introduction

Light-activated theranostic materials present a platform for potential clinical optical imaging and phototherapeutic applications.[1–6] Materials that are activated by near infrared (NIR) excitation wavelengths (λ) are especially advantageous since relatively deep (on the order of ≈ 3–5 cm) optical imaging and phototherapy can be achieved over this spectral band. Todate, indocyanine green (ICG) remains the only NIR chromophore approved by United Sates Food and Drug Administration (FDA) for specific clinical applications including ophthalmic angiography, cardiocirculatory measurements, assessment of hepatic function, and blood flow evaluation.[7–9] ICG has also been investigated for potential applications ranging from sentinel lymph node mapping in patients with different types of cancer to imaging intracranial aneurysm and cerebral arteriovenous malformations.[10–17] Additionally, ICG has been investigated as a photosensitizer for photodynamic therapy (PDT) of choroidal melanomas, and as a photothermal agent for treatment of port wine stains (PWSs).[18–20]

Despite its wide utility in clinical medicine, ICG's major drawbacks are its non-specificity and short lifetime within circulation (half-life on the order of 2–4 min). Encapsulation of ICG within various constructs, including micelles, liposomes, silica, and synthetic polymers has been investigated as an approach to increase circulation time of ICG and reduce its non-specific interactions.[21–31]

More recently, mammalian cells such as erythrocytes, lymphocytes, and macrophages, or constructs derived from them, are receiving increased attention as new

types of platforms for the delivery of therapeutic or imaging agents.[32–37] Use of erythrocytes is particularly attractive due to their naturally long circulation time (≈ 90–120 days), attributed to the presence of 'self-marker' membrane proteins.[38,39] Hemoglobin-depleted red blood cells (RBCs), erythrocyte ghosts (EGs), have been doped with iron oxide and gold nanoparticles to enhance contrast in magnetic resonance imaging and dynamic x-ray imaging of blood flow.[40–43] ICG-loaded EGs have been used to characterize the movement of erythrocytes in choriocapillaries and retinal capillaries of rabbits and monkeys.[44] In addition to imaging, erythrocytes have been doped with fluorescein isothiocyanate to create biosensors for monitoring changes in plasma analytes and extracellular pH.[45,46]

We recently reported the first demonstration of successful engineering of nano-sized vesicles derived from erythrocytes loaded with ICG for fluorescence imaging and photothermal destruction of human cells.[47] We refer to these constructs as NIR erythrocyte-mimicking transducers (NETs). A key advantage of erythrocyte-derived constructs as compared to liposomal particles is that the former can potentially have extended circulation time due to preserved membrane proteins that prevent phagocytosis by immune cells. In a previous study,[48] we demonstrated that CD47, a membrane glycoprotein, which impedes phagocytosis,[38,39] remains on the surface of NETs. Other investigators have reported that polymeric nano-constructs, coated with erythrocyte-derived membranes, were retained in mice blood for three days with circulation half-life of nearly 40 h.[49]

A particular feature of NETs is that their diameter (d_{NETs}) can be tuned to various sizes by appropriate mechanical manipulation procedures, and their ICG content can be

changed during the fabrication process. These parameters are important in that d_{NETs} can influence the NETs biodistribution dynamics, and in combination with the ICG content, they will determine the optical properties of NETs. Such properties are ultimately important in selection of the appropriate light dosimetry parameters for an intended light-based biomedical application, as well as the development of mathematical models to predict the optical response of biological tissues containing NETs.

Chapter 2 presents the first report on the optical properties of NETs as a function of their diameters, and ICG concentration utilized in fabricating them. Specifically, we examine micron- and nano-sized NETs formed without and with mechanical extrusion methods, respectively. The nano-sized NETs have relevance to cancer imaging and phototherapy. Specifically, the enhanced permeability and retention (EPR) effect of tumors, induced by leaky tumor vasculature and impaired lymphatic drainage, may provide the basis for the delivery of NETs into tumors.[50–52] The effects of changes in NETs diameter from micron to nano scale are relevant to imaging and photothermal destruction capability of vascular abnormalities such as those found in PWS lesions in skin, and subsequent selection of optimal imaging and irradiation parameters in this dermatological application. Finally, using a Monte Carlo simulation approach, we demonstrate the effects of NETs diameter and ICG concentration on the resulting light distribution within a simulated blood vessel, a biologically relevant target of light in various clinical applications.

In chapter 3, we use resulting optical properties (absorption coefficient (μ_a) and reduced scattering coefficient (μ_s')) of these NETs from chapter 2 to development a mathematical model for phototherapy of PWSs. As a first step towards potential application

of NETs in phototherapy of PWSs, we analyze in dedicated numerical simulations the photothermal response of blood vessels containing NETs, and compare the results with those obtained with the current treatment approach. These results can be used to identify the optimum formulation of NETs and appropriate irradiation parameters for NIR photothermal treatment of PWSs.

Chapter 4 investigates the phototheranostic capabilities of NETs for near infrared fluorescence imaging and photodestruction of cancer cells and subcutaneous xenograft tumors in mice. We demonstrate that NETs remain available within tumors at 24 hours post intravenous injection, and mediate the destruction of cancer cells and tumors through synergistic photochemical and photothermal effects in response to continuous wave laser irradiation. We report for the first time that NETs are localized to cancer cells lysosomes, and upon photo-excitation can induce Caspase-3 activation, leading to tumor apoptosis.

Lastly, Chapter 5 focuses on a particular wide-field optical imaging method of interest is spatial-modulated illumination (SMI). SMI uses structured sinusoidal illumination patterns of varying spatial frequencies projected on the tissue and measures attenuated intensity of the spatial patterns through optical sensors on pixel by pixel basis. SMI has been used to estimate the 2-D optical properties of tissues,[53,54] and quantify depth-resolved Protoporphyrin IX concentrations from preclinical glioma models using fluorescent imaging.[55,56] We present the first demonstration of the use of NETs in conjunction with SMI to image tumors intraperitoneally implanted in mice. Our results showed high accumulation of NETs within tumors after 24 hours post-injection. We showed enhanced contrast for NETs-mediated fluorescence imaging with frequency

modulations over conventional non-modulated illumination. Lastly, we demonstrated wide-field estimation of ICG concentration delivered by NETs and compare those values to quantitative organ analysis.

Chapter 2

Optical Properties of Biomimetic Probes Engineered from Erythrocytes

Abstract

Light-activated theranostic materials offer a potential platform for optical imaging and phototherapeutic applications. We have engineered constructs derived from erythrocytes, which can be doped with the FDA-approved NIR chromophore, ICG. We refer to these constructs as NETs. Herein, we investigated the effects of changing the NETs mean diameter from micron- (≈4 μm) to nano- (≈90 nm) scale, and the ICG concentration utilized in the fabrication of NETs from 5 to 20 μM on the resulting absorption and scattering characteristics of the NETs. Our approach consisted of integrating sphere-based measurements of light transmittance and reflectance, and subsequent utilization of these measurements in an inverse adding-doubling algorithm to estimate the μ_a and μ_s' of these NETs. For a given NETs diameter, values of μ_a increased over the approximate spectral band of 630–860 nm with increasing ICG concentration. Micron-sized NETs produced the highest peak value of μ_a when using ICG concentrations of 10 and 20 μM, and showed increased values of μ_s' as compared to nano-sized NETs. Spectral profiles of μ_s' for these NETs showed a trend consistent with Mie scattering behavior for spherical objects. For all NETs investigated, changing the ICG concentration minimally affected the scattering characteristics. A Monte Carlo-based model of light distribution showed that the presence of these NETs enhanced the fluence levels within simulated blood vessels. These results provide important data towards determining the appropriate light dosimetry parameters for an intended light-based biomedical application of NETs.

Introduction

Light-activated theranostic materials present a platform for potential clinical optical imaging and phototherapeutic applications.[1–6] Materials that are activated by NIR excitation λ are especially advantageous since relatively deep (on the order of ≈3–5 cm) optical imaging and phototherapy can be achieved over this spectral band. Todate, ICG remains the only NIR chromophore approved by United States FDA for specific clinical applications including ophthalmic angiography, cardiocirculatory measurements, assessment of hepatic function, and blood flow evaluation.[7–9] ICG has also been investigated for potential applications ranging from sentinel lymph node mapping in patients with different types of cancer to imaging intracranial aneurysm and cerebral arteriovenous malformations.[10–17] Additionally, ICG has been investigated as a photosensitizer for PDT of choroidal melanomas, and as a photothermal agent for treatment of PWSs.[18–20]

Despite its wide utility in clinical medicine, ICG's major drawbacks are its non-specificity and short lifetime within circulation (half-life on the order of 2–4 min). Encapsulation of ICG within various constructs, including micelles, liposomes, silica, and synthetic polymers has been investigated as an approach to increase circulation time of ICG and reduce its non-specific interactions.[21–31]

More recently, mammalian cells such as erythrocytes, lymphocytes, and macrophages, or constructs derived from them, are receiving increased attention as new types of platforms for the delivery of therapeutic or imaging agents.[32–37] Use of erythrocytes is particularly attractive due to their naturally long circulation time (≈90–120

days), attributed to the presence of 'self-marker' membrane proteins.[38,39] Hemoglobin-depleted RBCs, EGs, have been doped with iron oxide and gold nanoparticles to enhance contrast in magnetic resonance imaging and dynamic x-ray imaging of blood flow.[40–43] ICG-loaded EGs have been used to characterize the movement of erythrocytes in choriocapillaries and retinal capillaries of rabbits and monkeys.[44] In addition to imaging, erythrocytes have been doped with fluorescein isothiocyanate to create biosensors for monitoring changes in plasma analytes and extracellular pH.[45,46]

We recently reported the first demonstration of successful engineering of nano-sized vesicles derived from erythrocytes loaded with ICG for fluorescence imaging and photothermal destruction of human cells.[47] We refer to these constructs as NETs. A key advantage of erythrocyte-derived constructs as compared to liposomal particles is that the former can potentially have extended circulation time due to preserved membrane proteins that prevent phagocytosis by immune cells. In a previous study,[48] we demonstrated that CD47, a membrane glycoprotein, which impedes phagocytosis,[38,39] remains on the surface of NETs. Other investigators have reported that polymeric nano-constructs, coated with erythrocyte-derived membranes, were retained in mice blood for three days with circulation half-life of nearly 40 h.[49]

A particular feature of NETs is that d_{NETs} can be tuned to various sizes by appropriate mechanical manipulation procedures, and their ICG content can be changed during the fabrication process. These parameters are important in that d_{NETs} can influence the NETs biodistribution dynamics, and in combination with the ICG content, they will determine the optical properties of NETs. Such properties are ultimately important in

selection of the appropriate light dosimetry parameters for an intended light-based biomedical application, as well as the development of mathematical models to predict the optical response of biological tissues containing NETs.

Herein, we present the first report on the optical properties of NETs as a function of their diameters, and ICG concentration utilized in fabricating them. Specifically, we examine micron- and nano-sized NETs formed without and with mechanical extrusion methods, respectively. The nano-sized NETs have relevance to cancer imaging and phototherapy. Specifically, the EPR effect of tumors, induced by leaky tumor vasculature and impaired lymphatic drainage, may provide the basis for the delivery of NETs into tumors.[50–52] The effects of changes in NETs diameter from micron to nano scale are relevant to imaging and photothermal destruction capability of vascular abnormalities such as those found in PWS lesions in skin, and subsequent selection of optimal imaging and irradiation parameters in this dermatological application. Finally, using a Monte Carlo simulation approach, we demonstrate the effects of NETs diameter and ICG concentration on the resulting light distribution within a simulated blood vessel, a biologically relevant target of light in various clinical applications.

Methods and Materials

Fabrication of NETs

Whole bovine blood was centrifuged at 1300 relative centrifugal force (rcf) for five minutes at 4 °C to separate the erythrocytes from the plasma and buffy coat. Isolated erythrocytes were then washed in 1 ml of cold 1X phosphate buffered saline (PBS) (310 mOsm, pH 8), and centrifuged at 1300 rcf for five minutes at 4 °C. Packed erythrocytes were transferred

to an ultracentrifuge tube and suspended in 50 ml of hypotonic buffer (0.5X PBS, 155 mOsm, pH 8) and incubated at 4 °C for 30 min. Further hemoglobin depletion was not performed because of the possible deleterious effects on erythrocyte shape with more aggressive hypotonic treatments.

EGs, formed by hypotonic treatment of RBCs, were resuspended in 1X PBS, and separated into three sample sets. EGs in Set I were extruded 40 times through 400 nm polycarbonate porous membranes (Nuclepore Track-Etched Membranes, Whatman, Florham Park, NJ) (single extrusion method). EGs in Set II were extruded through 40 times 400 nm polycarbonate membranes, followed by 40 more extrusions through 100 nm polycarbonate membranes (double extrusion method). EGs in set III were not extruded. Extrusion of EGs in sets I and II resulted in formation of spherical nano-sized particles through cleavage and reformation of the membrane,[57,58] whereas EGs in set III remained micron-sized. The filters used for extrusion are cylindrical with nano-sized diameters, forming narrow and long tubes (tube length > tube diameter). Similar to lipid vesicles, when spherical EGs (or RBCs) are extruded through these filters, they likely acquire cylindrical shapes and break into smaller structures when they reach the end of the filters, and reassemble into nano-sized vesicles.[57] The bilayer of the EG ruptures when the induced membrane tension due to applied pressure exceeds the lysis tension.[58] To ensure that nearly the same amount of erythrocytes derived membranes were present among the samples in all three sets, extruded samples (sets I and II) were diluted appropriately so that the absorbance value at 280 nm (associated with membrane proteins) in these samples matched the value for non-extruded samples (set III). Therefore, with the same amount of membrane

available, we expect that there would be a smaller number of micron-sized NETs than nanosized NETs.

EGs in all sets were separated into aliquots, and incubated with 3 ml of hypotonic buffer ($Na_2HPO_4/Na_2H_2PO_4$, 140 mOsm, pH 5.8). To this solution, we added 3 ml of ICG dissolved in water at different concentrations so that the final concentrations of ICG in the loading solvent were 0, 5, 10, and 20 μM. Suspensions were then incubated for five minutes at 4 °C in dark, centrifuged at 25 000 rcf for 20 min, and washed twice in 1X PBS to remove any non-encapsulated ICG. ICG-loaded EGs (NETs) were re-suspended in cold 1X PBS buffer solution. Prior to characterization of optical properties, NETs samples were centrifuged and supernatant removed.

Characterization of NETs

Phase contrast images of un-extruded NETs (set III) were obtained using a microscope (Nikon Ti-Eclipse, Melville, NY), and an electron multiplier gained CCD camera (Quant EM-CCD, Hamamatsu, Japan) at integration time of 0.1 s and gain of 1.0. We estimated the diameter of un-extruded NETs using ImageJ software, and determined the mean and standard deviation (SD) of the population sample. The hydrodynamic diameters of nano-sized NETs (sets I and II) suspended in 1X PBS were measured by dynamic light scattering (DLS) (Zetasizer NanoZS90, Malvern Instruments Ltd, Malvern, UK).

We used an integrating sphere (4P-GPS-033-SL, Labsphere, North Sutton, NH) to measure the percent transmittance (*T*) and reflectance (*R*) from the samples (**Figure 2.1**). Visible-NIR (from 400 to 1000 nm) light from a broadband source (HL2000 20W Quartz-Tungsten-Halogen lamp, Ocean Optics, Dunedin, FL) was collimated, and an aperture

mask used to create a 4 mm diameter beam. A 400 micron fiber collected the transmitted or reflected light at the detector port, placed at 90° from the entrance or exit ports, respectively, and delivered it to a spectrometer (Prime-X, B&W Tek, Newark, DE).

Measurements of *T* and *R* for whole blood were obtained from non-diluted samples, and samples diluted with 1X PBS by 100 times. The purpose of diluting the blood was to enhance *T* for $\lambda < 604$ nm since the detector was unable to resolve the signature absorption peaks of oxyhemoglobin over the 400–600 nm spectral band. Since the reported range of hematocrit (hct) for bovine blood is 36.9 ± 4.2%,[59] we assumed an average value of 37% hct for the blood samples used in this study for the measurements of *T* and *R*.

Blood, or NETs samples were placed on the entrance port with the exit port closed for *T* measurements (**Figure 2.1a**), and on the open exit port for the *R* measurements (**Figure 2.1b**). To compare *T* and *R* among different sets of NETs, in our analysis we normalized the measurements of *T* to the values at 740 and 806 nm for NETs formed by double extrusion and with 5 μM ICG in the loading buffer. In our analysis of *R*, we normalized the measurements to those at 500 nm for unextruded EGs.

Non-normalized measurements of *T* and *R*, along with an assumed values of refractive index (n) (1.33), and estimates of the anisotropy factor (*g*) for NETs were subsequently used as input parameters into an inverse adding-doubling (IAD) algorithm.[60] The IAD algorithm repeatedly guesses and checks solutions for the radiative transport equation until it determines values of absorption coefficient (μ_a (mm^{-1})) and reduced scattering coefficient (μ_s' (mm^{-1})) that fit the measured data *T* and *R*.[60] The μ_s' is related to the scattering coefficient (μ_s) and *g* (the mean cosine of the scattering function) as:

$$\mu_s' = \mu_s\left(1-g\right) \tag{2.1}$$

Range of g is from −1 to 1. When g = 1, the scattering is completely in the forward direction, and μ_s' = 0. In the case of isotropic scattering (g = 0), μ_s' = μ_s. For example, the reported value of g for skin is ≈0.5 at 400 nm, and increases to >0.9 for wavelengths greater than 800 nm.[61] For mammalian cells, the reported g value is ≈0.95 in the spectral band of 425–900 nm.[61] Therefore, to estimate μ_s' for whole blood, we used g = 0.95.

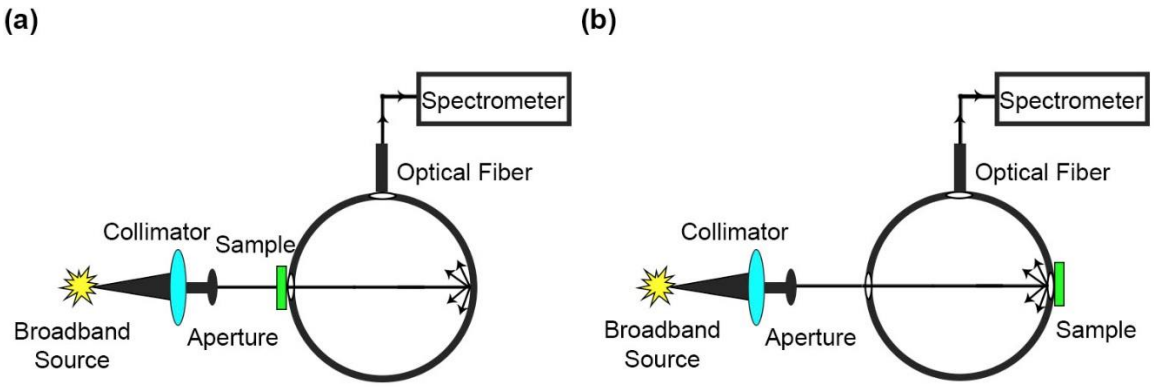

Figure 2.1 Schematic of integrating sphere-based measurements of (a) transmittance and (b) reflectance for whole blood, EGs, and NET samples.

For NETs, g value was estimated using a Mie Simulator (Virtual Photonics Initiative, Irvine, CA) based on measurements of the NETs diameter.[62] Specifically, the g values were estimated as 0.99 for the micron-sized NET based on measurements of diameter by phase contrast imaging (**Figure 2.2a**), 0.66 for nano-sized NETs formed by single extrusion, and 0.55 for nano-sized NETs formed by double extrusion, based on measurements of the diameter by DLS. We used these g values and the measured values of

T and *R* in the IAD algorithm to obtain spectrally-dependent estimates of μ_s' for whole blood, EGs, micron-sized NETs formed without extrusion, and nano-sized NETs formed by single or double extrusions at ICG loading concentrations in the range of 5–20 μM.

We used a general analytical expression[61] that takes into account contributions by Rayleigh and Mie types of scattering for spherical objects to fit the estimated μ_s' spectra:

$$\mu_s'(\lambda) = A'\left[f_{\text{Rayleigh}}\left(\frac{\lambda}{\lambda_o}\right)^{-4} + \left(f_{\text{Rayleigh}}\right)\left(\frac{\lambda}{\lambda_o}\right)^{-m} \right] \tag{2.2}$$

where $A' = \mu_s'(\lambda_o)$, f_{Rayleigh} is the fractional contribution due to Rayleigh scattering, λ_o is a reference wavelength, and m is the power law exponent (scattering power) related to the Mie scattering component. We used λ_o = 500 nm since at this wavelength there is no absorption by NETs that may originate from either hemoglobin or ICG, and therefore, optical attenuation for NETs is completely due to scattering. Spectrally-dependent values of μ_s' within the spectral range of 437–635 nm were fitted by Igor Pro (Wavemetrics, Lake Oswego, OR) and extrapolated for $\lambda < 437$ and $\lambda > 635$ based on **equation 2.2**.

Light-distribution model

The Monte Carlo light-distribution model used in this study was developed by Majaron et al [63,64]. To represent μ_a and μ_s' of human whole blood with 45% hct,[61,65] we scaled our estimates of μ_a and μ_s' associated with assumed value of 37% hct as follows:

$$\mu_a(45\%\ \text{hct}) = \mu_a(37\%\ \text{hct})\left(\frac{0.45}{0.37}\right) \tag{2.3}$$

$$\mu_s'(45\%\ \text{hct}) = \mu_s'(37\%\ \text{hct})\left(\frac{0.45}{0.37}\right) \tag{2.4}$$

We simulated 1,000,000 photons delivered to a 500 μm diameter blood vessel containing either blood at 45% hct without any added NETs, or with added nano- or micron-sized NETs (sets I–III). We note that this simulation is not representative of a skin with PWS. A PWS simulation would require additional features including a multi-layered geometry to account for the presence of epidermis and additional blood vessels. Herein, we only seek to investigate the relative optical response of a blood vessel with and without NETs. We used the scaled optical properties of blood (**equations 2.3** and **2.4**), and NETs obtained in this study. We assumed effective optical properties of the simulated blood vessel as:

$$\mu_{a\_BV} = f_{blood}\mu_{a\_blood}(45\%\ hct) + (1 - f_{NETs})\mu_{a\_NETs} \quad (2.5)$$

$$\mu'_{s\_BV} = f_{blood}\mu'_{s\_blood}(45\%\ hct) + (1 - f_{NETs})\mu'_{s\_NETs} \quad (2.6)$$

where μ_{a_BV} is the effective absorption coefficient of the blood vessel, f_{blood} and f_{NETs} are the respective fractions of blood and NETs in the blood vessel ($f_{blood} = f_{NETs} = 50\%$), μ_{a_blood} (45% hct) and μ_{a_NETs} are the respective absorption coefficients of blood with 45% hct and NETs, and $\mu_s{}'_{\_BV}$ (45% hct) and $\mu_s{}'_{\_NETs}$ are the effective reduced scattering coefficient of the blood vessel and NETs, respectively. We simulated a flat-top incident laser beam at 806 nm corresponding to peak absorption wavelength associated with the monomeric form of ICG in NETs. The beam delivered fluence of 10 J/cm^2, and illuminated a 100 μm diameter spot on the surface.

Results and Discussion

Size distribution of NETs

The average ± SD diameter for micron-sized NETs, formed without mechanical extrusion, was 4.31 ± 0.69 μm (n = 28) (**Figure 2.2a**). This mean value is smaller than the reported average diameter of bovine RBCs (5.05 μm), but within the reported SD (±0.16 μm).[66] The hydrodynamic peak (d_{peak}) diameters, as determined by DLS technique, were ≈164 nm (polydispersity index (PDI) = 0.10) and 91 nm (PDI = 0.07) for the populations of nano-sized NETs formed by single and double extrusions respectively (**Figure 2.2b**). We used lognormal fits to estimate the mean (d_{mean}) ± SD diameters of single extruded (160 ± 2 nm), and double extruded (92 ± 1 nm) NETs. The population of the nano-sized NETs is considered to be monodispersed since the respective PDI values are equal to, or less than 0.1.[67]

Since particles with diameters <200 nm are more effective for extravasation into tumors through the EPR effect,[68] nano-sized NETs may prove as effective nano-vesicles with light-based theranostic capabilities for fluorescence imaging and photo-destruction of tumors. Further molecular specificity of NETs can be achieved by functionalizing their surface with appropriate targeting moieties such as antibodies.[48]

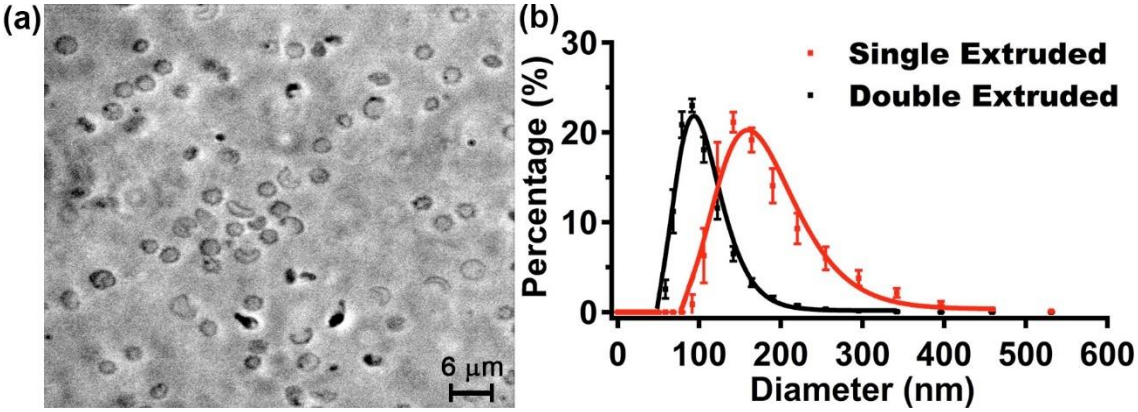

Figure 2.2 (a) Phase contrast image of micron-sized NETs formed without extrusion, and (b) hydrodynamic diameter distributions of nano-sized NETs formed by single or double extrusions, as determined by DLS method. The respective ranges of the measured diameters, based on DLS, for NETs fabricated by single and double extrusion methods were ≈91–396 nm, and 59–190 nm. We present the mean and standard deviation of the measurements of these samples (n = 6), represented as circles and error bars, respectively. The estimated mean diameters as determined from the lognormal fits (solid curves) were ≈160 nm and 92 nm for NETs formed by single and double extrusion methods, respectively.

Transmittance and Reflectance Measurements

The measurement results for *T* and *R* for micron-sized NETs formed without extrusion (d_{mean} ≈ 4.31 μm), and nano-sized NETs formed by single (d_{mean} ≈ 160 nm) or double extrusions (d_{mean} ≈ 92 nm) using ICG loading concentrations in the range of 5–20 μM are shown in **Figure 2.3**. We also present the results for whole blood, and EGs not containing ICG in these figures.

The non-diluted blood sample showed less than 3% transmission over the approximate spectral band of 400–610 nm (**Figure 2.3a**), indicative of the relatively high light absorption by hemoglobin in this wavelength range. Therefore, this sample was diluted by 100 times to resolve transmission changes over this spectral band. Minimum values of *T* at 420, 542, and 577 nm for the diluted blood sample (**Figure 2.3a**) are indicative of hemoglobin absorption at these wavelengths. We attribute the relatively high

values of T ($\lambda > 610$ nm) for the diluted sample to reduced number of erythrocytes and the overall lower absorption by hemoglobin at these wavelengths. The nearly constant value of T ($\lambda > 610$ nm) is suggestive of the Fresnel reflection at the interface of the sample solution and the cuvette.

It is important to note that the values of T for all sets of NETs nearly overlapped with those for the EGs except over the approximate bands of 400–440 nm and 630–865 nm, indicative of successful loading of ICG into the NETs. For EGs, T spectra did not show a decreasing trend over the 630–865 nm spectral band, consistent with the fact that these particles did not contain ICG. For the three sets of NETs having d_{mean} values in the range of ≈ 92 nm–4.31 μm, as the concentration of ICG in the loading buffer increased, there was an overall trend in T values becoming lower over the 630–865 nm spectral band (**Figure 2.3c, e, g**), indicating that higher concentrations of ICG were loaded into the particles. Independent of the d_{mean} value, minimum values of T occurred between 803 and 806 nm, which corresponds to peak absorption wavelength associated with monomeric form of ICG.

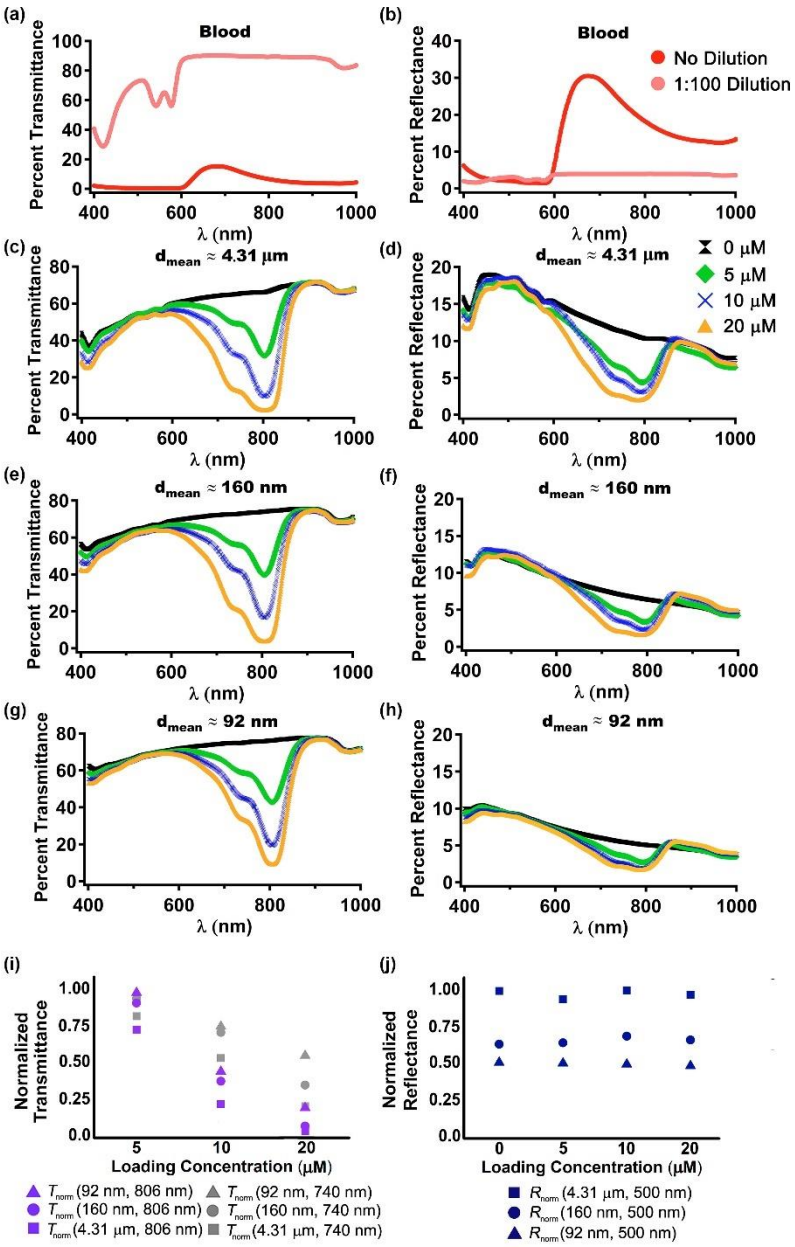

Figure 2.3 Spectrally dependent values of percent (a) transmittance, and (b) reflectance (b) for whole bovine blood samples without dilution, and diluted 100 times by adding 1X PBS (≈310 mOsm). Spectra of percent (c, e, g) transmittance, and (d, f, h) reflectance for micron-sized NETs formed (c, d) without extrusion, or by (e, f) single or (g, h) double extrusions using various ICG concentrations. Measurements were obtained with NETs suspended in 1X PBS (≈310 mOsm). The legend labels indicate the ICG concentration levels in the loading buffer. In panel (i), transmittance measurements are normalized to the values at 740 nm and 806 nm for 92 nm NETs formed using 5 μM ICG in the loading buffer. In panel (j), reflectance measurements are normalized to the value at 500 nm (spectral peak) for EGs.

We attribute the shoulder in the approximate spectral range of 720–760 nm (albeit without a distinct secondary peak) to the H-like aggregate forms of ICGs within the NETs.[47,69] Aggregation-induced split in the excited electronic state that results from a stacked (sandwich-like) arrangement of the individual chromophores, and their transition dipole moments constitute H-aggregation.[70–72] In H-aggregates, transitions to the upper level of the split excited state are allowed, resulting in a blue spectral shift.

With increased ICG concentration, the *T* value in the range of 720–760 nm decreased for the three sets of NETs, suggesting higher levels of ICG in the aggregated form within the NETs. For example, for NETs fabricated using ICG concentration of 5 μM in the loading buffer, *T* values associated with the H-like aggregate form of ICG decreased by about 10% as d_{mean} of NETs was increased from ≈ 92 nm to 4.31 μm (**Figure 2.3c, e, g**). Collectively, these results indicate that more ICG can be loaded into the larger diameter NETs, and that the relative fraction of monomeric form of ICG is consistently higher than the H-like aggregate forms when using ICG in the range of 5–20 μM to fabricate these three sets of NETs.

We summarize some of the salient features of *T* for NETs in **Figure 2.3i** where the measurements are normalized to the values at 740 nm and 806 nm for 92 nm NETs formed using 5 μM ICG in the loading buffer. At a given ICG concentration, as the NETs diameter became larger, normalized transmittance values (T_{norm}) becomes smaller. For both micron and nano-sized NETs, T_{norm} values decreased with increasing ICG concentration.

For the non-diluted whole blood sample, the relatively low values of R (<6%) in the approximate spectral range of 400–600 nm (**Figure 2.3b**) are likely due to loss of photons to absorption by hemoglobin in this spectral band. For wavelengths greater than the spectral peak at 674 nm, R values decreased, suggestive of decreased light absorption by hemoglobin, and decreased scattering by erythrocytes. For the whole blood sample diluted by 100 times, the R values were less than 4% over the entire spectral band investigated (400–1000 nm), suggesting that there were relatively fewer scattering objects (e.g., erythrocytes) within the sample to make sufficient back-scattered photons available for detection as compared with the non-diluted sample.

For the three sets of NETs, with increased ICG concentration in the loading buffer, there was an overall trend in R values becoming smaller over the approximate spectral band of 600–795 nm (**Figure 2.3d, f, h**). The peak R values were at 453 nm, 444 nm and 440 nm, corresponding to NETs with $d_{mean} \approx 4.31$ μm, 160 nm and 92 nm respectively. For a given d_{mean}, the peak R values varied only by about 0.9%— 1.3% as the ICG concentration increased from 5 to 20 μM. For all ICG concentrations used in fabricating these NETs, peak R values for micron-sized NETs ($d_{mean} \approx 4.31$ μm) were consistently higher by approximately 8% than those for nano-sized NETs with $d_{mean} \approx 92$ nm. This result suggests that increased levels of ICG used during fabrication do not contribute much to the reflectance from the particles at the peak reflectance wavelengths (outside the ICG absorption band), and the higher R values associated with the larger NETs are likely due to the enhanced back-scattering that results from increased diameter of the particles.

In **Figure 2.3j**, we show a summary of R measurements for EGs. At this wavelength, there are minimal contributions from absorption by hemoglobin and ICG, and therefore, R can be mostly contributed to back-scattering by the particles. At a given ICG concentration, normalized reflectance values (R_{norm}) became larger as NETs diameter increased. For both micron- and nano-sized NETs, R_{norm} values at 500 nm remained nearly independent of ICG concentration.

Absorption Coefficient (μ_a) of NETs

We used the measured values of T and R (**Figure 2.3**) in an Inverse Adding-Doubling (IAD) algorithm[60] to estimate the values of μ_a for micron-sized NETs formed without extrusion ($d_{mean} \approx 4.31$ μm), and nano-sized NETs formed by single ($d_{mean} \approx 160$ nm) and double extrusions ($d_{mean} \approx 92$ nm) at ICG loading concentrations in the range of 5-20 μM (**Figure 2.4**). We also present the results for blood samples, and EGs not containing ICG in these figures.

The estimated μ_a spectra for whole blood were obtained by using the T and R spectra of the diluted sample in the 400 – 604 nm range, and T and R spectra associated with $\lambda >$ 604 nm for the non-diluted sample in the IAD algorithm values. The estimated μ_a values over the 400 – 604 nm range were then multiplied by 100 to account for the dilution factor during T and R measurements.

The spectral peaks of μ_a at 420, 542, 581 nm (**Figure 2.4a**) are associated with oxyhemoglobin. The respective μ_a values of 25 and 23 mm^{-1} at 542 and 581 nm are in excellent agreement with the values of 29 and 23 mm^{-1} at these wavelengths reported in a

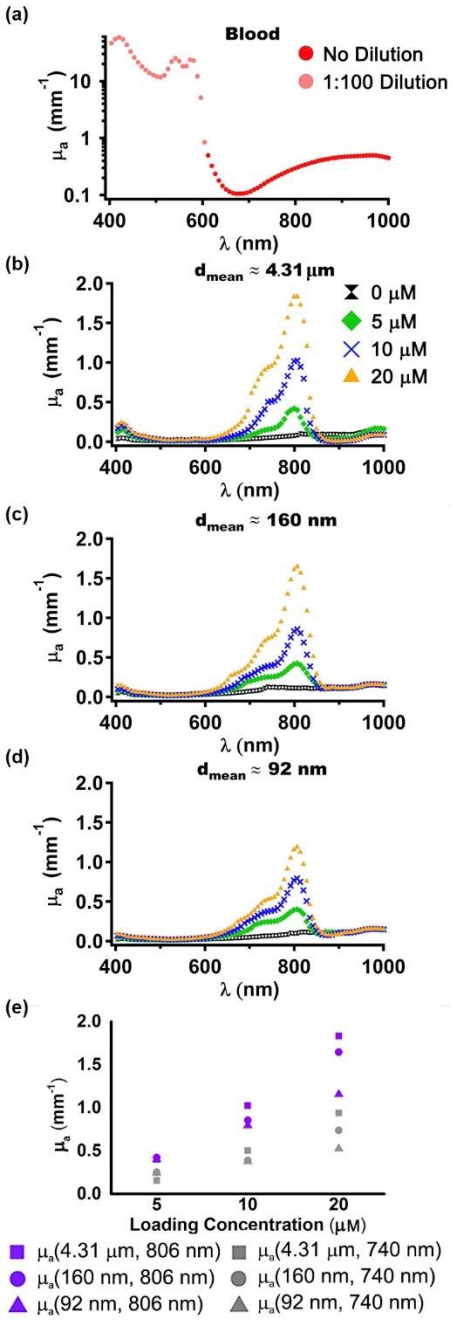

Figure 2.4 Spectrally-dependent values of μ_a for whole bovine blood (a) without dilution for $\lambda >$ 604 nm, and the sample diluted 100 times by adding 1X PBS ($\approx$ 310 mOsm) for $\lambda \leq 604$ nm. Values of μ_a for the diluted sample were multiplied by 100. Spectra of μ_a for (b) micron-sized NETs formed without extrusion, or by (c) single or (d) double extrusions using various ICG concentrations in the loading buffer. Measurements were obtained with NETs suspended in 1X PBS ($\approx$ 310 mOsm). In panel (e), we show a summary of μ_a values at 740 nm and 810 nm.

review article by Jacques,[61] and available in a tabulated form.[73] Our estimated μ_a value of 59 mm^{-1} at 420 nm is lower than the reported values of 115 and 257 mm^{-1} at this wavelength.[65,73] This difference may be due to the relatively low intensity of the quartz-tungsten-halogen lamp used during the measurements of *T* and *R*, at wavelengths close to 400 nm, which could lead to a lower value of the difference between reference and measured *T*, and subsequent under-estimation of μ_a. These overall agreements in spectral characteristics of μ_a with those in literature confirm the validity of our *R* and *T* measurements and the associated IAD algorithm in estimating μ_a (λ) for blood, and subsequently, the NETs in this study.

For these sets of NETs (**Figure 2.4b, c, d**), absorption peaks associated with oxyhemoglobin at 415, 542, and 577 nm, and those associated with deoxyhemoglobin at 439 and 555 nm[74] are greatly diminished, indicating partial or complete depletion of hemoglobin during fabrication of NETs. Consistent with a previous report,[75] the absorption peak at 414 nm is attributed to ICG, and for the three sets of NETs, its value in general increased with increasing values of ICG concentration used during fabrication.

For the three sets of NETs, there was an overall trend of increasing μ_a values over the approximate spectra range of 630 – 860 nm as the concentration of ICG in the loading buffer increased. NETs of all diameters had maximum value of μ_a at 806 nm, and a shoulder in the range of ≈ 720 – 760 nm, which correspond to the peak absorption wavelength associated with the monomeric and H-like aggregate forms of ICG within NETs, respectively. For EGs, μ_a spectra did not show a spectral peak at 806 nm or a distinct shoulder, consistent with the fact that ICG was not present in the EGs.

We summarize the values of μ_a for NETs at wavelengths associated with monomeric (806 nm) and H-like aggregate (740 nm) forms of ICG in **Figure 4e**. There was a nearly linear increase in μ_a at these wavelengths with increasing ICG concentration in the range of 5-20 μM for micron- and nano-sized NETs, indicating that the ICG content within the NETs increased regardless of the NETs diameter. As ICG concentration in the loading buffer increased from 5 to 20 μM, μ_a (λ = 806 nm) increased by ≈ 4.6 times for micron-sized NETs ($d_{mean} \approx 4.31$ μm), and ≈ 3.0 times for nano-sized NETs with $d_{mean} \approx 92$ nm. In general, at a given ICG concentration, as the NETs diameter increased from nano-sized ($d_{mean} \approx 92$ nm) to micron-sized ($d_{mean} \approx 4.31$ μm), higher amounts of ICG could be loaded into the micron-sized NETs, as evidenced by higher values of μ_a at these wavelengths for the micron-sized NETs.

Reduced Scattering Coefficient (μ_s') of NETs

The diameters of cellular components of whole blood (e.g., erythrocytes) and these NETs (in the range of ≈ 90 nm – 4 μm) are comparable to or larger than the investigated wavelength range of 400 nm – 1000 nm. Therefore, it is expected that the scattering behavior of whole blood and NETs can be described by Mie scattering. Best fits to the estimated values of μ_s' for $\lambda > 620$ nm were obtained with $f_{Rayleigh} = 0$, and $m = 0.517$ based on the T and R values for non-diluted blood sample.

Our estimated values of ≈ 2 – 1.4 mm^{-1} for μ_s' in the range of 620 – 1000 nm are consistent with the reported values of ≈ 1.5 – 1.3 mm^{-1} in this spectral range.[65] The inability to fit the μ_s' values for $\lambda < 620$ nm results from an inherent limitation of the IAD algorithm when the T and R values are relatively low. In particular, these values were less than 6%

for the non-diluted blood samples for T ($\lambda < 620$ nm) and R ($\lambda < 600$ nm). These low values are interpreted by the IAD algorithm as lost photons, and not available to make a contribution towards scattering; therefore, under-estimating μ_s' as compared to theoretical values provided by the analytical expression in **equation 2.2**.

Successful fits to μ_s' profiles in the approximate spectral band of 440 – 635 nm were obtained with $f_{Rayleigh} = 0$, and respective values of $m = 1.30$, 1.35, and 2.60 for NETs formed without extrusion ($d_{mean} \approx 4.31$ μm) and by single extrusion ($d_{mean} \approx 160$ nm) or double extrusions ($d_{mean} \approx 92$ nm). We extrapolated these fits to be consistent with Mie theory. Deviations from the analytical fits for $\lambda < 440$ nm and $\lambda > 635$ nm are due to limitations of the IAD algorithm. The algorithm under-estimates the values of μ_s' when $\lambda < 440$ nm or $\lambda > 635$ nm, likely due to the decrease in R values of the NETs over these spectral bands. For the micron-sized NETs ($d_{mean} \approx 4.31$ μm), and the nano-sized NETs ($d_{mean} \approx 92$ nm), the IAD algorithm tends to over-estimate the μ_s' over the 828 – 863 nm spectral band, possibly due to the T values $> \approx 10\%$ and low R values $< \approx 6\%$ associated with these NETs at these wavelengths.

Estimated values of m increased as the diameter of the NETs decreased, and appeared to follow a trajectory to reach the scattering power of 4 (associated with Rayleigh scattering) if the NETs diameter were to become smaller. The estimated values of m in the range of 1.30 and 2.60 are similar to those reported for soft tissues such as brain ($m = 1.2$),[76] heart ($m = 1.26$),[76] prostate ($m = 1.52$),[77] and breast ($m = 2.74$).[78]

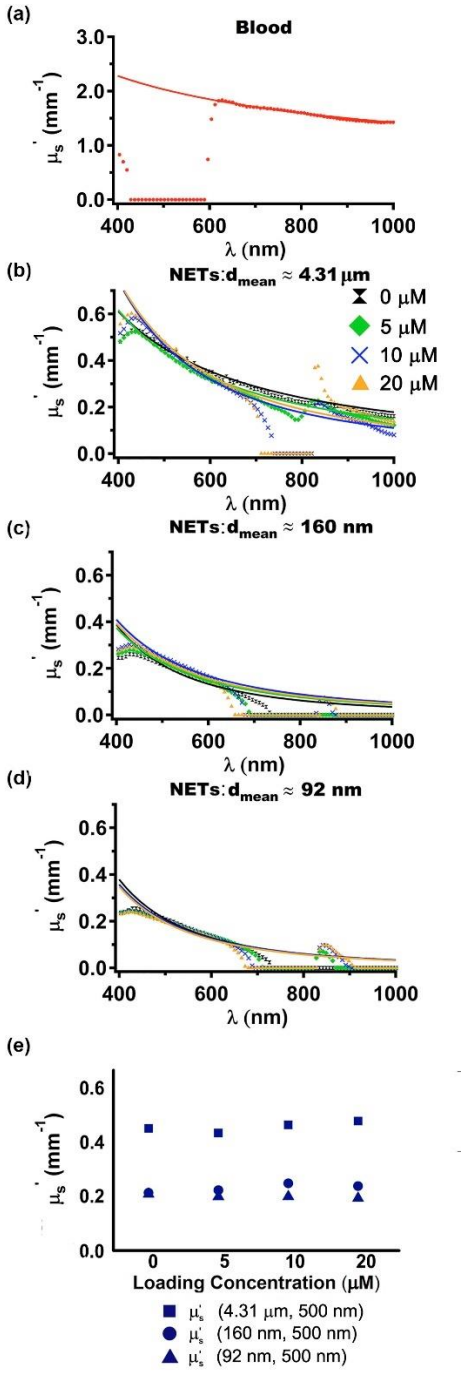

Figure 2.5 Spectrally dependent values of μ_s' for whole bovine blood (a) without dilution and the fitted profile based on equation (2.2). Spectra of μ_s' for (b) micron-sized NETs formed without extrusion, or by (c) single or (d) double extrusions using various ICG concentrations in the loading buffer, and the fitted profile based on equation (2.2). Measurements were obtained with NETs suspended in 1X PBS (≈ 310 mOsm). In panel (e), we show a summary of μ_s' values at 500 nm.

For all sets of NETs, values of μ_s' decreased with increasing wavelength in accordance with the analytical expression for Mie scattering, and were minimally dependent on ICG concentration used in fabricating them. While values of μ_s' were similar for the nano-sized NETs, they increased for the micron-sized NETs at the corresponding wavelengths.

We summarize the estimated values of μ_s' at 500 nm, a wavelength at which there is little contributions from absorption by hemoglobin and ICG, in **Figure 2.5e**. For both micron- and nano-sized NETs, μ_s' (λ = 500 nm) remained nearly independent of ICG concentration. At all ICG concentrations, values of μ_s' (λ = 500 nm) for micron-sized NETs were ≈ 2.2 times higher than those for nano-sized NETs.

Monte Carlo Simulation of Light Distribution in Blood Vessels Containing NETs

We used the estimated values of *g* by the Mie Simulator (Virtual Photonics Initiative, Irvine, California), the estimated values μ_a by the IAD algorithm, and the predicated values of μ_s' according to Mie scattering in a Monte Carlo-based model to simulate the light distribution in response to 806 nm laser irradiation of blood vessels containing NETs (**Figure 2.6a-f**).We assumed that the optical properties of the blood vessel were based on either 45% hematocrit (hct) without NETs (**Figure 2.6a**), or 45% hct plus 50% NETs (**Figure 2.6b-f**), and that the incident fluence was 10 J/cm^2 with the laser beam focused onto a 100 μm diameter spot. In **Figure 2.6g**, we show the resulting fluence levels as a function of the depth along the central axis of the laser beam.

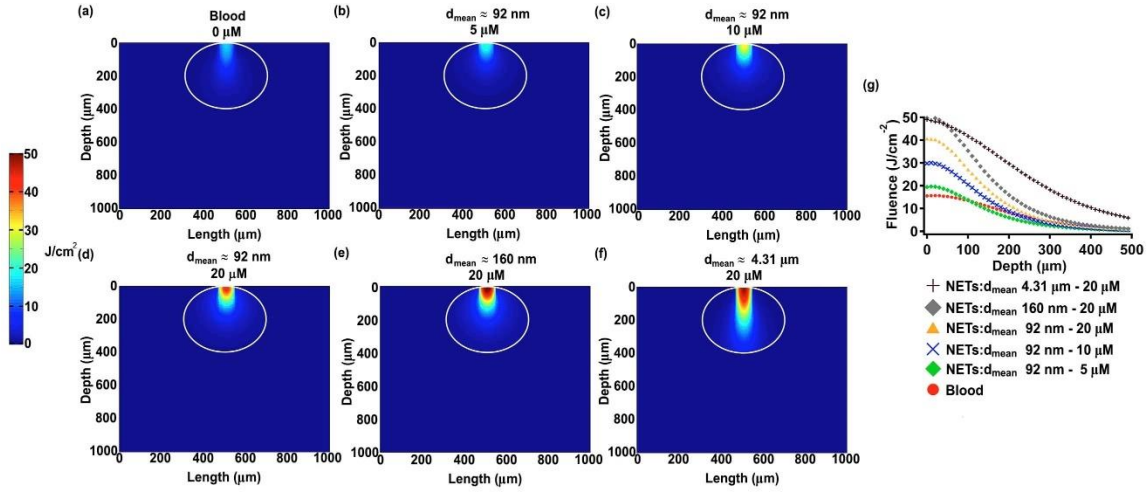

Figure 2.6 Monte Carlo-based estimations of fluence profiles within a simulated 500 μm diameter blood vessel filled with (a) blood containing 45% hematocrit without added NETs, or with added (b-d) nano-sized NETs (d_{mean} ≈ 92 nm), (e) d_{mean} ≈ 160 nm NETs, (f) micron-sized NETS (d_{mean} ≈ 4.31 μm). Relative fractions of blood and NETs in panels (b-e) were 50%. We utilized the optical properties of NETs formed using ICG concentrations of (b-d) 5, 10, and 20 μM, and (e, f) 20 μM in the loading buffer. We assumed 806 nm laser focused on a 100 μm diameter spot at incident fluence of 10 J/cm^2. Color scale bar represents the resulting fluence in J/cm^2 and white circle represents outline of the blood vessel. The white margins delineate the boundaries of the blood vessels. In panel (g), we show the depth profile of the fluences along the central axis of the laser beam.

Doping the blood vessel with NETs enhanced the fluence levels (**Figure 2.6b-g**). While increased fluence values above the incident level, due to back-scattering,[79] were predicted within the blood vessel without NETs, the subsurface peak fluence values were further amplified in the presence of NETs.

Nano-sized NETs of d_{mean} ≈ 160 nm and micron-sized NETs, fabricated using 20 μM ICG, produced similar fluence levels within the depth of ≈ 100 μm; however, at depths greater than 100, higher fluence levels were predicted by the micron-sized NETs (**Figure 2.6d, g**). Increasing the ICG concentration from 5 μM to 20 μM resulted in an overall increase in fluence values for up to ≈ 300 μm within the blood vessel doped with NETs having d_{mean} ≈ 92 nm (**Figure 2.6b-d, g**). Doping the blood vessel with micron-sized NETs

($d_{mean} \approx 4.31$ μm) produced higher fluence values deeper into the blood vessel when compared to nano-sized NETs (**Figure 2.6f, g**), attributed to higher forward scattering (g = 0.99). These results imply that for light-mediated destruction of large blood vessels, micron-sized NETs may provide better efficacy in terms of offering the ability to achieve higher fluences deeper into the blood vessel.

Conclusion

We report, for the first time, the optical properties of NETs as a function of their diameters and the ICG concentration level used in fabricating them. Our results demonstrate that for a given NETs diameter, values of μ_a increased over the approximate spectral band of 630 – 860 nm with increasing ICG concentration. Micron-sized NETs produced the highest peak value of μ_a when using ICG concentrations of 10 and 20 μM as compared to nano-sized NETs. For these NETs, spectral profiles of μ_s' were minimally affected by ICG concentration used in fabricating the NETs. Micron-sized NETs had higher values of μ_s' as compared to nano-sized NETs. Knowledge of the NETs optical properties establishes a framework for development of mathematical models aimed at predicting the optical response of biological tissues containing NETs. Additionally, optical properties of NETs are important in guiding the selection of appropriate light dosimetry parameters for various light-based biomedical application of NETs.

Chapter 3

Photothermal Treatment of Port Wine Stains Using Erythrocyte-Derived Particles Doped with Indocyanine Green: A Theoretical Study

Abstract

Pulsed dye laser irradiation in the wavelength range of 585-600 nm is currently the gold standard for treatment of PWSs. However, this treatment method is often ineffective for deeply seated blood vessels and in individuals with moderate to heavy pigmentation. Use of optical particles doped with the FDA-approved NIR absorber, ICG, can potentially provide an effective method to overcome these limitations. Herein, we theoretically investigate the effectiveness of particles derived from erythrocytes, which contain ICG, in mediating photothermal destruction of PWS blood vessels. We refer to these particles as NETs. Our theoretical model consists of a Monte Carlo algorithm to estimate the volumetric energy deposition, a finite elements approach to solve the heat diffusion equation, and a damage integral based on an Arrhenius relationship to quantify tissue damage. The model geometries include simulated PWS blood vessels as well as actual human PWS blood vessels plexus obtained by optical coherence tomography (OCT). Our simulation results indicate that blood vessels containing micron- or nano-sized NETs and irradiated at 755 nm have higher levels of photothermal damage as compared to blood vessels without NETs irradiated at 585 nm. Blood vessels containing micron-sized NETs also showed higher photothermal damage than blood vessels containing nano-sized NETs. The theoretical model presented in this study can be used in guiding the fabrication of NETs with patient-specific optical properties to allow for personalized treatment based on the depth and size of blood vessels as well as the pigmentation of the individual's skin.

Introduction

PWSs are congenital and progressive malformations of dermal capillaries that occur in approximately three children per 1,000 live births.[80] Pulsed dye lasers (PDL) with wavelengths in the range of 585-600 nm have become the most prevalent treatment for PWSs.[81–84] This treatment uses laser light to target the endogenous hemoglobin for photothermolysis of the blood vessels. Although clinical results can be obtained in the treatment of light red or red macular PWS, especially in children and light-skin individuals, clearing is inefficient, requiring multiple therapeutic sessions. It is reported that about 60 percent of patients receive reduction in redness and lesion size after ten treatment sessions, but only 10-20% experience complete clearance of the stain.[83,85] In addition, PDL treatments within safe therapeutic radiant dosages of ≈ 7-16 J/cm^2, when used in combination with cryogen spray cooling of skin,[86] do not provide the clinically desirable photothermal effects to completely destroy blood vessels located at depths greater than about 500 μm below skin surface.

Another challenge with the current approach is related to the treatment of patients with moderate to heavy skin pigmentation (Fitzpatrick types *IV*-*VI*). The skins of these patients contain a large number of melanosome organelles within the melanocytes, located primarily in the basal epidermis layer. Melanosomes contain melanin, a polymeric pigment with broad absorption spectrum ranging from UV to visible, including the 585-600 nm treatment band. Therefore, melanin acts as a chromophore competing with hemoglobin to partially absorb the photons intended to reach the dermal vascular plexus. The result is

non-specific thermal injury to the epidermis and inefficient photo-destruction of target blood vessels.

A potential phototherapeutic approach is to use an exogenous absorber that can be activated by NIR light to generate heat. The advantage of changing the therapeutic wavelength from 585 nm to NIR wavelength of 755 nm is associated with nearly threefold reduction in the absorption coefficient of a single melanosome.[61] One particularly promising exogenous absorber is ICG. It is one of the least toxic agents administered to humans, and the only FDA-approved NIR dye for specific imaging applications.[7,8] ICG has also been investigated as a photothermal agent for treatment of PWSs,[19,20] and as a photosensitizer for photodynamic therapy of choroidal melanomas and breast adenocarcinomas.[18,87]

Despite its current use in clinical settings, ICG's major disadvantage is its short half-life in blood (3-4 minutes).[7] Due to its amphiphilic nature, ICG can non-specifically bind to various biomolecules in the blood, including high- and low-density lipoproteins and albumin. Hepatic parenchymal cells uptake ICG, and/or the ICG-bound molecular complexes leading to biliary excretion into the intestine.[88]

To extend the circulation time and reduce non-specific interactions with plasma proteins and other biomolecules, ICG has been encapsulated into various constructs including synthetic polymers,[28–31] micelles,[22,24] liposomes,[25–27] and silica/silicate matrices.[23,89] Encapsulation within constructs derived from erythrocytes are particularly advantageous due to their naturally long circulation time (≈ 90-120 days), and potential biocompatibility.

We have previously reported on fabrication of vesicles derived from erythrocytes and loaded with ICG, and their utility for fluorescence imaging and photo-destruction of human cells.[47] We refer to these constructs as NETs. A particular feature of NETs is that their diameter can be tuned from micron- to nano-scale, and their ICG content can be adjusted independently during the fabrication process. We recently characterized the effects of NETs' diameter and ICG concentration on the resulting optical properties (μ_a and μ_s') of these constructs.[90] These results are particularly useful in development of mathematical models aimed at quantification of light and laser-induced temperature distributions in tissues containing NETs. As a first step towards potential application of NETs in phototherapy of PWSs, we analyze in dedicated numerical simulations the photothermal response of blood vessels containing NETs, and compare the results with those obtained with the current treatment approach of using pulsed dye lasers in 585-600 nm range. These results can be used to identify the optimum formulation of NETs and appropriate irradiation parameters for NIR photothermal treatment of PWSs.

Materials and Methods

Overview of model

In **Figure 3.1**, we present a block diagram of the mathematical model consisting of three components: a Monte Carlo light-transport model to estimate the energy deposition in response to laser irradiation,[63,64] finite-element model to compute the spatiotemporal temperature distribution based on the heat diffusion equation, and an Arrhenius rate process integral to quantify the resulting thermal damage. Each component of the model is described in the following subsections.

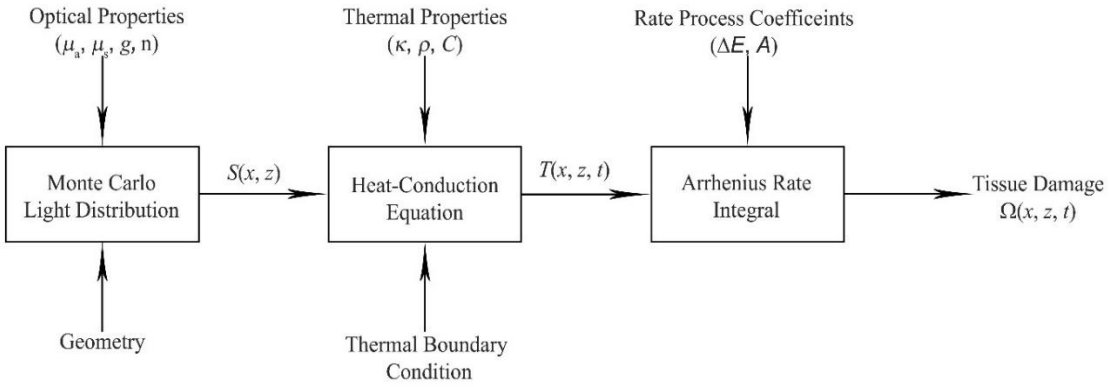

Figure 3.1 Block diagram of the mathematical model components.

Model geometry

We used two geometries to model the human skin with PWS. The first geometry simulated the skin and consisted of a 60 μm thick epidermis and 1,940 μm thick dermis containing blood vessels (**Figure 3.2**). The epidermis was composed of a 45 μm melaninless layer and a 15 μm melanocyte filled layer located at the basal epidermis. Blood vessels were assumed to be cylinders with diameters of 200 μm, running parallel to the *y* axis for the entire length of the geometry (1 mm). The top position of the vessel was located either at 500 or 800 μm below skin surface.

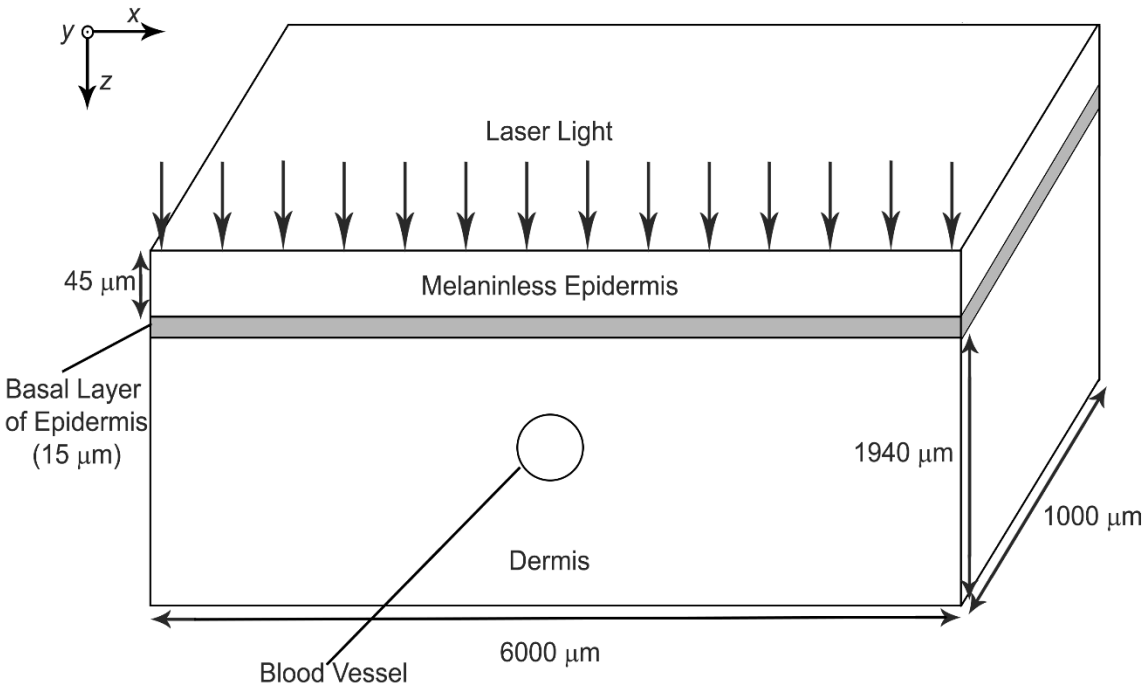

Figure 3.2 Simulated port wine stain geometry.

In addition, we also constructed a PWS skin geometry from an image obtained by optical coherence tomography (OCT) of a PWS patient (**Figure 3.3**).[91] We first removed motion artifact associated with the image cube, 5 mm (length) x 5 mm (width) x 2.8 mm (height), by taking the Fourier transform of each 2D section (5 mm x 5 mm) (axial resolution = 8 μm) and applying a bandpass filter with cutoff normalized frequencies of 0.1 and 1.0, where 1.0 corresponds to half of the sampling frequency in the horizontal direction, and 0.0 and 0.01 in the vertical direction. We then took the inverse Fourier transform of each image, and converted into binary values through thresholding. Finally, speckle noise was removed using a 3-dimensional median filter.

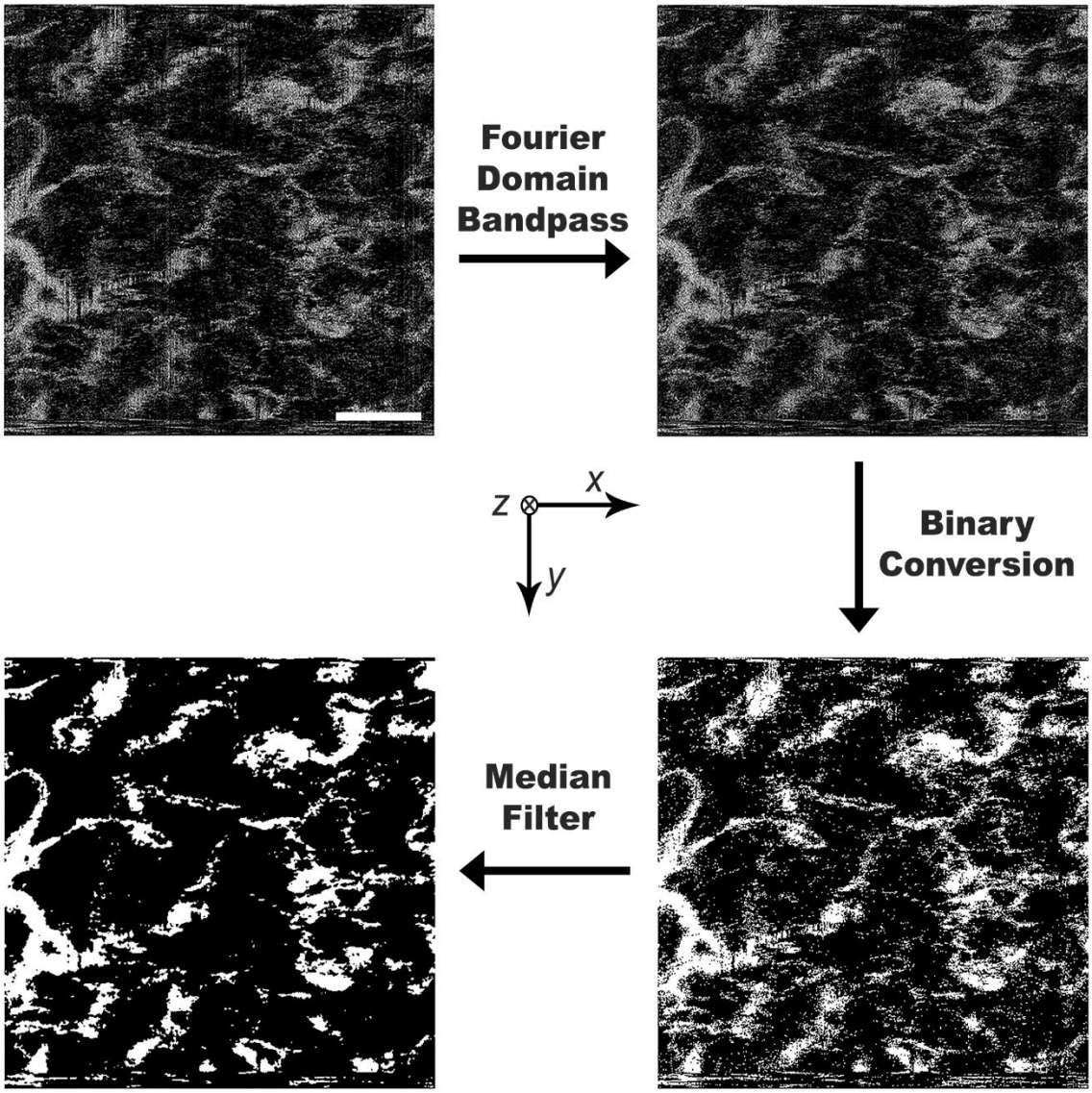

Figure 3.3 Flow chart of processing an OCT image of PWS skin for use in mathematical model. With respect to the coordinate system shown in Figure 3.2, the coordinate system here is rotated 90 degrees counter-clockwise around the *x*-axis. The images are horizontal cross-sections in the *x*-*y* plane at depth of z = 680 μm.

Optical properties of human skin

The baseline absorption coefficient for melaninless epidermis $\mu_{a,base}$ (mm^{-1}), and bloodless dermis was approximated by[92]

$$\mu_{a,base} = 0.0244 + 8.53 \cdot \exp[-\frac{\lambda - 154}{66.2}] \quad (3.1)$$

where λ is wavelength in nm. The absorption coefficient for the basal layer of the epidermis $\mu_{a,basal}$ is a combination of the $\mu_{a,base}$, and the absorption coefficient of melanosomes $\mu_{a,mel}$:

$$\mu_{a,basal} = f_{mel} \cdot \mu_{a,mel} + (1 - f_{mel}) \cdot \mu_{a,base} \quad (3.2)$$

where f_{mel} is the volume fraction of melanosomes. In this study, we present lightly, moderately and heavily pigmented skin with f_{mel} = 4, 15, and 50% respectively,[93] and $\mu_{a,mel}$ (mm^{-1}) defined as:[92]

$$\mu_{a,mel} = 6.6 \times 10^{10} \cdot \lambda^{-3.33} \quad (3.3)$$

For simulated single vessels, we accounted for attenuation of the incident light by absorption in the remaining PWS blood vessels by adjusting the absorption coefficient of the dermis ($\mu_{a,der}$) (**Table 3.1**) as:[64]

$$\mu_{a,der} = f_i \; C_i \; \mu_{a,blood} + (1 - f_i)\mu_{a,der} \quad (3.4)$$

where C_i is the correction factor accounting for optical screening within a blood vessel with radius r_i and f_i is the fractional volume occupied by the PWS blood vessels. In this adjustment, we account for the average r_i of the PWS blood vessels within a range of subsurface depths (z) (see **Table 3.1**), and assume 45% hct with oxygen saturation of 70%:[64]

$$C_i \approx 0.039 + 0.49 \exp\left[-\frac{\mu_{a,blood}(45\%\ \text{hct})\, r_i}{0.19}\right] + 0.47 \exp\left[-\frac{\mu_{a,blood}(45\%\ \text{hct})\, r_i}{0.19}\right] \quad (3.5)$$

The adjusted values of $\mu_{a,der}$ at 585 nm vary with depth and the corresponding values of r_i and f_i, whereas those for 755 nm are nearly independent of depth.

Table 3.1 Adjusted absorption coefficient of dermis used in this study.

z(μm)	r_i (μm)	f_i (%)	$\mu_{a,der}$ (585 nm) (mm^{-1})	$\mu_{a,der}$ (755 nm) (mm^{-1})
60-260	25	5.2	0.071	0.025
260-460	37	8.0	0.090	0.024
460-660	34	3.8	0.062	0.025
660-860	27	2.5	0.053	0.025
860-1060	24	2.0	0.050	0.025
1060-2000	24	1.5	0.047	0.025
PWS blood vessels imaged by OCT all z(μm)			0.073	0.026

For OCT simulated vessels, $\mu_{a,der}$ was expressed as:

$$\mu_{a,der} = f_{blood} \cdot \mu_{a,blood} + (1 - f_{blood}) \cdot \mu_{a,bas} \tag{3.6}$$

where f_{blood} is the volume fraction of blood in the healthy dermis, chosen to be 0.2% consistent with literature reported value,[92] and $\mu_{a,blood}$ (mm^{-1}) is the absorption coefficient of blood with oxygen saturation of 70%. In this case, values of $\mu_{a,der}$ were not adjusted since the actual distributions of blood vessels were directly obtained from the OCT images.

The μ_s (mm^{-1}) of the melaninless epidermis, epidermal basal layer, and dermis were estimated as[92]

$$\mu_s = \frac{2\times10^4 \cdot \lambda^{-1.5} + 2\times10^{11} \cdot \lambda^{-4}}{1-g} \tag{3.7}$$

where g was assumed to be 0.8 for 585 nm[94] and 0.91 at 755 nm,[95] the irradiation wavelengths used in this study.

Optical properties of NETs and blood vessels

Spectrally-dependent values of μ_a and μ_s' for micron-sized NETs (μNETS) and nano-sized NETs (nNETs) with respective mean diameters (d_{mean}) of ≈4 μm and 92 nm were previously estimated using an integrating sphere in conjunction with an inverse adding-doubling algorithm.[90] Values of μ_a and μ_s for blood with 45% hct and oxygen saturation of 70% were obtained from literature.[65] We then determined the effective optical properties of blood vessel (BV) as:

$$\mu_{a,BV} = (1 - f_{NETs})\mu_{a,blood} + f_{NETs}\mu_{a,NETs} \tag{3.8}$$

$$\mu_{s,BV} = (1 - f_{NETs})\mu_{s,blood} + f_{NETs}\mu_{s,NETs} \tag{3.9}$$

$$g_{BV} = (1 - f_{NETs})g_{blood} + f_{NETs}g_{NETs} \tag{3.10}$$

where $\mu_{a,x}$, $\mu_{s,x}$, and g_x are the respective effective absorption and scattering coefficients, and anisotropy factor, with the subscript x standing for either blood vessels containing blood and volume fraction of NETs (f_{NETs}) (assumed 10 or 25%), blood, or NETs. We varied $\mu_{a,NETs}$ so that $\mu_{a,BV}$ had values in the range of 1-18 mm^{-1}. To determine the ICG concentration in NETs fabrication buffer [ICG] (μM) to produce a desired $\mu_{a,BV}$, we first used a linear regression to quantify the relationship between the previously reported estimates of $\mu_{a,NETs}$, and the utilized values of [ICG]:

$$[ICG] = 17.8 \cdot \mu_{a,NETs} \tag{3.11}$$

Next, by re-arranging **equation 3.8** for $\mu_{a,NETs}$, and substituting the expression into **equation 3.11**, we obtained [ICG].

$$[\text{ICG}] = 17.8\left[\frac{\mu_{a,BV} - (1 - f_{NETs})\mu_{a,blood}(45\%\ \text{hct})}{f_{NETs}}\right] \quad (3.12)$$

Using **equation 3.12**, we determined [ICG] values of ≈ 108, 286, 464, 642, 820, and 998 μM to produce the corresponding $\mu_{a,BV}$ values of 1, 2, 3, 4, 5, and 6 mm^{-1}. For example, values of f_{NETs} = 25% and $\mu_{a,BV}$ = 18 mm^{-1} resulted in [ICG] = 1,258 μM. Values of the optical properties used in this study are provided in **Table 3.2**.

Table 3.2 Optical properties used in this study. Optical properties for blood are based on 45% hematocrit.

Wavelength	Optical Properties	Melaninless Epidermis	Basal Layer Containing Melanosomes (Light)	Basal Layer Containing Melanosomes (Moderate)	Basal Layer Containing Melanosomes (Heavy)	Dermis	Blood	μNETs (d_{mean} = 4 μm)	nNETs (d_{mean} = 92nm)	$\mu_{a,BV}$
585 nm	μ_a (mm^{-1})	0.037	1.65	6.07	20.15	a	17.91	-	-	
	μ_s (mm^{-1})	15.61	15.61	15.61	15.61	15.61	76.05	-	-	
	g	0.80	0.80	0.80	0.80	0.80	0.970	-	-	
755 nm	μ_a (mm^{-1})	0.025	0.71	2.58	8.61	a	0.44	6.04-56.04	6.04-56.04	1-18
	μ_s (mm^{-1})	17.55	17.55	17.55	17.55	17.55	79.85	2.20	0.06	59.90-72.09
	g	0.91	0.91	0.91	0.91	0.91	0.983	0.99	0.55	0.87-0.98

[a]See Table 3.1

Mathematical Model

The three-dimensional Monte Carlo model for light transport and energy deposition was developed earlier by Majaron *et al.*[63,64] Our simulations involved one million photons for 585 or 755 nm flat-top laser beams with diameter of 6 mm for simulated PWS geometry, and 8 mm for the skin model based on the PWS patient OCT record. With a 2.3 GHz central processing unit, each Monte Carlo simulation took ≈ 2-11 hours depending on the geometry

and optical properties of the tissue. For example, the run time was ≈ 10.5 hours for a simulated geometry containing nNETs (f_{NETs} = 10%, $\mu_{a,BV}$ = 6 mm^{-1}), and lightly pigmented skin (f_{mel} = 4%) irradiated at 755 nm. For an OCT geometry, an example run time was ≈ 2.0 hours for a moderately pigmented skin (f_{mel} = 15%) irradiated at 585 nm without NETs.

We used the heat diffusion equation to calculate the spatiotemporal temperature profiles in response to laser irradiation:

$$\kappa[\frac{\partial T^2(x,z,t)}{\partial^2 x}+\frac{\partial T^2(x,z,t)}{\partial^2 z}]+S(x,z)=\rho C\frac{\partial T(x,z,t)}{\partial t} \tag{3.13}$$

where κ is the thermal conductivity, $T(x, z, t)$ is the skin temperature (°C) (assuming symmetry about the y-axis), x is the lateral distance from the beam center (m), z is the depth into the skin, t is time (s), $S(x, z)$ is the heat source term resulting from absorption of photons (W m^{-3}), ρ is the density (kg m^{-3}), and C is the specific heat capacity (J kg^{-1} °C^{-1}). Thermal properties of human skin used in the study were density, ρ = 1,200 kg m^{-3}, specific heat capacity, C = 3,600 J kg^{-1} °C^{-1}, and κ = 0.26, 0.53, 0.53 W m^{-1} °C^{-1} for epidermis, dermis, and blood vessels, respectively.[38] The baseline skin temperature was 35 °C.

We assumed that a cryogen spurt was sprayed onto the skin surface immediately prior to the laser pulse.[96–99] To account for this type of skin cooling, we implemented a convective surface boundary condition as follows:

$$-\kappa\frac{\partial T(x,z,t)}{\partial z}\Big|_{z=0}=h[T_{med}-T(x,z,t)\big|_{z=0}] \tag{3.14}$$

where T_{med} is the temperature of the cryogen film on the skin surface (°C), and h is the convective heat transfer coefficient at the skin surface. We utilized the relevant thermal

parameters associated with the boundary condition from our previous work,[99–101] and list them in **Table 3.3**. The heat-diffusion equation was solved numerically using the commercial finite-elements software package, FEMLAB®. The finite-elements run time for simulated geometries was 2-3 minutes using 1200x400 nodes. For OCT geometries, run time was 12-18 hours using 500x350 nodes.

Table 3.3 Parameters for Surface Thermal Boundary Condition

Time Interval	h (W/m^2 °C)	$T_{surface}$(°C)	Duration (ms)
Cryogen spurt application	4000	-50	100
Cryogen pool residence	3000	-26	200
Rewarming	10	25	500

Thermal damage to the skin was quantified using the Arrhenius rate damage integral:

$$\Omega(x,z) = A\int_0^{\tau} \exp[-\frac{E}{RT(x,z,t)}]\, dt \qquad (3.15)$$

where $\Omega(x, z)$ is the damage index, A is the frequency factor (A = 1.8 x 10^{51} s^{-1} for bulk skin and A = 7.6 x 10^{66} s^{-1} for blood) , E is the damage activation energy (E = 327,000 J mol^{-1} for bulk skin and E = 455,000 J mol^{-1} for blood) and R is the universal gas constant (R = 8.314 J mol^{-1} K^{-1}).[102,103] Value of $\Omega(x, z)$ = 1 is associated with irreversible damage to 63% of the tissue. Laser pulse duration was fixed at 3 ms, and it was applied immediately after termination of a 100 ms cryogen spurt. Values of $\Omega(x, z)$ were calculated following the laser pulse and through the duration of the rewarming interval. The percent photothermal damage to the blood vessel (%Damage) was defined as the area of the damaged vessel at this time divided by the total cross-sectional area.

Results and Discussion

Simulated PWS geometry

Threshold incident dosage for epidermal damage in absence of NETs

We first determined the threshold incident dosage (D_{th}) for epidermal damage in response to 585 and 755 nm irradiation without blood vessels. For lightly, moderately, and heavily pigmented skin, values of D_{th} were determined as 8, 3 and 1 J/cm^2 for 585 nm, and 21, 6, and 3 J/cm^2 for 755 nm irradiation, respectively (**Table 3.4**). These simulation results confirm that use of 755 nm increases the threshold for epidermal injury, due to the lower absorption of melanin at this wavelength compared to 585 nm. These results are consistent with a previous clinical study where laser irradiation at 755 nm with incident dosages greater than 10 J/cm^2 effective induced PWS lightening.[104]

Table 3.4 Estimated threshold incident dosages for epidermal damage (D_{th}) in absence of NETs for simulated PWS skin geometry.

Wavelength	Skin Pigmentation	f_{mel} (%)	D_{th} (J·cm^{-2})
585 nm	Light	4	8
	Moderate	15	3
	Heavily	50	1
755 nm	Light	4	21
	Moderate	15	6
	Heavily	50	3

Photothermal response of PWS blood vessels in the absence of NETs

The percent photothermal damage profiles to blood vessels without NETs for lightly (f_{mel} = 4%) pigmented skin at the D_{th} = 8 J/cm^2 at 585 nm and 21 J/cm^2 at 755 nm are shown in **Figure 3.4**. Complete damage to blood vessels without NETs was observed for blood

vessels in response to 585 nm laser irradiation at D_{th} = 8 J/cm^2 (**Figure 3.4a, c**). However, this vascular damage was also accompanied by damage to the surrounding dermis. For blood vessels without NETs irradiated at 755 nm, there was 79 and 50 %Damage to vessels at depths of 500 and 800 µm, respectively, without thermal injury to perivascular dermis (**Figure 3.4b, d**).

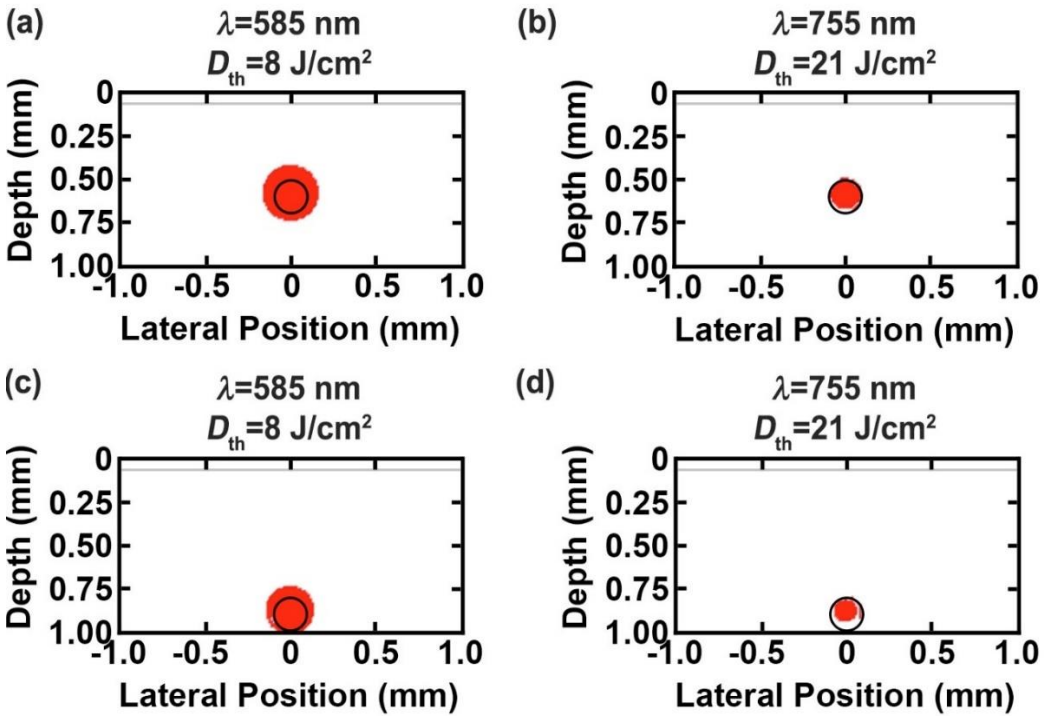

Figure 3.4 Damage profiles shown in red ($\Omega \geq 1$) for blood vessels located at (a, b) 500, and (c, d) 800 µm below skin surface for lightly pigmented skin (f_{mel} = 4%) in response to (a, c) 585, and (b, d) 755 nm laser irradiation without NETs.

For moderately pigmented skin (f_{mel} = 15%) in response to 585 nm irradiation at D_{th} = 3 J/cm^2, %Damage to the vessels at 500 and 800 µm were 34% and 11 %, respectively (**Figure 3.5**). In response to 755 nm irradiation at D_{th} = 6 J/cm^2, there was no damage to the blood vessels at either depths. Lastly, for heavily pigmented skin (f_{mel} = 50%) in response to 585 nm irradiation at D_{th} = 1 J/cm^2 and 755 nm irradiation at D_{th} = 3 J/cm^2,

there was no damage to the vessels at either depths (results not shown). The decrease in %Damage for blood vessels with moderately and heavily pigmented skin can be attributed to the decrease in D_{th}, as well as increased light absorption within the basal epidermis.

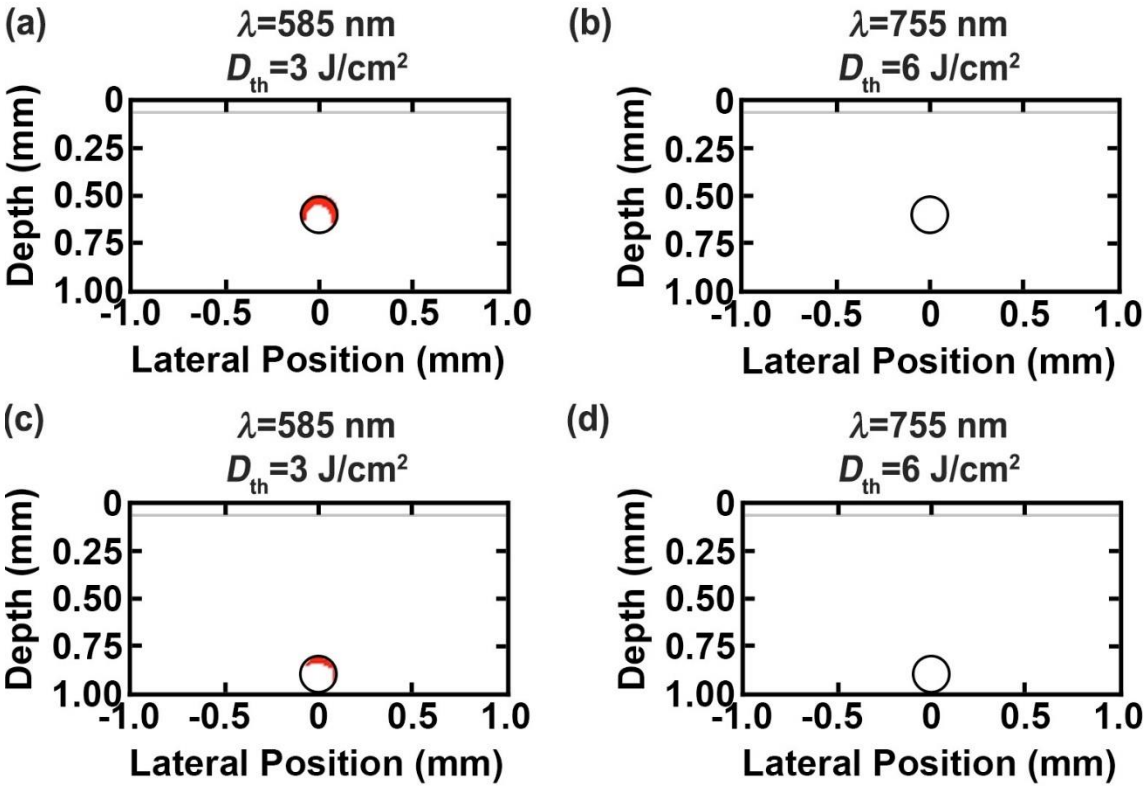

Figure 3.5 Damage profiles shown in red ($\Omega \geq 1$) for blood vessels located at (a, b) 500, and (c, d) 800 µm below skin surface for moderately pigmented skin (f_{mel} = 15%) in response to (a, c) 585, and (b, d) 755 nm laser irradiation without NETs.

Photothermal response of PWS blood vessels containing NETs

The percent photothermal damage profiles to blood vessels containing µNETs or nNETs (f_{NETs} = 10%) for lightly pigmented skin (f_{mel} = 4%) in response to 755 nm irradiation at D = 21 J/cm^2 are shown in **Figure 3.6**. There was 100% damage to blood vessels located at depths of 500 and 800 µm below skin surface containing µNETs, or nNETs with $\mu_{a,BV}$ of 1 mm^{-1} (**Figure 3.6**). As the depth of the blood vessel increased from 500 to 800 µm, there

was a decrease in damage to the dermis, which was further reduced when using nNETs as compared to µNETs.

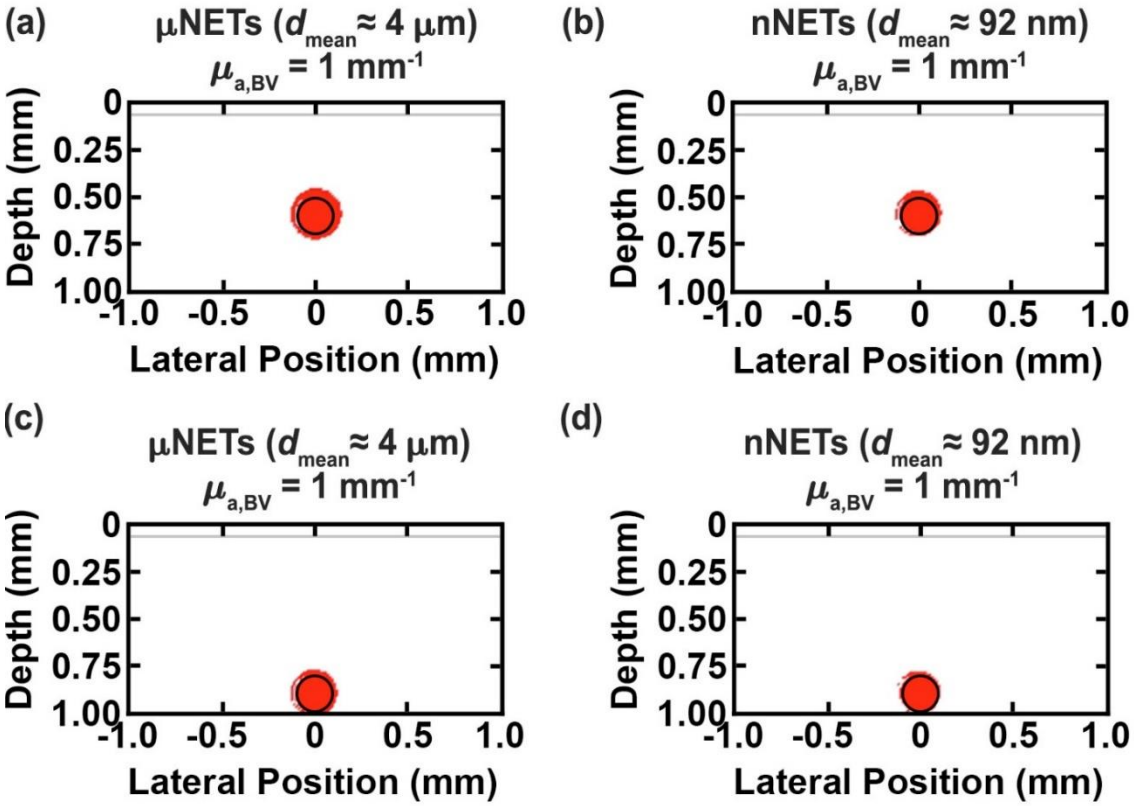

Figure 3.6 Damage profiles shown in red ($\Omega \geq 1$) for blood vessels containing µNETs, or nNETs at f_{NETs} = 10% with $\mu_{a,BV}$ = 1 mm^{-1}, and located at depths of (a, b) 500, and (c, d) 800 µm below skin surface. Light skin pigmentation (f_{mel} = 4%), λ = 755 nm, D_{th} = 21 J/cm^2.

These results suggest PWS patients with light pigmentation and blood vessels as deep as 500-800 µm could potentially benefit from the delivery of µNETs or nNETs that yield $\mu_{a,BV}$ = 1 mm^{-1} to achieve photothermal injury to the blood vessels. This value of $\mu_{a,BV}$ corresponds to µNETS or nNETs with $\mu_{a,NETs} \approx 6$ mm^{-1}, which can be fabricated by using ≈ 108 µM ICG in the fabrication buffer (**equation 3.12**).

For moderately pigmented skin (f_{mel} = 15%), f_{NETs} = 10%, and 755 nm laser irradiation at D_{th} = 6 J/cm^2, there was no damage to the blood vessels when using µNETs or nNETs that yielded $\mu_{a,BV}$ = 1 mm^{-1} (**Figure 3.7a**). For $\mu_{a,BV}$ = 3 mm^{-1}, the blood vessel at depth of 500 µm showed 94 and 86 %Damage when containing µNETs or nNETs, respectively (**Figure 3.7a, b**). For this value of $\mu_{a,BV}$, when the depth of the blood vessel was increased to 800 µm, respective %Damage values were reduced to 89% and 74% in the presence of µNETs or nNETs (**Figure 3.7c,d**).

In general, for the case of the blood vessel containing µNETs at depth of 500 µm, %Damage to blood vessels followed an exponentially increasing behavior with $\mu_{a,BV}$, and approached an asymptotic value of ≈95% for values of $\mu_{a,BV} \geq 3$ mm^{-1}, corresponding to $\mu_{a,NETs} \geq 26$ mm^{-1} (**Figure 3.7a**). For the blood vessel containing nNETs at depth of 500 µm, and blood vessels containing µNETs or nNETs at depth of 800 µm, the relationship between $\mu_{a,BV}$ and %Damage to blood vessels followed a sigmoidal behavior where below a certain threshold value of $\mu_{a,BV}$ (and the corresponding $\mu_{a,NETs}$) there was no damage to the vessel (**Figure 3.7a**). These results indicate that once $\mu_{a,BV}$ exceeds ≈ 3 mm^{-1} with either µNETs or nNETs, %Damage to blood vessels ranging in depth between 500-800 µm is maximized to the same level of ≈95%.

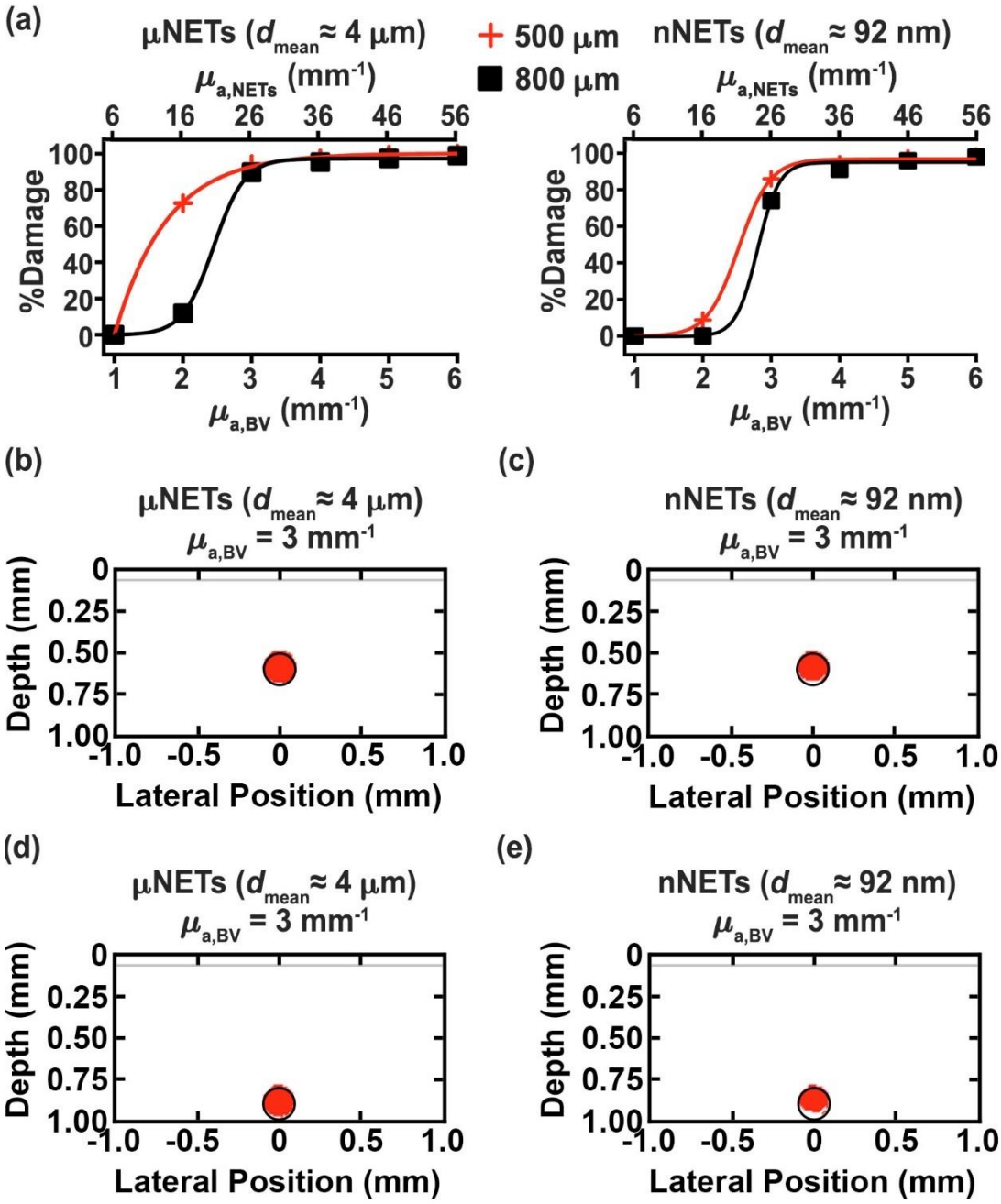

Figure 3.7 (a) %Damage to blood vessels containing μNETs or nNETs (f_{NETs} = 10%) as a function of $\mu_{a,BV}$ and $\mu_{a,NETs}$ (markers) fitted with exponential or sigmoidal functions (solid curves). Damage profiles shown in red ($\Omega \geq 1$) for blood vessels located at depths of (b, c) 500, and (d, e) 800 μm below skin surface containing μNETs, or nNETs at f_{NETs} = 10% with $\mu_{a,BV}$ = 3 mm^{-1}. Moderate skin pigmentation (f_{mel} = 15%), λ = 755 nm, D_{th} = 6 J/cm^2.

The therapeutic advantage of NETs in conjunction with 755 nm laser irradiation over current treatment at 585 nm without NETs was more evident with moderate skin pigmentation. For example, blood vessels with $\mu_{a,BV}$ = 6 mm^{-1}, and containing µNETs or nNETs had >98 %Damage to vessels at either depths (**Figure 3.7a**), whereas blood vessels without NETs irradiated at 585 nm had 34 and 11 %Damage to vessels at depths of 500 and 800 µm, respectively (**Figure 3.5**).

For heavily pigmented skin (f_{mel} = 50%), there was a dramatic decrease in damage to blood vessels containing NETs with $\mu_{a,BV}$ = 1-6 mm^{-1} (f_{NETs} = 10%) in response to 755 nm laser irradiation at D_{th} = 3 J/cm^2 (results not shown). When f_{NETs} was increased to 25%, blood vessels located at depths of 500 and 800 µm showed 60 and 36 %Damage, respectively, in presence of µNETs ($\mu_{a,BV}$ = 18 mm^{-1}) (**Figure 3.8a,c**). At this value of f_{NETs}, blood vessels containing nNETs ($\mu_{a,BV}$ = 18 mm^{-1}) showed 36 and 27 %Damage to vessels at depths of 500 and 800 µm, respectively (**Figure 8b,d**). For $\mu_{a,BV}$ = 18 mm^{-1}, the corresponding ICG concentrations in the fabrication is ≈ 1,258 µM (**equation 3.12**).

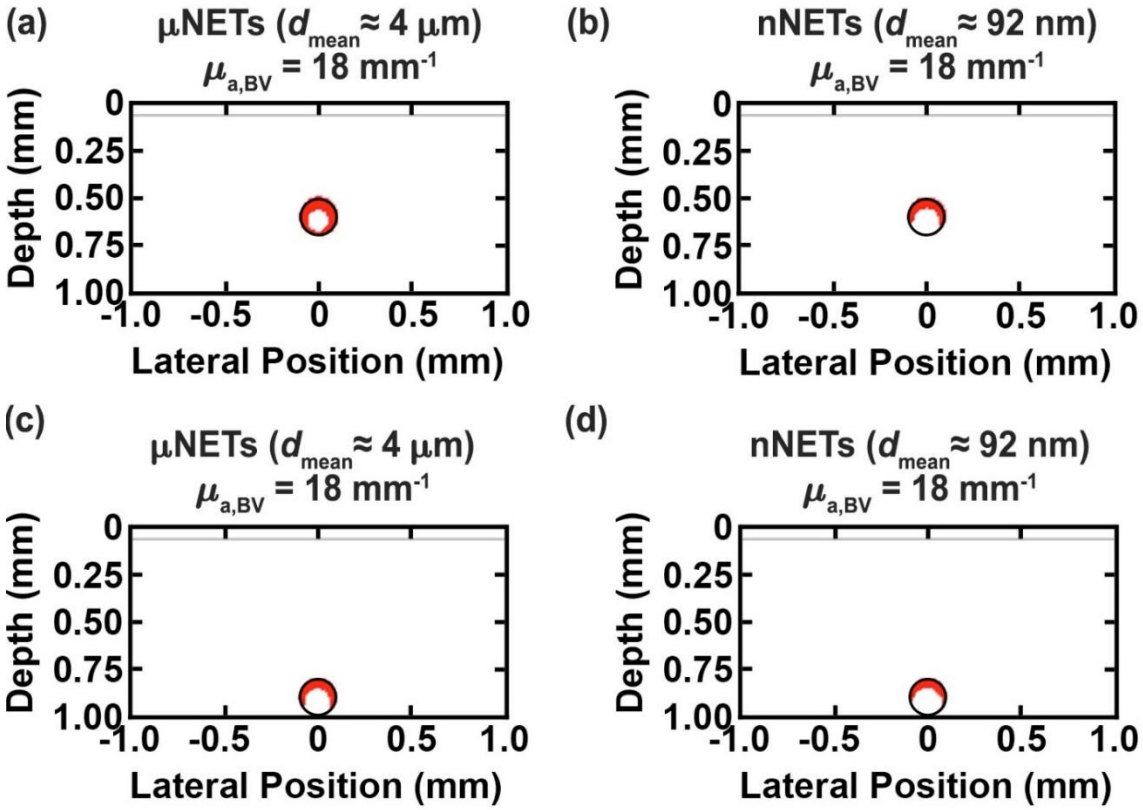

Figure 3.8 Damage profiles shown in red ($\Omega \geq 1$) for blood vessels containing μNETs, or nNETs at f_{NETs} = 25% with $\mu_{a,BV}$ = 18 mm^{-1}, and located at depths of (a, b) 500, and (c, d) 800 μm below skin surface. Heavy skin pigmentation (f_{mel} = 50%), λ = 755 nm, D_{th} = 3 J/cm^2.

These results demonstrate that blood vessels containing μNETs had greater therapeutic efficacy as compared to nNETs. The increase in %Damage to a blood vessel containing μNETs is due to higher energy deposition values deeper into the blood vessels resulting from greater amount of light scattered in the forward direction by μNET (g = 0.99, **Table 3.2**) as compared to nNETs (g = 0.55, **Table 3.2**). Given their larger diameter, the optical behavior of μNETs is consistent with Mie scattering,[29] allowing for higher forward scattering.

PWS geometry based on patient OCT image

A three-dimensional rendering of the patient PWS geometry is shown in **Figure 3.9a** (see also multimedia files). The PWS vessel diameters ranged from 60 to 650 μm with most around 200 μm, and as deep as 1 mm below the skin surface. To test different skin pigmentations, epidermal layers were added to the geometry with light (f_{mel} = 4%), moderate (f_{mel} = 15%) and heavy (f_{mel} = 50%) pigmentations. Due to the greater therapeutic efficacy of μNETs for simulated PWS vessel geometries, we chose to use μNETs for patient PWS vessels with $\mu_{a,BV}$ = 6 mm^{-1} and f_{NETs} = 10% for lightly pigmented skin (f_{mel} = 4%), and $\mu_{a,BV}$ = 18 mm^{-1} and f_{NETs} = 25% for moderately (f_{mel} = 15%) and heavily (f_{mel} = 50%) pigmented skin. Damage profiles are shown for lightly, moderately and heavily pigmented skin irradiated with 755 nm for PWS vessels with μNETs, or 585 nm for PWS vessels without NETs (**Figure 3.9b-f**).

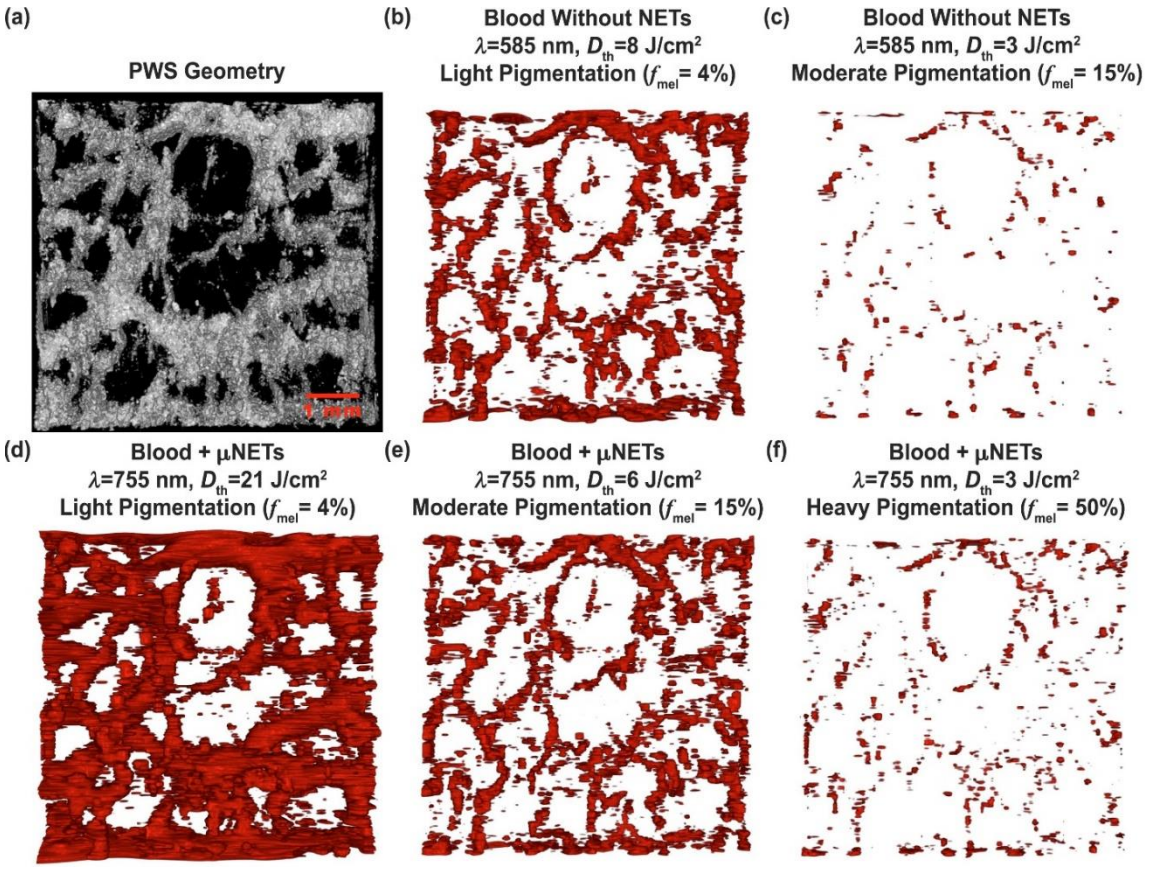

Figure 3.9 Three-dimensional rendering of (a) human PWS obtained by OCT, and (b-f) damage profiles to PWS blood vessels. Red regions correspond to values of $\Omega \geq 1$. Panels (b,c) present damage profiles in response to 585 nm laser irradiation without NETs for light (f_{mel} = 4%), and moderate (f_{mel} = 15%) pigmentation levels, respectively. Panels (d-f) present damage profiles in response to 755 nm laser irradiation in presence of μNETs for light (f_{mel} = 4%), moderate (f_{mel} = 15%), and heavy (f_{mel} = 50%) pigmentation levels, respectively. Parameters for patient PWS blood vessels containing μNETs were $\mu_{a,BV}$ = 6 mm^{-1}, f_{NETs} = 10% for panel (d), and $\mu_{a,BV}$ = 18 mm^{-1}, f_{NETs} = 25% for panels (e, f).

The therapeutic effectiveness of NETs in conjunction with 755 nm irradiation over 585 nm irradiation without NETs can be seen from these results. We calculated the %Damage for vessels up to the depth of 1000 μm below the surface on a pixel by pixel basis within the simulated 3D PWS geometry obtained by OCT imaging. This was

accomplished by comparing each pixel in the 3D damage profile with that of the 3D geometry. The number of pixels showing values of $\Omega \geq 1$ were summed and divided by the total number of pixels in the geometry to obtain an estimate of %Damage. Lightly, moderately and heavily pigmented skin showed %Damage of 88, 30 and 4%, respectively, in presence of μNETs. For PWS vessels without NETs, there was 32 and 2 %Damage for lightly and moderately pigmented skin, respectively. In response to the irradiation parameters investigated, current therapeutic approach, based on 585 nm laser irradiation, is most effective in treating patients with light pigmentation by damaging blood vessels to a depth of ≈ 1.2 mm, but still with some blood vessels remaining intact in the lateral direction (**Figure 3.10b**). Depth of damage is reduced to ≈ 0.8 mm, and accompanied by a reduction in lateral vascular damage in moderately pigmented PWS skin (**Figure 3.10c**).

Under the parameters investigated, laser irradiation at 755 nm in conjunction with μNETs can increase the damage depth to ≈ 1.4 mm, and also induce complete damage to the vascular plexus in the lateral direction in patients with light pigmentation (**Figure 3.10d**). For patients with moderate and heavy pigmentation levels, blood vessels to depth of ≈ 1.2 mm can be damaged when using 755 nm laser irradiation in conjunction with NET, but the extent of lateral vascular damages decreases (**Figure 3.10e, f**). These results suggest that similar to the optical response of single blood vessel, there may be shading effects to reduce the energy deposited to deeper blood vessels.[105] Such effects can occur if vessels are as close as a few microns.[106] Optimizing the ICG concentration in NETs may provide a means to allow for more uniform light energy distributions.

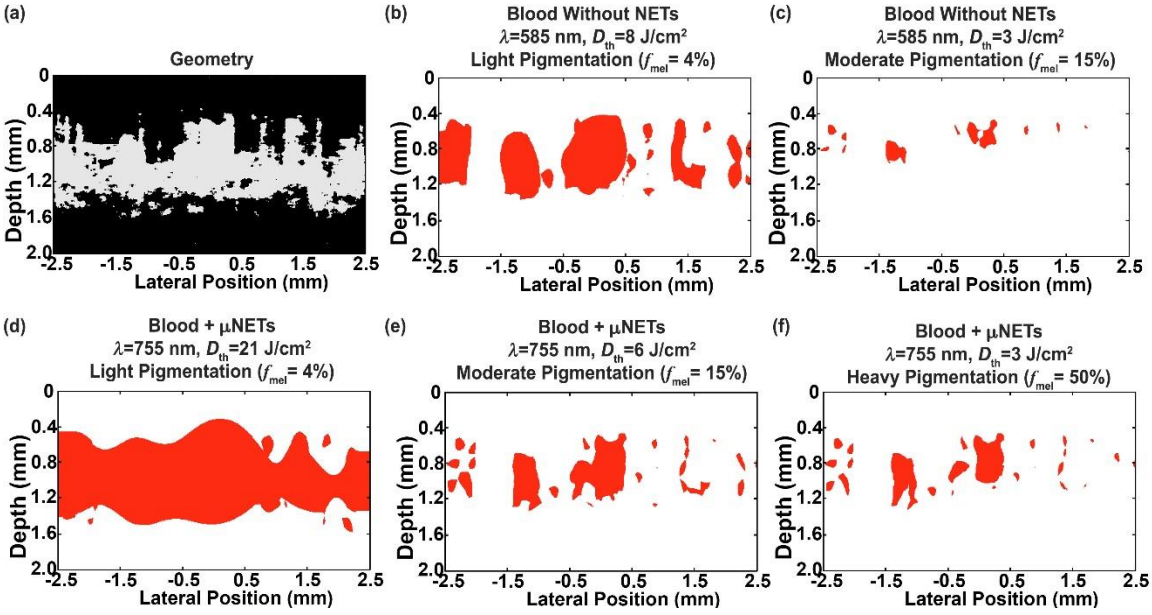

Figure 3.10 Two-dimensional *x*-*z* cross section of (a) human PWS obtained by OCT, and (b-f) damage to PWS blood vessels. Red regions correspond to values of $\Omega \geq 1$. Panels (b,c) present damage profiles in response to 585 nm laser irradiation without NETs for light (f_{mel} = 4%), and moderate (f_{mel} = 15%) pigmentation levels, respectively. Panels (d-f) present damage profiles in response to 755 nm laser irradiation in presence of μNETs for light (f_{mel} = 4%), moderate (f_{mel} = 15%), and heavy (f_{mel} = 50%) pigmentation levels, respectively. Parameters for patient PWS blood vessels containing μNETs were $\mu_{a,BV}$ = 6 mm^{-1}, f_{NETs} = 10% for panel (d), and $\mu_{a,BV}$ = 18 mm^{-1}, f_{NETs} = 25% for panels (e, f).

Use of free ICG in conjunction with pulsed 808 and 810 nm laser irradiation for treatment of patients with PWS has been reported.[11,12] While promising clinical results have been reported in these studies, delivering NETs to PWS blood vessels is more advantageous than free ICG as it provides a method to increase the circulation time of ICG, and can consequently, elongate the therapeutic window of time over which laser irradiation can be performed. For example, nano-constructs (≈ 80 nm diameter) composed of poly (lactic-co-glycolic acid) core coated with erythrocyte-derived membranes were retained in

blood for three days with circulation half-life of ≈ 8 hours in mice.[49] Piao et al reported that the circulation half-life of gold materials cloaked with erythrocyte membranes (≈ 90 nm diameter) was ≈ 9.5 hours.[107] Increased circulation time of erythrocyte-coated particles can be attributed to the presence of "self-marker" membrane proteins to allow evasion by immune cells.[38,39] One important "self-marker" membrane protein on the surface of the erythrocytes is CD-47 glycoprotein, whose interaction with immunoreceptor signal regulatory protein alpha (SIRPα), expressed by macrophages, results in inhibition of phagocytosis.[108] We previously demonstrated that CD-47 remains on the surface of the NETs,[48] providing a mechanism for increased circulation time of NETs. Furthermore, NETs can serve as a biocompatible and non-toxic platform for delivery of ICG. In a recent study, Rao et al reported the absence of systemic toxicity at 15 days post intravenous injection of erythrocyte membrane-coated upconversion nanoparticles in mice.[109]

Results of this theoretical study indicate that use of NETs in conjunction with pulsed 755 nm laser irradiation can provide a personalized approach for effective treatment of PWS blood vessels by customizing the optical properties of NETs to match the type of vascular plexus (e.g., depth, size, and distribution of blood vessels) and induce the necessary photothermal effects. The theoretical model presented in this study can be used in guiding the fabrication of NETs with appropriate level of ICG, and development of laser dosimetry parameters.

Conclusion

Using theoretical models, we have demonstrated that NETs can be beneficial for NIR laser treatment of PWS. NETs can be fabricated with patient-specific optical properties to allow

for a personalized treatment based on the size and depth of the blood vessels as well as the pigmentation of the individual's skin. The use of NIR lasers in combination with NETs addresses key challenges in vascular phototherapy by reducing epidermal damage and increasing penetration to deeper blood vessels.

Chapter 4

Erythrocyte-Derived Theranostic Nanoplatforms for Near Infrared Fluorescence Imaging and Photodestruction of Tumors

Abstract

Nanoparticles activated by NIR excitation provide a capability for optical imaging and photodestruction of tumors. We have engineered optical nanoconstructs derived from erythrocytes, which are doped with the FDA-approved NIR dye, ICG. We refer to these constructs as NETs. Herein, we investigate the phototheranostic capabilities of NETs for fluorescence imaging and photodestruction of SKBR3 breast cancer cells and subcutaneous xenograft tumors in mice. Our cellular studies demonstrate that NETs are internalized by these cancer cells and localized to their lysosomes. As evidenced by NIR fluorescence imaging and in vivo laser irradiation studies, NETs remain available within tumors at 24 h postintravenous injection. In response to continuous wave 808 nm laser irradiation at intensity of 680 mW/cm2 for 10−15 min, NETs mediate the destruction of cancer cells and tumors in mice through synergistic photochemical and photothermal effects. We demonstrate that NETs are effective in mediating photoactivation of Caspase-3 to induce tumor apoptosis. Our results provide support for the effectiveness of NETs as theranostic agents for fluorescence imaging and photodestruction of tumors and their role in photoinduced apoptosis initiated by their localization to lysosomes.

Introduction

Light-activated materials present a potential theranostic platform for image-guided phototherapy.[1,3,4] In particular, use of NIR wavelengths (≈ 750-1450 nm) is especially advantageous since relatively deep (≈ 2-3 cm) optical imaging and phototherapy can be achieved due to reduced light absorption and scattering by endogenous constituents. To-date, ICG remains as the only NIR-activated agent approved by FDA for specific clinical applications including ophthalmic angiography, cardiocirculatory measurements, assessment of hepatic function and blood flow evaluation.[7,8] ICG has also been investigated for potential applications ranging from sentinel lymph node mapping in patients with different types of cancer to imaging intracranial aneurysm and cerebral arteriovenous malformations.[10–12,14,16,17]

In addition to its optical imaging capabilities, ICG has also been investigated as a photosensitizer for photodynamic therapy of choroidal melanomas and breast adenocarcinomas.[18,87] as well as a photothermal agent for treatment of port wine stains.[19] However, ICG's major drawbacks are its short plasma half-life (≈ 3-5 minutes) and non-specific interactions with various biological macromolecules, particularly serum albumin and high density lipoproteins. To overcome these limitations, ICG has been encapsulated within various constructs, including micelles, liposomes, silica and synthetic polymers.[21,23–25,28,29]

Use of mammalian cells such as erythrocytes, lymphocytes, and macrophages, or constructs derived from them, are receiving increased attention as delivery platforms due to increased circulation time and biocompatibility.[32,34,107,109,110] For example, Hu et al

reported that nano-constructs (≈ 80 nm diameter) composted of poly (lactic-co-glycolic acid) core coated with erythrocyte-derived membranes were retained in blood for three days with circulation half-life of ≈ 8 hours in mice.[49] Piao et al have reported that the circulation half-life of gold nanocages cloaked with erythrocyte membranes (≈ 90 nm diameter) was ≈ 9.5 hours.[107] Rao et al did not observe systemic toxicity 15 days after intravenous injection of erythrocyte membrane-coated upconversion nanoparticles in mice.[109]

We previously provided the first report on the engineering of nano-sized vesicles derived from erythrocytes loaded with ICG, and their utility for fluorescence imaging and photo-destruction of HDME cells.[47] We refer to these constructs as NETs since once activated by NIR light, NETs can transduce the absorbing photons energy to generate heat, emit fluorescence, or mediate production of reactive oxygen species (ROS). Herein, we investigate the phototheranostic capabilities of NETs for near infrared fluorescence imaging and photodestruction of cancer cells and subcutaneous xenograft tumors in mice. We demonstrate that NETs remain available within tumors at 24 hours post intravenous injection, and mediate the destruction of cancer cells and tumors through synergistic photochemical and photothermal effects in response to continuous wave laser irradiation. We report for the first time that NETs are localized to cancer cells lysosomes, and upon photo-excitation can induce Caspase-3 activation, leading to tumor apoptosis.

Materials and Methods

Fabrication of NETs

Erythrocytes were separated from bovine whole blood (Rockland Immunochemicals, Inc., Limerick, PA) by centrifugation (5 minutes, 1,300xg, 4 °C). The supernatant, containing the plasma and buffy coat, was discarded and the resulting packed erythrocytes were washed twice with 1X (310 mOsm, pH ~ 8.0) PBS. Packed erythrocytes were then subjected to sequential hypotonic treatment with 0.5X PBS (155 mOsm, pH ~ 8.0) and 0.25X PBS (77.5 mOsm, pH ~ 8.0) respectively. The centrifugation process (20,000xg, 15 minutes, 4 $^{\circ}$C) was repeated until all the hemoglobin was depleted, resulting in an opaque white pellet containing micron-sized hemoglobin-depleted EGs.

To obtain nano-sized EGs, the micron-sized EGs were extruded 10 times through 800 nm polycarbonate porous membranes (Nuclepore Track-Etched Membranes, Whatman, Florham Park, New York), followed by 10 more extrusions through 400 nm polycarbonate membranes, and another 10 times through 200 nm polycarbonate membranes using an extruder (LIPEX Extruder, TRANSFERRA Nanosciences Inc, Burnaby, Canada). To concentrate the nano-sized EGs, 10 ml of nano-sized EGs were centrifuged (99,000xg, 1 hour, 4 $^{\circ}$C) and re-suspended in 1 ml of 1X PBS.

To load ICG into nano-sized EGs, 1 ml of nano-sized EGs solution, concentrated by 10 times, was incubated with 3 ml of ICG dissolved in water (at concentration of 2 mg/ml) and 3 ml of hypotonic buffer (Na_2HPO_4/ $Na_2H_2PO_4$, 140 mOsm, pH ~ 5.8), resulting in 6 mg of ICG in 7 ml of the loading buffer. The corresponding concentration of ICG in this loading buffer was ≈ 1.1 mM (considering the molecular weight of ICG as ≈

775 Da). The suspension was incubated for five minutes at 4 °C in dark, centrifuged at 74,000xg for 30 minutes, and then washed three times using 1X PBS to remove any non-encapsulated ICG. The pellet containing ICG-encapsulated EGs (i.e., NETs) was removed and re-suspended in 1 ml of 1X PBS (4 $^{\circ}$C). To avoid saturation in measurements of NIR absorbance values during absorption spectral recordings, this solution of NETs was further diluted by a factor of 80 using 1X PBS. We then acquired the absorption spectrum of the 1:80 diluted solution of NETs.

Next, we proceeded to estimate the free ICG equivalent concentration within the population of NETs [ICG_{NETs}] as follows. We first acquired the absorption spectra of ICG dissolved in water at concentrations in the range of 2-10 μM. We chose water as the solvent since the absorption spectra of NETs resembles that of ICG dissolved in water at concentrations less than ≈ 20 μM. The spectra were then spectrally integrated in the range of 600-900 nm, and the resulting values (A_{int}) were plotted against ICG concentrations to obtain a calibration curve (R^2 = 0.99). We then used the value of A_{int} associated with the 1:80 diluted solution of NETs in conjunction with the calibration curve to estimate [ICG_{NETs}] ≈ 12.25 μM. Finally, we estimated [ICG_{NETs}] for the undiluted NETs to be ≈ 980 μM as the product of 12.25 μM and the dilution factor 80. In a similar fashion, we prepared various dilutions of the NETs solution with values of [ICG_{NETs}] ≈ 2, 10, 18, 36, 72 and 144 μM.

Characterization of NETs

The hydrodynamic diameters of NETs suspended in 1X PBS were measured by dynamic light scattering (DLS) (Zetasizer NanoZS90, Malvern Instruments Ltd, Malvern, United

Kingdom). The absorption spectra of NETs ([ICG_{NETs}] ≈ 10 μM) and 13 μM free ICG suspended in 1X PBS were obtained using a UV-visible spectrophotometer (Cary 50 UV-Vis spectrophotometer, Agilent Technologies, Santa Clara, CA) with optical path length of 1 cm. The fluorescence emission spectra of NETs ([ICG_{NETs}] ≈ 2 μM) and 4 μM free ICG were acquired in response to 720 ± 2.5 nm, and recorded using a fluorimeter (Fluorolog-3 spectrofluorometer, Edison, NJ). We normalized the fluorescence emission spectra ($\chi(\lambda)$) as:

$$\chi(\lambda) = \frac{F(\lambda)}{(1\text{-}10^{-A(\lambda_{ex})})} \tag{4.1}$$

where A and F are the wavelength (λ) dependent absorbance and intensity of the emitted fluorescence light, respectively, and λ_{ex} is the excitation wavelength.

Photostability of NETs

NETs suspended in PBS ([ICG_{NETs}] ≈ 18 μM) and 22 μM of ICG dissolved in PBS were prepared. Samples were then laser-irradiated at 808 nm using intensity (I_o) value of 680 mW/cm^2 (9 mm diameter focal spot) for durations (t_{laser}) ranging between 1-15 minutes. Immediately following each experiment at a given t_{laser}, we acquired the absorption spectra of the samples, and normalized them to the absorbance value at 808 nm ($A(\lambda)$ = 808nm)) prior to laser irradiation (defined as time t_0).

Detection of singlet oxygen generation

We used 10 μM 1,3-diphenylisobenzofuran (DPBF) as a probe to detect the generation of singlet oxygen ($^1O_2$) in response to 808 nm photo-excitation of 11 μM free ICG or NETs

([ICG_{NETs}] ≈ 18 μM). DPBF has an absorption peak at 411 nm in DMF.[111] Upon reacting with $^1O_2$, DPBF undergoes 1,4-cycloaddition to form an endoperoxide product, resulting in decreased 411 nm absorption. Samples were irradiated at I_o = 680 mW/cm^2 for 10 seconds. An aliquot of sample was then withdrawn and the absorbance at 411 nm was recorded using a UV-visible spectrophotometer. The absorbance value at 411 nm was normalized to the absorbance value at 411 nm prior to laser irradiation. In the negative control experiment, DPBF solution without NETs or free ICG was irradiated at I_o = 680 mW/cm^2, and the 411 nm absorbance values were determined and normalized as above.

Cell culture

SKBR3 human breast cancer cells (ATCC®, Manassas, VA) were cultured in Rosewell Park Memorial Institute (RPMI) 1640 medium (Mediatech Inc, Manassas, VA) supplemented with 10% fetal bovine serum (FBS) and 1% Penicillin/Streptomycin (Corning Inc., Corning, NY) at 37 °C in 5% humidified CO_2. Cells were used for *in vitro* experiments, and implanted in mice to induce tumors.

Assessment of NETs uptake by SKBR3 cancer cells

We used bright-field and NIR fluorescence imaging, flow cytometry, and laser scanning confocal fluorescence microscopy (LSCFM) to evaluate the uptake of NETs by SKBR3 cancer cells. Cells were cultured in 96-well plates for NIR fluorescence imaging, and 12-well plates for flow cytometry. For LSCFM, cells were grown on poly-l-lysine coated coverslips in 12-well plates. After 24 hours, cells were incubated in RPMI medium containing PBS (negative control), NETs ([ICG_{NETs}] ≈ 36 μM) or 44 μM free ICG (positive

control) for 3 hours. Cells were then washed three times with PBS prior to imaging or flow cytometry.

NIR fluorescence emission (> 770 nm) in response to 740 ± 35 nm excitation by a Nikon Mercury/Xenon arc lamp was captured by an electron multiplier gained charge-coupled device (EM-CCD) camera (Quant EM-CCD, C9100-14 Hamamatsu, Shizuoka-ken, Japan). The camera exposure time was set at 0.7 seconds for NIR fluorescence emission and 0.03 seconds for bright-field images and gain of 1.0. We present falsely colored microscopic images with NIR fluorescent emission due to ICG (red channel) merged with bright-field (gray channel).

For flow cytometry experiments, the RPMI medium was removed, and cells were incubated with trypsin for 5 minutes. After incubation, fresh RPMI was added to halt trypsinization, and cells were subsequently centrifuged at 125xg for 5 minutes. The supernatant was removed, and the pellet was then re-suspended in 1X PBS. A flow cytometer (BD FACSAria cell sorter, San Jose, CA) with photo-excitation at 633 nm and emission collection at > 785 nm was used to measure the NIR signals from cells that had been incubated with PBS, NETs or free ICG. All studies were done using three different samples. During flow cytometry, a minimum of ≈10,000 events were counted for each triplicate within the gating region.

For LSCFM experiments, the RPMI medium was removed after incubating the cells with NETs, and cells where then incubated with LysoTracker yellow® HCK-123 (Invitrogen, Carlsbad, CA) for two hours. Immediately after staining with LysoTracker, we fixed and permeated the cells using 4% paraformaldehyde and 2% tween 20,

respectively. We then mounted the slide with ProLong^{TM} Gold Antifade containing 4',6-diamidino-2-phenylindole (DAPI) (Invitrogen, Carlsbad, CA) and used a confocal microscope (Leica SP5, Leica Microsystems Inc., Buffalo Grove, IL) with photo-excitation at 405, 488 and 633 nm, corresponding to DAPI, LysoTracker, and ICG absorption respectively. Fluorescence emission were collected at 420-480, 500-610 and > 655 nm, respectively. We present falsely colored microscopic images corresponding to DAPI (blue channel), and LysoTracker yellow emission (green channel), and ICG NIR emission (red channel). For co-localization analysis, we used ImageJ to calculate the pixel intensity correlation using the two methods, Pearson and Costes.[112]

Laser irradiation of SKBR3 cancer cells

To investigate the photo-destructive capability of NETs, SKBR3 cells were cultured in a 96-well. After 24 hours, cells were incubated with RPMI medium containing PBS, free ICG (44 and 176 μM), or NETs (with specific value of $[ICG_{NETs}]$ = 18, 36, 72, or 144 μM) for three hours in dark at 37 °C. After incubation, cells were then washed three times with PBS and fresh medium was added. We subsequently irradiated the cells at 808 nm using I_o values of 680 mW/cm^2 for 15 minutes.

To assess the viability of cells following laser irradiation, cells were incubated in RPMI medium containing 2 μM Calcein-AM and 4 μM Ethidium Homodimer-1 (EthD-1) (ThermoFisher Scientific, Waltham, MA) as the respective live/dead assays for 30 minutes. Cells were then washed with PBS and fluorescently imaged in response to Calcein-AM excitation at 485 ± 35 nm and EthD-1 excitation at 543 ± 22 nm excitation by a Nikon Mercury/Xenon arc lamp. Respective fluorescence emission over the spectral bands of 524

± 24 nm and 593 ± 40 nm were captured by an EM-CCD camera with exposure time set at 0.03 seconds. We present falsely colored microscopic images with Calcein-AM fluorescent emission (green channel) overlaid with EthD-1 fluorescence emission (red channel). Cell viability in each well was calculated using a fluorescent microplate reader (Molecular Devices FlexStation II 384, Harlow Scientific).

To detect the presence of ROS in response to NIR laser irradiation of SKBR3 cancer cells, we used the molecular probe 2',7'-dichlorofluorecein diacetate (DCFH-DA) (Sigma-Aldrich, St. Louis, MO). Once the non-fluorescent DCFH-DA is oxidized by ROS, it is converted into a fluorescent molecule 2',7'-dichlorofluorescein (DCF).[113] In a subset of experiments, cells treated with PBS, 18 μM NETs and 22 μM free ICG for three hours (as described above) were further incubated with 25 μM DCFH-DA in RPMI medium for 30 minutes prior to laser irradiation at the parameters indicated above. Following irradiation, we imaged the cells in bright-field and fluorescence modes. The DCF fluorescence emission (524 ± 24 nm) in response to 485 ± 35 nm excitation by a Nikon Mercury/Xenon arc lamp was captured by an EM-CCD camera. The camera exposure time was set at 0.2 seconds for DCF fluorescence emission and 0.03 seconds for bright-field images and gain of 1.0. We present falsely colored microscopic images with DCF fluorescent emission (green channel) merged with bright-field (gray channel).

To determine if ROS included $^1O_2$ as a constituent, we used sodium azide as a $^1O_2$ quencher probe.[114] In a subset of experiments, we pre-treated the SKBR3 cells with DCFH-DA (as described above), washed them after 30 minutes, and then incubated them in RPMI

medium containing 50 mM sodium azide for 45 minutes prior to laser irradiation at the indicated parameters above.

Animal study

Female Nu/J mice (20~25 g; 6-8 weeks) were purchased from Jackson Laboratory (Bar Harbor, Maine) and utilized in this study under a protocol approved by the University of California, Riverside Institutional Animal Care and Use Committee (A-20140022). We injected $\approx 1 \times 10^7$ SKBR3 cancer subcutaneously into the thighs. Mice were monitored until the tumor sizes reached approximately 15 mm^3. The tumor volume was calculated as $D \times d^2/2$, where D and d were the larger and smaller diameter of each tumor.

Tumor-bearing mice were randomly divided into three groups with four animals in each group. Group 1 received PBS injection without laser irradiation. Group 2 received PBS injection and 808 nm laser irradiation using I_o = 680 mW/cm^2 for 10 minutes. Group 3 received NETs [$ICG_{NETs} \approx 980$ μM] injection and 808 nm laser irradiation using I_o = 680 mW/cm^2 for 10 minutes. We administered 100 μl of PBS or NETs intravenously via tail-vein injection while the animal was anesthetized. Laser irradiation was performed at 24 hours post injection of PBS or NETs with a beam diameter of 9 mm. We measured the temperature change in response to laser irradiation by inserting a mini-hypodermic thermocouple (0.2 mm thermocouple diameter) (HYP0, OMEGA, Norwalk, CT) connected to a LabQuest® data acquisition system (Vernier, Beaverton, OR) ≈ 1 mm below the skin and about 2 mm outside the laser-irradiated spot. Following the experimental procedures, animals were allowed to recover. We assessed the efficacy of NETs in mediating photo-induced reductions in tumor size by measuring the tumor volumes

following each treatment at every two days intervals and for up to 16 days after laser irradiation. We estimated the relative tumor volumes (V/V_o) during this time interval by dividing the volume of each tumor (V) on the measurement day divided by the initial tumor volume (V_o) on the day of laser irradiation. Animals were subsequently euthanized on day 16 following laser irradiation.

In a subset of experiments, an animal from each group was euthanized immediately after laser irradiation. Tumors were removed and frozen at -80 °C for later analysis. Approximately, ≈ 7 days later, tumors were thawed and sectioned in 10 μm thicknesses using a cryostat microtome (CM1950 cryostat, Buffalo Grove, Illinois) and stained with fluorescein isothiocyanate (FITC)-labeled Caspase-3 antibody (BD Biosciences, San Jose, CA) as an established method to assay for cell apoptosis.[115–117] Fluorescent emission (524 ± 24 nm) in response to 485 ± 35 nm excitation by a Nikon Mercury/Xenon arc lamp was captured by an EM-CCD camera with exposure time set at 0.2 seconds. Mean and SDs of the image intensities (n = 5 images) were quantified using ImageJ.

To evaluate the feasibility of NETs in tumor imaging, in a subset of experiments, 100 μl of PBS or NETs [$ICG_{NETs} \approx 980$ μM] were administered by tail vein injection. At 24 hours post injection, animals were euthanized, and tumors extracted. Extracted tumors were fluorescently imaged in a dark box. Two light emitting diodes (LEDs) delivering 700 ± 30 nm excitation light were used for illumination. Fluorescence emission was captured using a CCD camera (Pixis 1024B, Roper Scientific, Trenton, NJ) equipped with a long pass filter transmitting wavelengths greater than 810 nm. To prevent pixel saturation, the camera exposure time was set to 90 seconds.

Results and Discussion

Characterization of NETs

The mean peak hydrodynamic diameter of NETs as estimated by dynamic light scattering (DLS) was ≈ 79 nm (**Figure 4.1a**). We used lognormal fits to estimate the mean ± standard deviation (SD) diameter of NETs as 85 ± 1 nm. We have previously published transmission electron[47] and scanning electron[48] microscopic images of NETs, and demonstrated that DLS-based measurements of NETs' diameters are consistent with those made by electron microscopy. The polydispersibility index (PDI) value for this set of NETs was 0.2, meaning that the standard deviation in diameter is 20% of the mean value. Nanoparticles with PDI values in the range of 0.1~0.4 are considered as moderately polydispersed.[67] Since the hydrodynamic diameters of NETs are < 200 nm, they are likely to be effective for extravasation into tumors through the EPR effect, induced by the leaky tumor vasculature and impaired lymphatic drainage.[50,51]

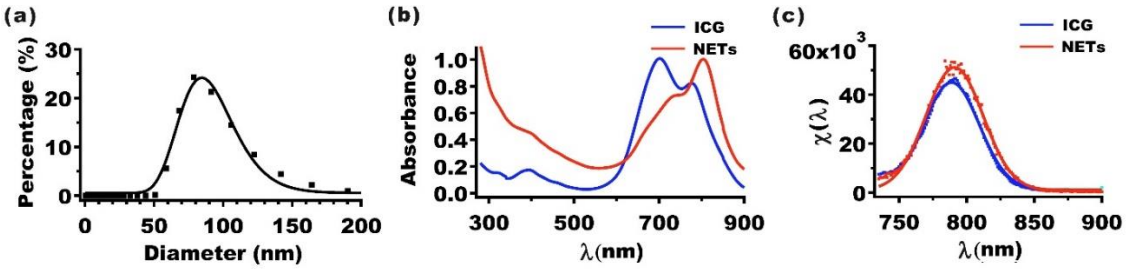

Figure 4.1 Characterization of NETs. (a) Hydrodynamic diameter distribution of NETs as determined by DLS. Circles and error bars (too small to be seen) represent the mean and standard deviations of diameters, respectively (n = 4 measurements). The estimated mean diameter as determined from the lognormal fits (solid curves) is ≈ 85 nm. (b) Absorption spectra of 13 μM free ICG, and NETs ([ICG_{NETs}] ≈ 10 μM). (c) Normalized fluorescence emission spectra ($\chi(\lambda)$) (see equation 4.1)) (circles) and Gaussian fits (solid curves) of 4 μM free ICG and NETs ([ICG_{NETs}] ≈ 2 μM) in response to photo-excitation at 720 ± 2.5 nm. Solvent used in spectral recordings was 310 mOsm PBS.

The absorption spectrum of free 13 μM ICG dissolved in ≈ 310 mOsm phosphate buffer saline (PBS) (defined as the 1X PBS), and NETS fabricated using 1.1 mM ICG in the loading buffer are shown in **Figure 4.1b**. The free ICG equivalent concentration loaded into these NETs [ICG_{NETs}] was estimated as ≈ 10 μM (see EXPERIMENTAL SECTION). Absorption spectrum of free ICG exhibited primary and secondary peaks at 698 and 776 nm, associated with the H-like aggregate and monomeric forms of ICG, respectively.[69] In contrast, NET, suspended in 1X PBS, showed a dominant spectral peak at 804 nm, suggesting that the monomeric ICG was the dominant form within these NETs. The bathochromic (red) spectral shift in the monomeric absorption of free ICG from 776 nm to 804 nm in NETs is consistent with our previous results.[47,48,90] This shift can be attributed to the binding of ICG molecules to phospholipids and membrane proteins of the NETs, causing a change in the molecular energy levels of ICG, as well as the local solvent environment surrounding ICG within the NETs.[69,119]

In response to photo-excitation at 720 ± 2.5 nm, the normalized fluorescence emission spectra ($\chi(\lambda)$) (see **equation 4.1**) of 4 μM free ICG and NETs ([ICG_{NETs}] ≈ 2 μM) showed respective peaks at 792 and 796 nm, associated with the monomer form respectively (**Figure 4.1c**). The normalized fluorescence emission spectra had a similar bathochromic shift from 792 nm (associated with monomer form of free ICG) to 796 nm (associated with emission from the monomeric form of ICG in NETs). Peak value of $\chi(\lambda)$ for NETs was ≈ 15% higher than that of free ICG. This increase may be due to reduced self-aggregation of ICG as a result of its binding to proteins and lipids in the membrane

shell of NETs. Similar fluorescent enhancement has been reported for ICG binding to lipids,[25] proteins in fetal bovine serum,[69] and albumin.[120]

Photostability and NETs-mediated singlet oxygen generation

To gain insight on photostability of ICG in both free and nano-encapsulated formulations, we acquired their respective absorption spectra immediately after being laser irradiated at 808 nm with incident intensity (I_o) of 680 mW/cm^2 for up to 15 minutes (**Figure 4.2a**). We prepared solutions of free ICG (22 μM) and NETs ([ICG_{NETs}] ≈ 18 μM) in 1X PBS so that the absorbance values for both free ICG and NETs at 808 nm were 1.8. With increasing laser irradiation times, there were corresponding reductions in the absorption spectra (**Figure 4.2a**). These reductions can be attributed to photo-induced chemical modification of ICG molecules to produce a leuco form of the dye with converted sp^2 to sp^3 carbon hybridization, and/or induce cleavage of the π–conjugation along the polyene segment of the dye while keeping the aromatic benzoindotricarbocyanine moieties intact.[47] At 808 nm, free ICG had the lowest percentage decrease in its absorbance values as compared with NETs (**Figure 4.2b**). For example, after 15 minutes of irradiation, the 808 nm absorbance values of free ICG and NETs irradiated at 680 mW/cm^2 decreased by 26.2, and 60.0%, respectively. Greater reductions in 808 nm absorbance values of NETs upon laser irradiation may be due to induced molecular conformational changes in ICG as a result of nano-encapsulation.

We used 1,3-diphenylisobenofuran (DPBF) as a probe to assess the generation of $^1O_2$ in response to 808 nm photo-excitation of free ICG and NETs (see EXPERIMENTAL SECTION). Laser irradiation of DMF-dissolved DPBF at I_o = 680 mW/cm^2 for up to 80

seconds did not alter the absorbance value at 411 nm (**Figure 4.2c**), confirming that there was no photo-induced production of $^1O_2$ in the absence of NIR absorbing molecules or particles. However, in presence of free ICG or NETs, the normalized DPBF absorbance at 411 nm progressively decreased with increased 808 nm laser irradiation time (**Figure 4.2c**). Generation of $^1O_2$ is consistent with the type II photochemistry where the intersystem crossing of ICG (in free or nano-encapsulated form) to the excited triplet state is followed by energy transfer to the ground state molecular oxygen, producing $^1O_2$.

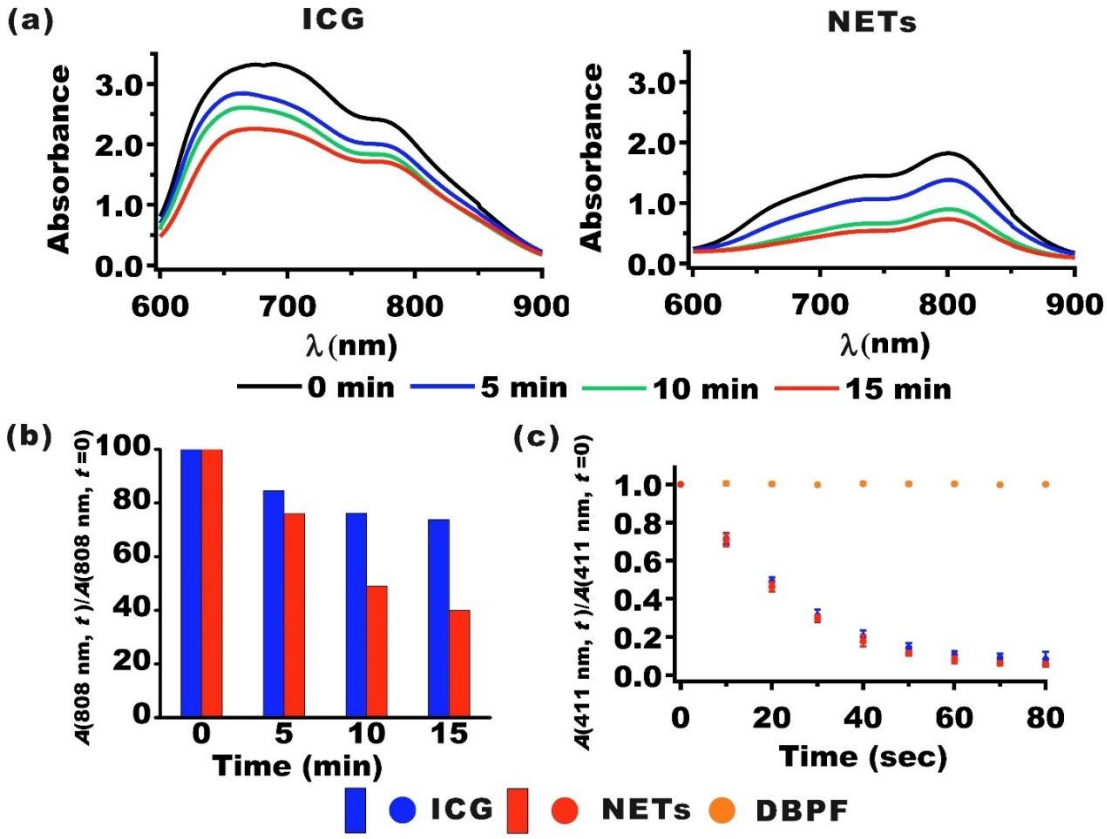

Figure 4.2 Photostability and $^1O_2$ generation of NETs in solution. (a) Absorption spectra of 22 μM free ICG, and NETs ($[ICG_{NETs}] \approx 18$ μM) before and after 808 nm laser irradiation (I_o = 680 mW/cm^2) for 5, 10, and 15 minutes. (b) Normalized 808 nm absorbance values for ICG and NETs as a function of 808 nm laser irradiation time. (c) Normalized 411 nm absorbance values for solutions containing 10 μM DPBF without, or with 11 μM ICG or NETs ($[ICG_{NETs}] \approx 18$ μM) as a function of 808 nm laser irradiation time. Data points and error bars in panel (c) represent the mean and SDs for n = 4 samples.

Fluorescence imaging of SKBR3 breast cancer cells incubated with NETs

SKBR3 human breast cancer cells were incubated at 37 °C with PBS (negative control), 44 μM free ICG (positive control) or NETs ($[ICG_{NETs}] \approx 36$ μM) for three hours. Following incubation, cells were washed, and then fluorescently imaged. While there were none or minimal NIR fluorescence emission from SKBR3 cells incubated with PBS or free ICG, NETs-incubated cells emitted NIR fluorescence (**Figure 4.3a**).

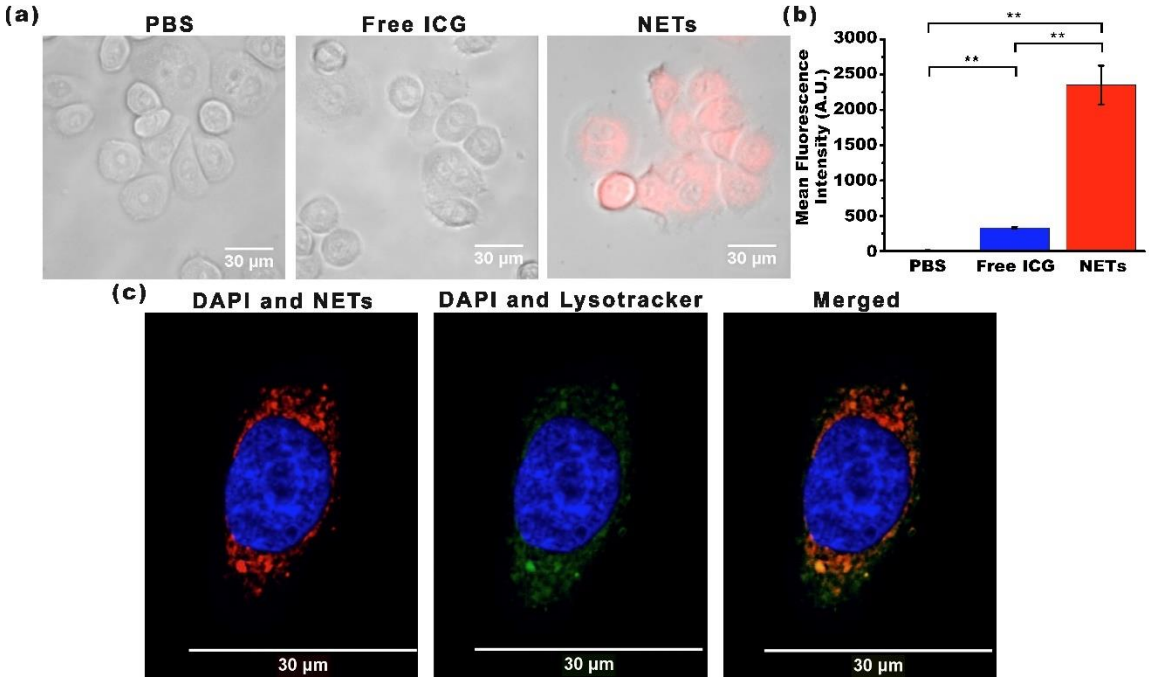

Figure 4.3 Uptake of NETs by SKBR3 cancer cells. (a) Merged bright-field and fluorescent images of SKBR3 cancer cells following three hours of incubation at 37 °C with PBS, 44 μM free ICG or NETs ($[ICG_{NETs}] \approx 36$ μM). Images are falsely colored. Red channel: NIR emission due to ICG; Gray channel: bright-field. (b) Uptake analysis of SKBR3 cells by flow cytometry. Geometric mean fluorescence intensity (n = 3 different samples) (**) $p < 0.01$. (c) Laser scanning confocal fluorescent images of a SKBR3 cell following three hours of incubation at 37 °C with NETs. Images are falsely colored. Blue channel: DAPI; Green channel: Lysotracker; Red channel: NIR emission due to ICG from NETs.

Flow cytometry results confirmed that the mean fluorescence intensity of cells incubated with NETs were significantly higher than those associated with cells incubated with free ICG or PBS (n = 3, $p < 0.01$) (**Figure 4.3b**). These results further validate that NETs were effectively uptaken by the cells, whereas most of ICG was removed as a result of washing the cells. These results demonstrate that NETs serve as an effective platform to deliver their cargo (ICG) to cancer cells.

To determine the cellular localization of NETs, we used 4',6-diamidino-2-phenylindole (DAPI) and Lysotracker, fluorescent probes that respectively stain the nucleus and lysosomes, and imaged the cells by laser scanning confocal fluorescence microscopy (LSCFM) (**Figure 4.3c**). Lysotracker and ICG fluorescence from NETs spatially overlapped, suggesting that NETs were localized to lysosomes of the cells, and positioned at the periphery of the nucleus. Our analysis of the images indicated Pearson's value of $R = 0.99$, confirming that the intensity distributions were highly correlated. Similarly, Costes' P value of 1.00 confirmed the co-localization of the intensities from each pixel. Although not investigated here, it is possible that NETs may also accumulate in mitochondria. For example, it has been demonstrated that an analog form of ICG, consisting of a cyclohexenyl substitution in the middle of the polymethine linker and two asymmetrical amphipathic N-alkyl side chains, accumulated in the mitochondria of MCF-7 and 4T1 breast cancer cells.[121] In another study, localization of magnetic complex nanoparticles loaded with ICG to the mitochondria of A549 adenocarcinomic alveolar basal epithelial cell line was reported.[122]

Laser irradiation of SKBR3 breast cancer cells incubated with NETs

SKBR3 cells were incubated at 37 °C with PBS (negative control), 176 μM free ICG (positive control) or NETs ($[ICG_{NETs}] \approx 144$ μM) for three hours. Following incubation, cells were washed and then irradiated at 808 nm for 15 minutes using $I_o = 680$ mW/cm^2.

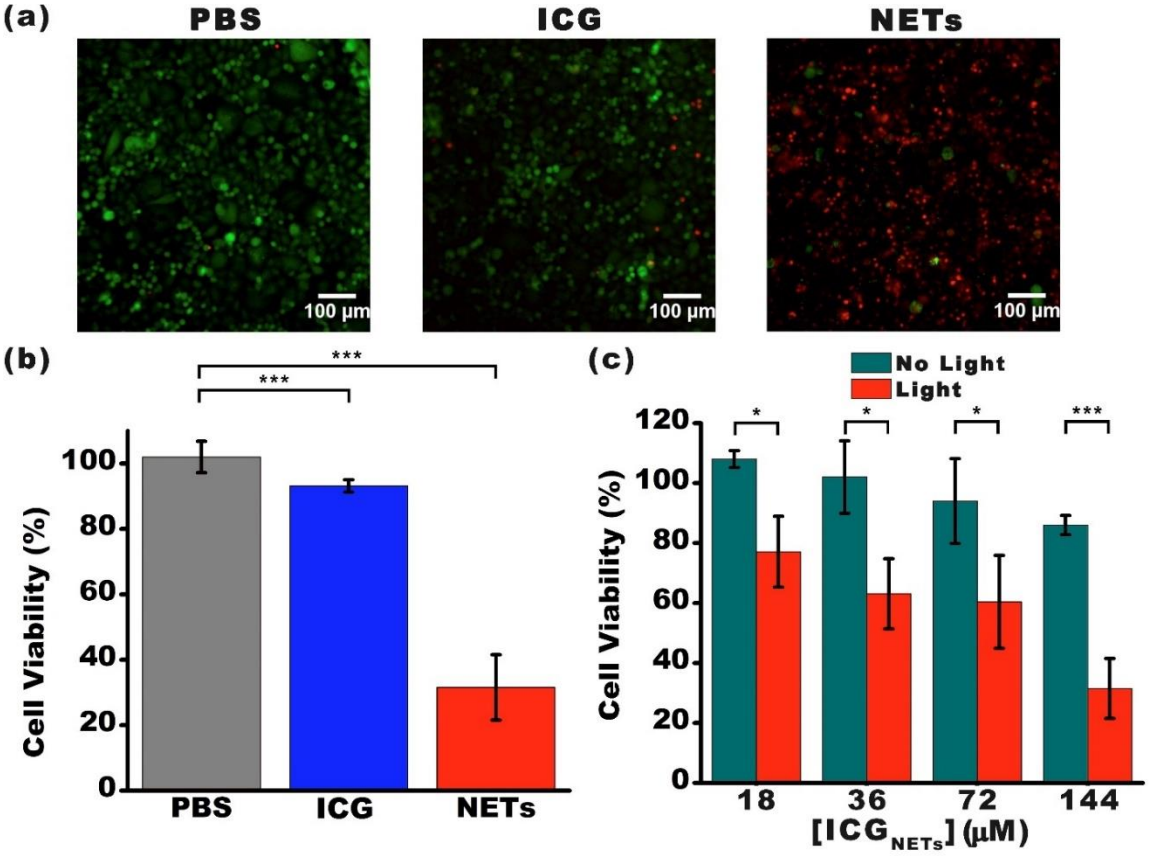

Figure 4.4 Photo-destruction of SKBR3 cancer cell *in vitro*. (a) Fluorescent images of SKBR3 cancer cells incubated with PBS (negative control), 176 μM free ICG (positive control), and NETs ($[ICG_{NETs}] \approx 144$ μM) for three hours at 37°C and followed by 808 nm laser irradiation at $I_o = 680$ mW/cm^2 for 15 minutes. Live cells were identified by the Calcein AM stain, and falsely colored in green. Dead cells in response to laser irradiation were identified using the Ethidium homodimer-1 stain, and falsely colored in red. (b) Percentage viability of SKBR3 cells as a function of incubation agent. (c) Percentage viability of SKBR3 cells as a function of $[ICG_{NETs}]$. In panels (b) and (c), statistically significant differences are indicated as (*) $p < 0.05$ and (***) $p < 0.001$ (n = 3 samples for each treatment).

We evaluated the viability of the cells following laser irradiation. Cells were stained with Calcein acetoxymethyl (AM) and ethidium homodimer-1 (EthD-1) to fluorescently visualize the live and dead cells, respectively (**Figure 4.4a**). In response to laser irradiation, ≈ 93% of ICG-treated SKBR3 cells remained viable. However, only 32% of NETs-treated cells were viable after laser irradiation at these parameters (**Figure 4.4b**).

We also evaluated the effects of [ICG_{NETs}] on photo-destruction of SKBR3 cells. The fraction of cell death progressively increased as [ICG_{NETs}] increased (**Figure 4.4c**). With increased [ICG_{NETs}] from 18 μM to 144 μM, the fractions of cells death increased from 23% to 69% for SKBR3 cells incubated with NETs.

To investigate if ROS production was a contributing mechanism to photo-induced destruction of SKBR3 cells, we used the molecular DCFH-DA (see EXPERIMENTAL SECTION). Cells incubated with NETs showed DCF fluorescence whereas the incubation of cells with PBS or ICG did not result in any noticeable DCF fluorescence emission (**Figure 4.5a**). These results indicate that NETs were uptaken by SKBR3 cancer cells, and mediated ROS production in response to laser irradiation.

To determine if ROS included $^1O_2$ as a constituent, we used sodium azide as an $^1O_2$ quencher (see EXPERIMENTAL SECTION).[114] Upon pre-treatment with sodium azide, the DCF fluorescence emission from SKBR3 cells incubated with NETs was quenched after laser irradiation, indicating the DCF emission from cells not treated with sodium azide was associated with $^1O_2$ production in response to laser irradiation.

Collectively, our *in vitro* results based on analysis of cell viability (**Figure 4.4**) and the use of molecular probes for ROS detection (**Figure 4.5**) support the presence of a photo-

chemical mechanism in destruction of cancer cells incubated with NETs and laser-irradiated at 808 nm using I_o = 680 mW/cm^2 for 15 minutes.

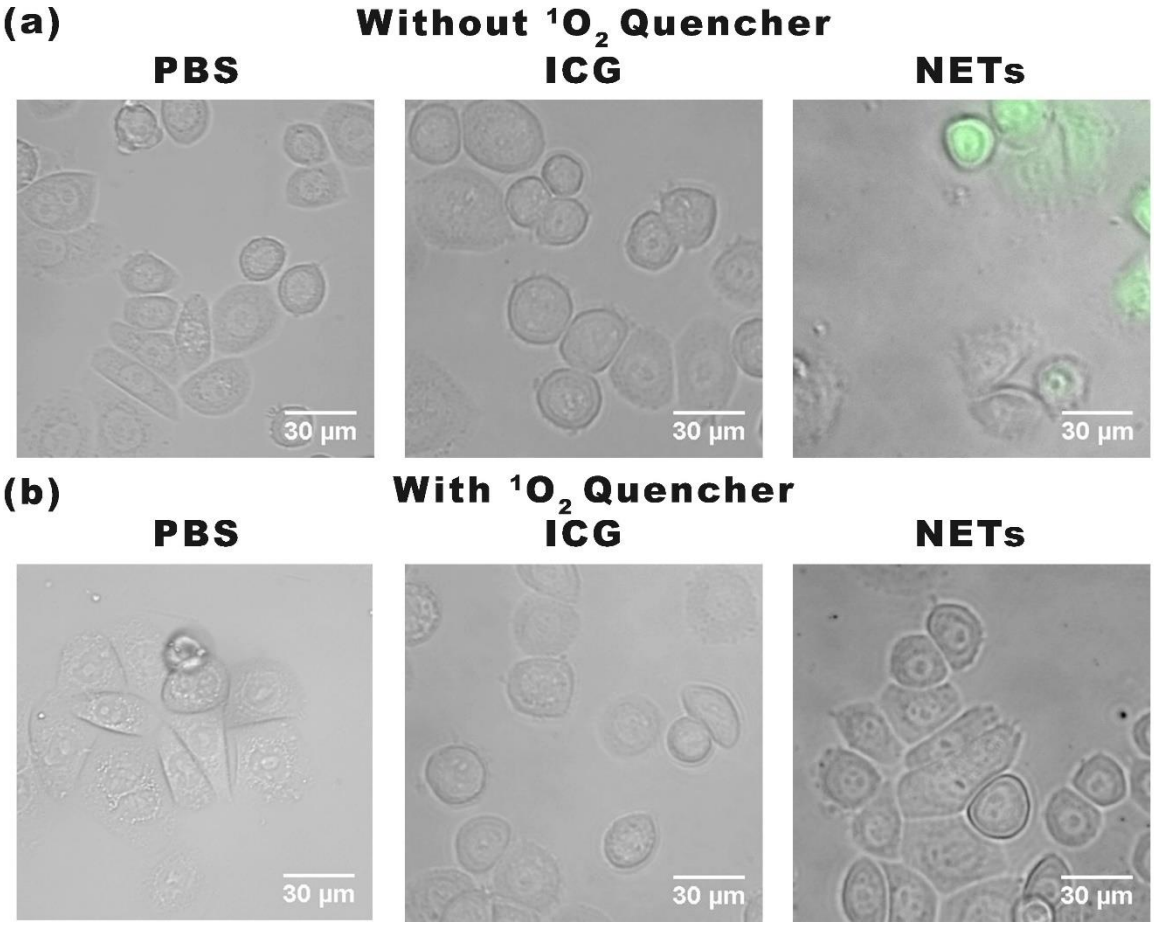

Figure 4.5 Detection of ROS generation by cell imaging. We present merged bright-field and DCF fluorescence images of SKBR3 cancer cells incubated with PBS, 44 μM free ICG, or NETs ([ICGNETs] ≈ 36 μM) for three hours and subsequently irradiated at 808 nm for 15 minutes at I_o = 680 mW/cm^2. Images correspond to (a) without and (b) and with application of $^1O_2$ quencher, sodium azide. Images are falsely colored. Gray channel: bright-field. Green channel: fluorescence emission from DCF.

NIR fluorescence imaging and laser irradiation of tumors

We investigated the efficacy of NETs in NIR fluorescence imaging of tumors. Tumors were extracted 24 hours after tail vein injection of PBS (control) or NETs ([ICG_{NETs}] ≈ 980 μM), and were immediately imaged by NIR photo-excitation and collecting the

fluorescence emission. NETs offered the capability to image the tumor (**Figure 4.6a**), indicating that they were present within the tumor at 24 hours post-injection. These results show that encapsulation of ICG within erythrocyte-derived nano-vesicles provided an effective method to prolong the circulation of ICG, and making it available for an intended application (e.g., tumor imaging) for at least 24 hours.

We assessed the capability of NETs in mediating photo-destruction of xenograft tumors implanted subcutaneously in mice. Laser irradiation was done 24 hours after intravenous injection of NETs via the tail vein. To investigate if there was a photothermal effect during laser irradiation, we recorded the *in vivo* temperature changes using a thermocouple needle probe inserted at ≈ 1 mm below the skin and ≈ 2 mm outside the laser-irradiated spot. Laser irradiation at I_o = 680 mW/cm^2 resulted in temperature rise of ≈ 11°C at the end of the 10 minutes of irradiation time (**Figure 4.6b**). This temperature rise under-estimates the actual temperature distributions within the tumor, and is a measure of the heat diffusion from the irradiated tumor site. Nevertheless, these measurements suggest that there was a photothermal effect during laser irradiation.

To investigate the presence of cellular apoptosis in response to laser irradiation, some of the tumors were extracted immediately after laser irradiation, and imaged by fluorescent immuno-staining to detect the presence of Caspase-3. As evidenced by fluorescence emission, there was Caspase-3 activation in mice injected with NETs and irradiated at 680 mW/cm^2 for 10 minutes (**Figure 4.6c**). Analysis of these images confirmed that NETs were effective in mediating photo-induced activation of Capase-3 as evidenced by statistically significant higher values of fluorescence intensity associated

with Caspase-3 (**Figure 4.6d**). Results of *in vivo* laser irradiation of tumors provide further evidence that NETs remained in circulation for at least 24 hours.

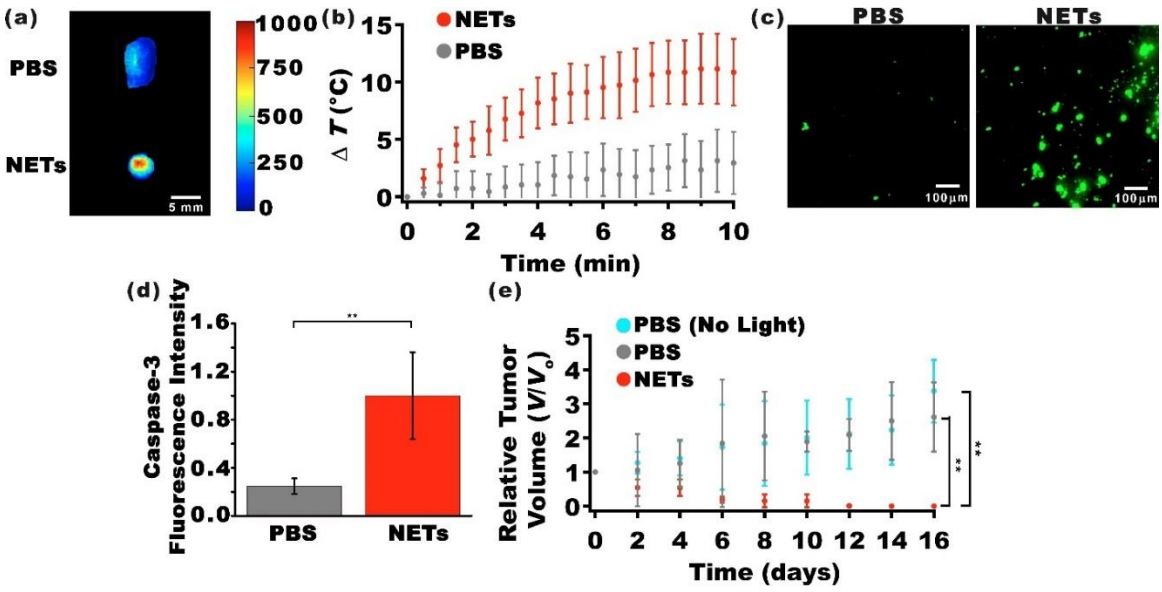

Figure 4.6 NIR fluorescence imaging and photo-destruction of xenograft tumors in mice. (a) NIR fluorescence images of tumors extracted 24 hours after tail injection of PBS (top panel), and NETs ($[ICG_{NETs}] \approx 980$ μM) (bottom panel). Scale bar on the right corresponds to fluorescent intensity (photo-excitation at 700 ± 30 nm, and emission > 810 nm collected). (b) Temperature rise as a function of laser irradiation time as measured by a thermocouple needle probe placed ≈ 1 mm below skin surface and ≈ 2 mm outside the irradiated spot. (c) Fluorescent images of sectioned tumors by immunostaining using FITC-labeled Caspase-3 antibody. (d) Fluorescence emission intensity associated with FITC-labeled Caspase-3 antibody as the apoptosis indicator following laser irradiation. (e) Estimated relative change in tumor volumes (V) of non-orthotopic xenograft tumors in mice with respect to the volumes at time zero (V_o). Time zero is with respect to the day of laser irradiation. Mice were injected via the tail vein with either 100 μL of PBS, or NETs ($[ICG_{NETs}] \approx$ 980 μM). Laser Irradiation was done 24 hours post injection of NETs or PBS. Irradiation parameters were: 808 nm; spot size = 9 mm; irradiation time = 10 min, $I_o = 680$ mW/cm^2. In panels (b) and (e), n = 4 mice for each administered agent. In panel (d), n = 5 images from different sections of same tumors for each administered agent (statistically significant difference at (**) $p <$ 0.01).

In response to laser irradiation at $I_o = 680$ mW/cm^2 in conjunction with NETs, we observed reductions in tumor volumes as early as two days post-laser irradiation (**Figure 4.6e**). By 10 days post-irradiation, tumor volumes were nearly zero. In contrast, laser

irradiation in the absence of NETs was associated with growths in tumor volumes, indicating the effectiveness of NETs in mediating photo-destruction of tumors.

Some important aspects of this study were the findings that: (1) NETs were localized to lysosomes as evidenced by LSCFM results (**Figure 4.3**); and (2) NETs mediated photo-activation of Caspase-3 in tumors (**Figure 4.6c, d**). These results indicate that lysosomal localization of NETs with subsequent laser irradiation, at the indicated parameters, can induce cellular apoptosis. Photo-induced damage to lysosomes membranes leads to release of cathepsin proteases and other hydrolytic enzymes into the cytosol[123] to activate apoptosis mediator proteins.[124] Pro-apoptotic mediators include a sub-group of B-cell lymphoma 2 (BCL-2) family of proteins.[125] Bid, is a member of the BCL-2 sub-group containing only the BH3 domain, which is cleaved by proteases to truncated Bid (tBid).[126] Upon translocation to the outer membranes of mitochondria, tBid can directly promote mitochondrial outer membrane permeabilization (MOMP).[127,128] or play a role in recruitment of cytosolic Bax, another member of the pro-apoptotic BCL-2 group, to mediate MOMP,[129,130] leading to release of pro-apoptotic proteins including cytochrome *c*.[131,132] The release of cytochrome *c* as a signal will finally activate the executors including Caspase-3 for cell death.[124] Therefore, our findings are consistent with photo-induced lysosomal damage as the basis to induce apoptosis. Nevertheless, based on the observed temperature increases (**Figure 4.6b**), photothermal effects could have also contributed to the destruction of cancer cells (**Figure 4.4**) and tumors (**Figure 4.6e**).

Various light-activated nanoparticle systems are under investigation in relation to cancer imaging and therapy. Based on material type, such systems can generally be

classified into semiconductors (e.g., quantum dots (QDs)), metallic (e.g., gold, silver), and organic particles (i.e., carbon nanomaterials such as graphene and fullerene).[133,134] There are certain attractive features with these types of materials such as photostability of QDs, tunable optical properties of QDs and gold nanomaterials, light-induced local surface plasmon resonance effects, and quantum confinement effects due to nanosize (<10nm) of carbon materials that result in their distinct optical properties. Limitations of these materials include cytotoxicity associated with certain constituents of QDs, potential oxidative stress and genotoxicity associated with gold nanoparticles,[135] safety concerns with carbon nanotubes,[136] and short vascular retention time of carbon nanomaterials due to their excretion through the kidneys, which stems from their small size (<10nm).

In comparison to these light-activated nanoparticle systems, the major key advantages of NETs stem from its constituent materials and composition that lead to the distinct properties and capabilities of these particles: (1) As constructs that can be engineered autologously (or from similar blood types), NETs are potentially non-immunogenic, non-toxic, and biocompatible. (2) CD47 is a key membrane glycoprotein expressed in erythrocytes,[137] which impedes phagocytosis. Our previous results[48] indicate that CD47 remains on the surface of NETs, suggesting that NETs may remain shielded from the immune system and have extended retention time within the vasculature; hence, providing their cargo (e.g., ICG) available for delivery to the tumor site over a longer time. Herein, as evidenced by NIR fluorescence imaging and *in vivo* laser irradiation studies, NETs remain available within tumors at 24 hours post intravenous injection. In comparison, the reported half-life of ICG encapsulated in poly(DL-lactic-co-glycolic acid)

or liposomal nanoparticles following intravenous injection are, respectively, on the order of approximately five minutes and less than a minute in blood.[29,138] (3) Fabrication of NETs is simple. Particles can be produced within about a day at room temperature and pressure without any complex chemical synthesis procedures, and use of specialized and expensive equipment.

Our results are consistent with the findings by Ren et al in which nanoparticles (≈ 150 nm diameter) comprised of an ICG-bound albumin and perfluorcarbon core encapsulated by an erythrocyte-derived membrane shell were used a photo-therapeutic agent.[139] These investigators also reported that both photothermal and photochemical effects (i.e., production of singlet oxygen) can serve as the basis for destruction of xenograft tumors in mice in response to 808 nm laser irradiation at I_o = 1 W/cm^2 for three minutes.

A synergistic effect of photothermal and photochemical mechanisms indicates that the photophysics of ICG allows for both vibrational relaxations from its excited state electronic states as well as intersystem crossing to a triplet state under the irradiation parameters investigated in this study to ultimately lead to photo-destruction of tumors. The photophysical properties of ICG can be exploited to endow NETs with capabilities for fluorescence imaging and therapeutic effects. In this context, NETs can serve as platforms for light-activated theranostics as applied to a variety of solid tumors. For example, a particularly important clinical application is in relation to ovarian cancer theranostics. Patients with ovarian cancer are most often diagnosed with late stage disease with metastasis to the peritoneum. One of the most important prognostic factors is the degree of

cytoreduction at surgery. However, small tumor nodules (< 1 mm) are difficult to detect by current pre-operative imaging methods, or visually during surgery. Furthermore, tumors may reside along critical structures to be removed without inducing significant morbidity. Surgical procedures such as diaphragm stripping, splenectomy, distal pancreatectomy, liver resection, or cholecystectomy may be required to remove such intraperitoneal tumors. NETs can potentially be used as light-activated theranostic nanoprobes during intraoperative procedures to enable visualization of small tumor nodules for surgical removal, or mediate photo-destruction of inoperable tumors.

Conclusion

We have demonstrated the photo-theranostic capabilities of NETs for fluorescence imaging and photo-destruction of cancer cells, and subcutaneous xenograft tumors in mice. NETs are internalized by cancer cells, and localized to the lysosomes. NETs remain available within tumors at 24 hours post intravenous injection, and mediate the destruction of cancer cells and xenograft tumors through synergistic photochemical and photothermal effects at the irradiation parameters investigated. Our results indicate that NETs are capable of mediating photo-induced tumor destruction initiated by their localization to lysosomes with subsequent activation of Caspase-3, and culminated in tumor apoptosis.

Chapter 5

Ovarian Tumor Imaging using Erythrocyte-Derived Fluorescent Nanoprobes and Structured Illumination

Abstract

Fluorescent nanoparticles activated by near-infrared excitation provide a potential platform for optical imaging of ovarian cancer. We have engineered nano-sized vesicles derived from erythrocytes that encapsulate the FDA-approved NIR fluorophore, ICG. We refer to these constructs as NETs. Herein, we present the first demonstration of the use of NETs in conjunction with structured illumination to fluorescently image ovarian tumors intraperitoneally implanted in mice. Our results showed high accumulation of NETs within tumors 24 hours post-intraperitoneal injection. We demonstrate enhanced contrast for imaging with frequency modulations over conventional constant illumination. In addition, we show the ability to estimate the concentration of ICG delivered by NETs and compare those values to quantitative organ analysis. Our results suggest that NETs can be used in conjunction with structured illumination for potential tumor imaging applications.

Introduction

Ovarian cancer has the greatest mortality rate than all gynecological malignancies combined, accounting for approximately 14,000 deaths in the United States in 2018.[140,141] Patients with ovarian cancer are often diagnosed with the late stage of the disease, with only 19% diagnosed when the cancer is confined to the ovaries (stage I).[142] The 5-year survival rate is relatively high (≈ 92%) if diagnosed at stage I, but significantly drops to less than 30% if diagnosed at stage III-IV where the cancer metastasizes beyond the pelvic region.[142] One of the most important factors for improving survival rate is the success of cytoreductive surgery with complete resection of all visible cancer.[143–145] However, the current surgical standard is to remove tumor nodules larger than 1 cm, often resulting in partial resection. In addition, there may be undetectable small intraperitoneal tumor nodules (< 1 cm) and/or poor contrast between the tumor and healthy tissue which contribute to the difficulty of complete resection. Therefore, there is a clinical need for development of intraoperative imaging systems to guide the removal of all intraperitoneal ovarian tumors. Effectiveness of fluorescein isothiocyanate (FITC) as a visible fluorescent tracer has been demonstrated in intraoperative image-guided removal of ovarian tumors in women.[146]

Use of fluorescent agents activated within by NIR wavelengths in the spectral range of ≈ 700-1300 are particularly advantageous, allowing for optical imaging on the order of at least 1 cm depending on tissue optical properties.[147,148] Epithelial ovarian cancer accounts for nearly 90% of ovarian tumors.[149] Since the invasion depth of epithelial ovarian

cancer is in the range of ≈2-5 cm, NIR wavelengths offer sufficient penetration depth to image these tumors.[150]

To-date, ICG remains as the only FDA approved NIR dye for applications including assessment of cardiac and hepatic function, ophthalmic angiography, and blood flow evaluation.[7–9] More recently, ICG has been used during intraoperative imaging of liver and ovarian cancers to enhance tumor-tissue boundaries for more accurate resection.[151,152] However, one of the major drawbacks of ICG's is its short circulation half-life (≈ 3-5 min) and elimination through the hepatobiliary mechanism,[88,153] which limits it bioavailability for effective tumor visualization.

Various constructs (e.g. micelles, liposomes, synthetic polymers and silica) have been used to overcome these limitations by encapsulating ICG.[23,24,27,154,155] Due to their potential biocompatibility, erythrocytes, macrophages and lymphocytes or constructs derived from them have been receiving attention as delivery platforms.[32–34] Erythrocytes are particularly attractive due to "self-marker" membrane proteins that shield them from clearance by the mononuclear phagocytic system.[49] Therefore, constructs derived from erythrocytes may have extended circulation times to have their cargo (e.g, ICG) available for an intended application such as optical imaging of ovarian tumor nodules. We demonstrated the first engineering of nano-sized vesicles derived from erythrocytes containing ICG.[47] We refer to these particles as NIR erythrocyte-mimicking transducers (NETs), since once activated by NIR light they can transduce the energy to emit fluorescence, generate heat, or lead to formation of reactive oxygen species.[156] When

combined with appropriate imaging techniques, NETs can provide fluorescence detection of specific structures such as tumors.

A particular wide-field optical imaging method is based on SMI. SMI uses structured illumination patterns of varying spatial frequencies projected on the tissue, and measures the attenuated intensity of the spatial patterns returning from the illuminated object through wide-field detection of optical sensors on a pixel by pixel basis. SMI has been used to estimate the 2-D optical properties of tissues,[53,54] and quantify depth-resolved Protoporphyrin IX concentrations from preclinical glioma models using fluorescent imaging.[55,56] In addition, SMI has been used to enhance fluorescence imaging of subcutaneous myeloma tumor boundaries imaging using Cy5.[157]

Herein, we present the first demonstration of using NETs in conjunction with SMI to image ovarian intraperitoneal tumors in mice. We first validated the ability to image tumor phantoms using SMI and NETs. Our *in vivo* results showed high accumulation of NETs within tumors. Through use of SMI, we were able to demonstrate enhanced contrast for NETs-mediated fluorescence imaging with frequency modulations over conventional non-modulated illumination. Lastly, we demonstrated wide-field estimation of ICG concentration delivered by NETs and compare those values to quantitative organ analysis.

Materials and Methods

Fabrication of NETs

Whole human blood (Innovative Research, Novi, MI) was centrifuged (5 minutes, 1,300xg, 4 °C) to isolate the erythrocytes. Plasma and buffy coat were discarded and the remaining

pellet containing erythrocytes was washed twice with 310 mOsm phosphate buffer saline (PBS) (referred to as the 1X solution) (pH ~ 8.0). The erythrocytes were then subjected to hypotonic treatment using 0.25X PBS (77.5 mOsm, pH ~ 8.0) and centrifuged (20,000xg, 15 minutes, 4 $^{\circ}$C). This process was repeated until all the hemoglobin was depleted, resulting in micron-sized EGs.

Nano-sized EGs were produced by sequential extrusion of the micron-sized EGs through 800, 400, and 200 nm polycarbonate porous membranes (Nuclepore Track-Etched Membranes, Whatman, Florham Park, New York) using an extruder (LIPEX Extruder, TRANSFERRA Nanosciences Inc, Burnaby, Canada) with the extrusion process repeated 10 times through each of the membranes with the indicated pore diameters. To concentrate the nano-sized EGs, 10 ml of suspension was centrifuged (99,000xg, 1 hour, 4 $^{\circ}$C), and the pellet was then re-suspended in 2 ml of 1X PBS.

To load ICG into nano-sized EGs, 2 ml of the concentrated nano-sized EGs suspension was incubated with 2 ml of 75 μM ICG dissolved in water and 2 ml of hypotonic buffer (Na_2HPO_4/ $Na_2H_2PO_4$, 140 mOsm, pH ~ 5.8), resulting in 25 μM concentration of ICG in the loading buffer. The suspension was incubated for five minutes at 4 °C in dark, centrifuged at 74,000xg for 30 minutes, and then washed two times using 1X PBS to remove any non-encapsulated ICG. The pellet containing ICG-encapsulated EGs (i.e., NETs) was removed and re-suspended in 0.5 ml of 1X PBS (4 $^{\circ}$C). To avoid saturation in the recordings the of absorption spectra, this solution of NETs was further diluted by a factor of 200 using 1X PBS. We then acquired the absorption and fluorescence spectra of the 1:200 diluted solution of NETs.

Characterization of NETs

The hydrodynamic diameters of NETs suspended in 1X PBS were measured by DLS (Zetasizer NanoZS90, Malvern Instruments Ltd, Malvern, United Kingdom). The absorption spectra of NETs (diluted 1:200) in 1X PBS was obtained using a UV-visible spectrophotometer (Cary 50 UV-Vis spectrophotometer, Agilent Technologies, Santa Clara, CA) with optical path length of 1 cm. The fluorescence emission spectra of NETs (diluted 1:200) was acquired in response to 710 ± 2.5 nm, and recorded using a fluorimeter (Fluorolog-3 spectrofluorometer, Edison, NJ). We obtained the normalized the fluorescence emission spectra [$\chi(\lambda)$] as:

$$\chi(\lambda) = \frac{F(\lambda)}{(1-10^{-A(\lambda_{ex})})} \tag{5.1}$$

where A and F are the wavelength (λ) dependent absorbance and intensity of the emitted fluorescence light, respectively, and λ_{ex} is the excitation wavelength.

We quantified the amount of ICG loaded in NETs by first acquiring the absorption spectra of ICG dissolved in the loading buffer solvent at concentrations in the range of 2-10 µM. The spectra were spectrally integrated in the range of 600-900 nm, and the resulting values (A_{int}) were plotted against ICG concentrations to obtain a calibration curve. We then used the supernatants collected after fabrication of NETs, calculated A_{int} in the same fashion, and used those A_{int} in conjunction with the calibration curve to determine the amount of ICG present in the supernatant ($m_{super} \approx 1.99$ µg). The initial amount of ICG in the loading buffer (113.25 µg) was subtracted $m_{super} \approx 1.99$ µg to estimate the amount of ICG loaded in NETs (111.26 µg).

SMI System

The SMI imaging system consisted of a digital micromirror device (DMD) chip projector equipped with a broadband high-pressure mercury (HPM) lamp (Dell MP2400, Round Rock, TX) (**Figure 5.1**). Illumination light was optically filtered to deliver excitation in the range of 710 ± 25 nm. An electron multiplier gained charge coupled device camera (Quant EM-CCD, C9100-14 Hamamatsu, Shizuoka-ken, Japan) equipped with an 18-55 mm focal length lens (Nikon AF-S DX NIKKOR 18-55mm, Tokyo, Japan), and bandpass or longpass filters was used to collect reflectance (720 ± 5 nm) or fluorescence emission (> 785 nm), respectively. Exposure times of the camera were set to 50 ms and 2 s for reflectance and fluorescence imaging, respectively.

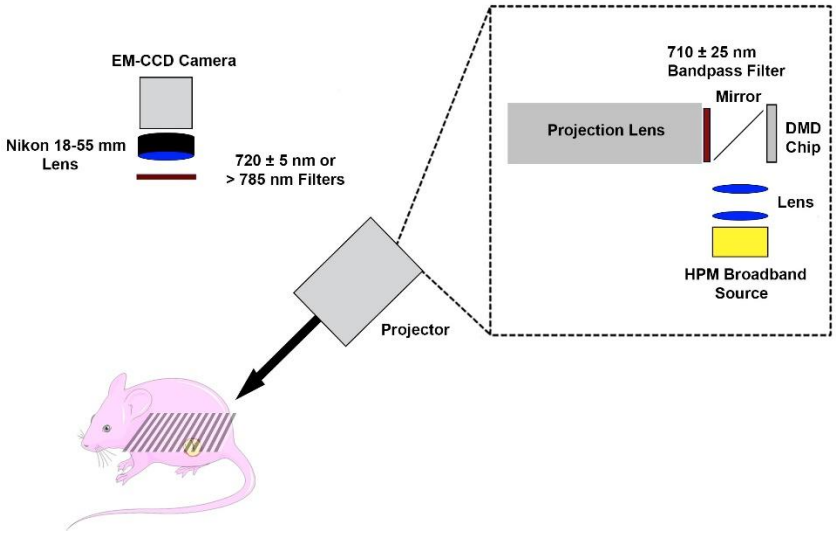

Figure 5.1 Reflectance and fluorescence spatial frequency imaging system.

We created patterned grayscale sinusoidal illumination with the spatial intensity pattern (*S*):

$$S = \frac{S_o[1+\cos(2\pi f_x x+\theta)]}{2}, \tag{5.2}$$

where S_o, f_x and θ are the illumination source intensity, spatial modulation frequency, and spatial phase offset, respectively. We used uniformly spaced values of f_x ranging between 0-0.50 mm^{-1} and θ = 0, 120 and 240°. For each f_x, we averaged three images at a given phase, and obtained the amplitude envelope (M_{AC}) by using a three-point amplitude demodulation method:[158]

$$M_{AC}(x,y) = \frac{\sqrt{2\{[I_1(x,y) - I_2(x,y)]^2 + [I_2(x,y) - I_3(x,y)]^2 + [I_3(x,y) - I_1(x,y)]^2\}}}{3} \quad (5.3)$$

where I_1, I_2 and I_3 represent the average intensity values of three images for a pixel in a given x and y position and a particular phase. We averaged three images to determine the amplitude of the DC (f_x = 0 mm^{-1}) component:

$$M_{DC}(x,y) = \frac{I_1(x,y) + I_2(x,y) + I_3(x,y)}{3} \quad (5.4)$$

Optical Property Estimation using the Diffusion Equation

In order to estimate the optical properties on a pixel by pixel basis the light diffusion equation was used. The time independent form of the light diffusion equation in a turbid medium is:

$$\frac{d^2}{dz^2}\varphi - \mu_{eff}{}^2\varphi = -q \quad (5.5)$$

where φ is the fluence rate ($W \cdot mm^{-2}$), z is depth, $\mu_{eff} = (3\,\mu_a\,\mu_{tr})^{1/2}$ (mm^{-1}) is the effective attenuation coefficient, $\mu_{tr} = (\mu_a + \mu_s')$ (mm^{-1}) is the transport coefficient, and q is the irradiance delivered by the source to the surface. Other parameters are defined as μ_a (mm^{-}

[1]) the absorption coefficient, μ_s (mm^{-1}) the scattering coefficient, g the mean cosine of the scattering function, and $\mu_s' = \mu_s(1-g)$ (mm^{-1}) the reduced scattering coefficient.

In response to the normal incident light modulated at a given k_x (mm^{-1}) ($k_x=2\pi f_x$) in the lateral direction on the surface, and having phase (θ):

$$q = q_o(z)\cos(k_x x + \theta) \tag{5.6}$$

the resulting fluence rate within the tissue will be

$$\varphi = \varphi_o(z)\cos(k_x x + \theta) \tag{5.7}$$

where $q_o = 3\,\mu_s'\,\mu_{tr}\,P_o \exp(-\mu_{tr} z)$, P_0 is the irradiance delivered by the source, and k_x is related to the spatial frequencies by $f_x = k_x/2\pi$. Inserting **equations 5.6** and **5.7** into **equation 5.5**, we form the 1D second-order Helmholtz equation for fluence rate as a function of depth:[53]

$$\frac{d^2}{dz^2}\varphi_o - \mu_{eff}'^{\,2}\varphi_o = -q_o \tag{5.8}$$

where

$$\mu_{eff}' = (\mu_{eff}^{\,2} + k_x^{\,2})^{1/2} = \frac{1}{\delta_{eff}'} \tag{5.9}$$

and δ'_{eff} is the effective penetration depth. The one-dimensional solution to **equation 5.8**, φ_o as a function of depth (z) is:

$$\varphi_o(z) = \frac{3P_o a'}{(\mu_{eff}'^{\,2}/\mu_{tr}^{\,2} - 1)}\exp(-\mu_{tr} z) + C\exp(-\mu_{eff}' z) \tag{5.10}$$

where $a' = \mu_s' / \mu_{tr}$ is the reduced albedo and C is a constant defined as:[159]

$$C = \frac{-3P_o a'(1+3A)}{(\mu_{eff}'^{\,2} / \mu_{tr}^{\,2} - 1)(\mu_{eff}' / \mu_{tr} + 3A)} \tag{5.11}$$

In **equation 5.11**, A is a proportionality constant related to the effective reflection coefficient R_{eff}:[159]

$$A = \frac{1 - R_{eff}}{2(1+R_{eff})};\ R_{eff} \approx 0.0636n + 0.668 + \frac{0.710}{n} - \frac{1.440}{n^2} \tag{5.12}$$

where n is the refractive index. We calculated normalized fluence ($\varphi_{o,norm}$) as a function of depth by dividing all $\varphi_o(z)$ values by $\varphi_o(z = 0)$ for each spatial frequency. Finally, the diffuse reflectance (R_d) is defined as:

$$R_d(f_x, \mu_a, \mu_s') = -\frac{A\varphi\big|_{z\to 0^+}}{P_o} = \frac{3Aa'}{(\mu_{eff}' / \mu_{tr} + 1)(\mu_{eff}' / \mu_{tr} + 3A)} \tag{5.13}$$

Using **equation 5.13**, we created a 2D map of R_d (f_x=0 mm^{-1}) (i.e., R_d in response to non-modulated illumination) vs R_d (f_x=0.5 mm^{-1}) for various values μ_a and μ_s' ranging between 0-3.00 mm^{-1} and incremented by 0.01 mm^{-1}. This 2D map can subsequently be used to determine the values of μ_a and μ_s' from the measurements of R_d for a given sample. Second, $M_{DC,ref}$ (f_x = 0 mm^{-1}) and $M_{AC,ref}$ (f_x = 0.50 mm^{-1}) were measured using a reference sample with known optical properties (μ_a = 0 mm^{-1} and μ_s' = 1.0 mm^{-1}) and R_d for the reference sample ($R_{d,ref}$) was calculated for f_x (0 and 0.50 mm^{-1}), μ_a = 0 mm^{-1} and μ_s' = 1 mm^{-1}. Third, a new measurement $M_{DC,sample}/M_{AC,sample}$, $M_{DC,ref}/M_{AC,ref}$, and $R_{d,ref}$ was used to solve $R_{d,sample}(x, y)$ (**equation 5.14**). Lastly, for both 0 and 0.50 mm^{-1}, $R_{d,sample}(x, y)$ and R_d from look up tables were then both used to determine μ_a and μ_s' using least squares minimization.[53] These results were then used to calculate φ_o and ultimately $\varphi_{o,norm.}$

$$R_{d,sample}(x, y, f_x) = \frac{M_{\mathrm{AC,sample}}(x, y, f_x)}{M_{\mathrm{AC},ref}(x, y, f_x)} R_{d,ref}(f_x) \quad (5.14)$$

Fabrication of Tumor Phantoms Containing NETs

Cylindrical gelatin phantoms were fabricated to represent a tumor mass containing NETs. Gelatin powder (Sigma Aldrich, St. Louis, MO, USA) at 10% concentration by mass dissolved in PBS was added to heated 1X PBS until dissolved. Once the gelatin solution cooled, intralipid was added as the scattering agent in the tumor phantom so $\mu_s' = 1\ \mathrm{mm}^{-1}$ at 710 nm. NETs were added to the tumor phantom at a concentration of 0.5% by volume. Phantoms were then refrigerated for 12 hours to solidify. On following day, we cut chicken breast samples into 2 x 2 x 2 cm cubes and used a punch biopsy to cut holes into these samples to implant the tumor phantom. We then used the punch biopsy to cut tumor phantoms into 4 mm diameters in the lateral direction and 1 mm in the axial direction and implanted them into the chicken breast. Chicken flaps were cut into 2 x 2 cm squares with thickness of 2.5 mm and placed over the tumors to mimic the presence of tissue that overlie tumors. These chicken breast tissue phantoms were then imaged by the SMI system in both reflectance and fluorescence modes. Using the reflectance measurements, μ_a and μ_s' were determined and averaged.

Animal Study

Female Nu/J mice (20~25 g; 6-8 weeks) were purchased from Jackson Laboratory (Bar Harbor, Maine) and utilized in this study under a protocol approved by the University of California, Riverside Institutional Animal Care and Use Committee (A-20170038). We

implanted ≈ 1×10^7 SKOV3 cancer cells by intraperitoneal (IP) injection while each animal was anesthetized by 2% isoflurane in oxygen. After four weeks, we administered 100 µl of NETs suspension in 1X PBS by IP injection while the animals were anesthetized 2% isoflurane in oxygen.

We estimated injected dosage of ICG delivered in NETs formulation as follows. Based on the amount of ICG loaded in NETs (111.26 µg), the effective concentration of ICG in NETs was 0.222 mg/ml. The effective concentration is an estimate of ICC concentration that would be dispersed in solution if NETs were disintegrated to release their ICG content. Given the injection volume of ≈ 0.1 ml into each mouse, and an average mouse weight of ≈ 20 g, dosage of ICG administered into an animal was ≈ 1.110 mg/kg. This injected dosage of ICG was lower than the lethal dosage in 50% of animals (LD_{50}) of ≈ 62 mg/kg in mice.[160]

After 24 hours, five mice were anesthetized with ketamine (80 mg/kg)/xylazine (10 mg/kg) and the whole body was imaged by the SMI system with eleven uniformly spaced f_x ranging between 0-0.50 mm^{-1} (imaging parameters stated in SMI system methods section). Mice were then euthanized with compressed CO_2 gas, and the abdomen was opened to expose the organs. We washed to abdominal cavity three times to remove NETs that were not uptaken by intraperitoneal tumors. The open abdomen was then imaged by the SMI system with eleven uniformly spaced f_x ranging between 0-0.50 mm^{-1}. For all representative images, fluorescence emission intensities were normalized by adjusting the minimum and maximum intensities.

Following euthanasia, liver, spleen, lung, intestine, heart, kidney, stomach and tumors with surrounding tissue were extracted and fluorescently imaged by the SMI system. Regions of interests (ROIs) were selected for each organ and the mean intensity ($\bar{I}$) was calculated as:

$$\bar{I} = \frac{\sum_{j=1}^{m} I_j}{m} \tag{5.15}$$

where m is the total number of pixels in the ROI and I_j is the pixel intensity at the jth pixel of a given image.

We subsequently used the estimated $\bar{I}$ values to compute the tumor to organ image contrast ($C_{Tumor\text{-}Organ}$):

$$C_{Tumor-Organ} = \frac{\bar{I}_T - \bar{I}_O}{\bar{I}_O} \tag{5.16}$$

where $\bar{I}_T$ and $\bar{I}_O$ represent the $\bar{I}$ for the tumor and each organ (liver, spleen, lung, intestine, heart, kidney) calculated independently and SD_O represents the standard deviation (SD) of $\bar{I}_O$.

Calculation of ICG Concentration using Imaging and Reference Phantoms

Liquid reference phantoms were fabricated to create a calibration of fluorescence intensity and ICG concentration. Intralipid (Sigma Aldrich, St. Louis, MO, USA) was added to 1X PBS so that $\mu_s' = 1\ mm^{-1}$ at 710 nm. This was estimated by creating a linear fit of previously measured μ_s' with intralipid concentration.[161] ICG concentrations were added so that the final concentrations were 0.025, 0.050, 0.075 and 0.100 μM. The

phantoms were fluorescently imaged with the SMI system with f_x = 0 mm^{-1} and average fluorescent intensities were calculated for each phantom. The resulting average fluorescent intensities were plotted against ICG concentrations to obtain a calibration curve (R^2 = 0.998). The animal images and $\bar{I}$ values were used with the calibration curve to estimate the ICG concentration within the animal and organs.

Quantitative Organ Analysis

Extracted organs were then grinded using a tissue grinder (Omni International, Inc., Kennesaw, GA, USA), and then incubated in 4 ml of sodium dodecyl sulfate (SDS, Sigma Aldrich, St. Louis, MO, USA) solution (5% w/v in water) for one hour to lyse the cells causing the release of ICG. Lysed organs in the SDS solution were centrifuged at 16,000g for 45 minutes at 4°C. The supernatants of the homogenized organs were collected, and the corresponding fluorescence emission spectra in response to 720 ± 2.5 nm excitation wavelength were recorded using the fluorimeter. ICG concentration in each organ was estimated by comparing the integrated fluorescence emission signal over the 735-900 nm spectral band with a calibration curve that related the integrated fluorescence emission over the same wavelength range to various concentrations of ICG in SDS solution.

Results and Discussion

NETs Characterization

Illustrative hydrodynamic diameter distribution, absorption, and fluorescence spectra of NETs fabricated using 25 μM ICG in the loading buffer are presented in **Figure 5.2**. The mean peak hydrodynamic diameter of NETs estimated by dynamic light scattering was ≈

101 nm (**Figure 5.2a**). These results are consistent with the measurements of the NETs diameter by transmission and electron scanning imaging.[47,48] Since the hydrodynamic diameters of NETs are < 200 nm, they are likely to be effective for extravasation into tumors through the enhanced permeability and retention effect, induced by the leaky tumor vasculature and impaired lymphatic drainage.[50,51]

Absorption at 280 nm originates from the presence of proteins on NETs. Absorption in the range of 600-900 nm with spectral peak and shoulder at 805 and 755 nm, respectively, correspond to the monomeric and aggregated forms of ICG.[47,162] Fluorescence spectrum in response to photo-excitation at 710 nm demonstrated an emission peak at 801 nm corresponding to the monomeric form of ICG.

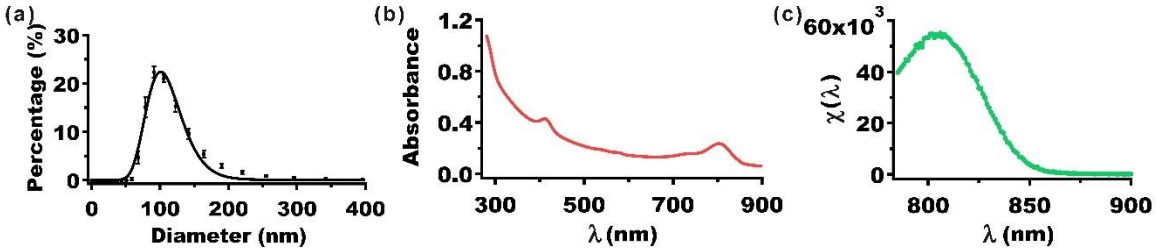

Figure 5.2 (a) Hydrodynamic diameter distribution of NETs as determined by DLS. Squares and error bars represent mean and SD of diameters, respectively (n = 8 measurements of the same sample). The estimated mean diameter as determined from log-normal fits (solid curves) was ≈ 101 nm. (b) Absorption spectrum of NETs. (c) Fluorescence spectrum of NETs in response to photo-excitation at 710 nm. The suspension of NETs in 1X PBS was diluted by factor of 200 for both absorption and $\chi(\lambda)$ measurements. ICG concentration used in the loading buffer to fabricate these NETs was 25 μM.

Phantom Study

Using reflectance SMI with f_x = 0 and 0.5 mm^{-1} of our chicken breast tissue phantom, μ_a and μ_s' were determined using least squares minimization of $R_d(x, y)$. We determined the mean ± SD of μ_a and μ_s' for our chicken breast tissue phantom to be 0.032 ± 0.008 and

0.1977 ± 0.035 mm^{-1}, respectively. Although μ_a and μ_s' values are within the range of previously reported values, μ_a values were slightly higher than our sample tested.[163] The difference in μ_a values may be due to slight variation in the optical properties of the chicken breast or an over estimation of μ_a due to minimal absorption.[53] There was little to no increase in μ_a due to the low concentration (0.5%) of NETs in the simulated tumor. Using the optical properties of the phantom and **equations 5.7** and **5.10**, we calculated $\varphi_{o,norm}$ for f_x = 0, 0.05, 0.10, 0.20 and 0.4 mm^{-1} as a function of depth and lateral location (**Figure 5.3a-e**).

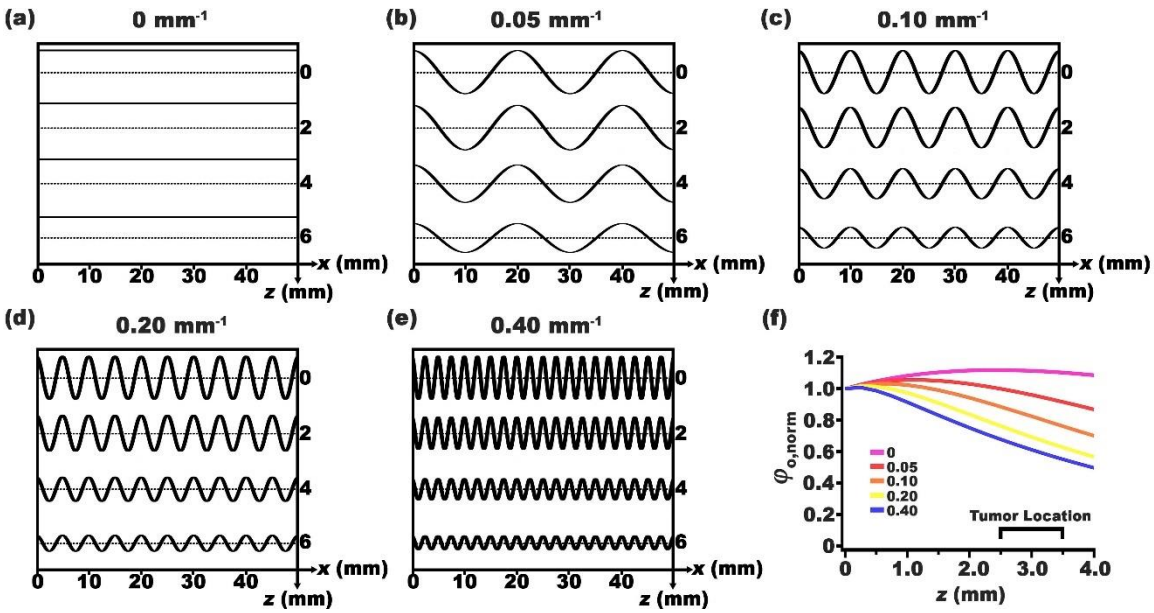

Figure 5.3 Normalized fluence profiles as a function of depth and lateral location for mean optical properties of the chicken breast phantom (μ_a = 0.028 mm^{-1}, μ_s' = 0.179 mm^{-1}) and spatial frequencies of (a) 0, (b) 0.05, (c) 0.10, (d) 0.20 and (e) 0.40 mm^{-1}. (f) Normalized fluence profiles as a function of depth for greatest intensity of each spatial frequency.

As f_x increased, $\varphi_{o,norm}$ decreased more rapidly for deeper depths. We present a summary for each $\varphi_{o,norm}$ as a function of depth for the maximum intensity for each f_x (**Figure 5.3f**). Within the tumor phantom location, $\varphi_{o,norm}$ decreased as the spatial frequency increased.

However, with $f_x > 0.30$ mm^{-1} there was little variation in $\varphi_{o,norm}$. For example, there was less than a 5% decrease in $\varphi_{o,norm}$ as f_x increased from 0.30 to 0.50 mm^{-1}. Due to scattering, the tissue acts as a low pass filter, attenuating $\varphi_{o,norm}$ at greater depths for high spatial frequencies.[164] This low pass filtering property can be attributed to limiting the number of longer path length excitation photons which attenuates the excitation at deeper depths.[54]

We present demodulated SMI fluorescent images of tumor phantom in response to illumination at f_x = 0, 0.05, 0.10, 0.20 and 0.40 mm^{-1} (**Figure 5.4a**). The intensity of the images decreases with increased spatial frequency indicating low-pass spatial filtering properties of tissue. At f_x = 0 mm^{-1}, there was increased intensity in the phantom surrounding the simulated tumor from longer path length photons. Due to higher fluence values associated with the use of f_x = 0.05-0.20 mm^{-1}, tumor phantoms at depth of 2.5 mm could be more easily distinguished. For $f_x > 0.20$ mm^{-1}, tumor fluorescence dropped off rapidly similarly to the fluence plot. This suggests that SMI allows for enhanced contrast with selection of appropriate spatial frequencies. We quantified the contrast for the tumor to chicken phantom ratio ($C_{Tumor\text{-}Phantom}$) where the SD represents the standard deviation of the contrast derived from pixel intensity SD from the tumor and chicken phantom. As f_x increased, contrast increased with maximal contrast at f_x = 0.10 mm^{-1}. The contrast of f_x = 0.10 mm^{-1} had ≈ 10-fold increase when compared to f_x = 0 mm^{-1}, which can be attributed to limitation of longer path photons. Whereas the decrease in contrast from f_x = 0.10 mm^{-1} to f_x = 0.40 mm^{-1} is due to lower intensity of the tumor within the phantom. Although for this tumor phantom the optimal contrast was with f_x = 0.10 mm^{-1}, the f_x to promote optimal

contrast may be different depending on the depth of tumor and optical properties of the tissue and tumor.

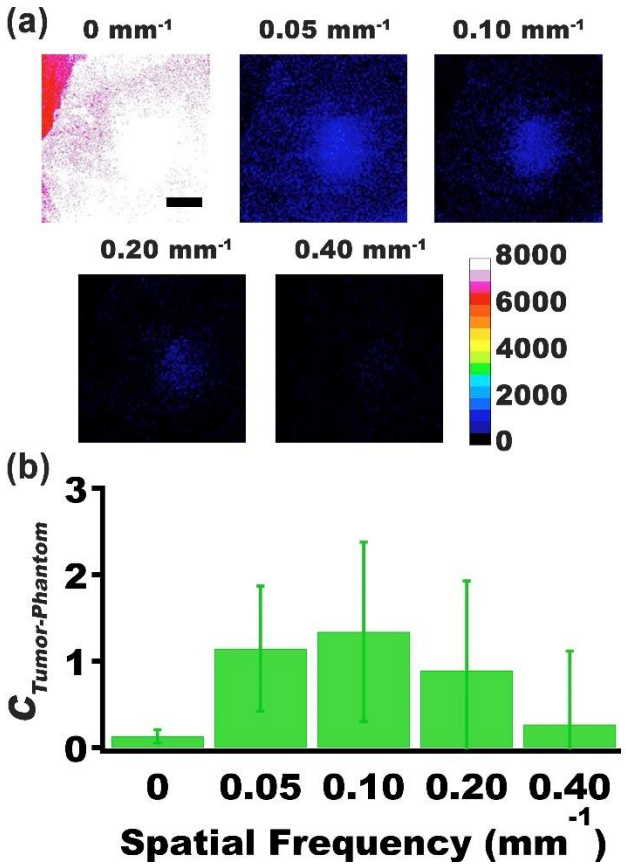

Figure 5.4 (a) Fluorescence intensity map of a 4 mm diameter tumor phantom at depth of 2.5 mm below the surface in response to illumination at spatial modulation frequencies of 0, 0.05, 0.10, 0.20 and 0.40 mm^{-1}. Concentration of NETs within the tumor phantom was 0.5%. Scale bar at the right corresponds to the intensity of the demodulated images. White scale bar on image corresponds to 5 mm. (b) Tumor-phantom contrast for spatial modulation frequencies of 0, 0.05, 0.10, 0.20 and 0.40 mm^{-1}.

Animal Study

Top panel of **Figure 5.5** shows representative color and fluorescent images for closed body mouse. There was highest intensity in the abdomen for both f_x = 0 and 0.20 mm^{-1}, suggesting that highest concentration of tumors resided in the abdomen. To investigate the

co-registration of color and NIR fluorescent images of NETs within tumors, we euthanized the mice, opened the body cavity and washed 3 times with 1X PBS to remove NETs that were not uptaken by any tumors or organs. We then fluorescently imaged the mouse open body using f_x = 0-0.50 mm^{-1}. Representative color and normalized fluorescence intensity images with f_x = 0 and 0.20 mm^{-1} are shown in middle panel of **Figure 5.5**. For all mice, there were tumor nodules identified throughout the abdominal and thoracic cavities, with highest number of tumor nodules in the abdominal cavity. In several mice, tumors could be identified near the lungs and heart using color and fluorescent images. This indicates that the tumors metastasized above the diaphragm and that NETs were able to reach the tumors through the circulatory system. Small molecules and nanoparticles can enter the circulatory system by the portal system veins through the visceral peritoneum, mesentery and omentum or by systemic circulation through the parietal peritoneum or lymphatics.[165–167] For washed open body mice without tumors and injected with NETs there was little signal from both abdominal and thoracic cavities suggesting that a majority of the signal was from NETs within tumors (**Figure 5.6**)

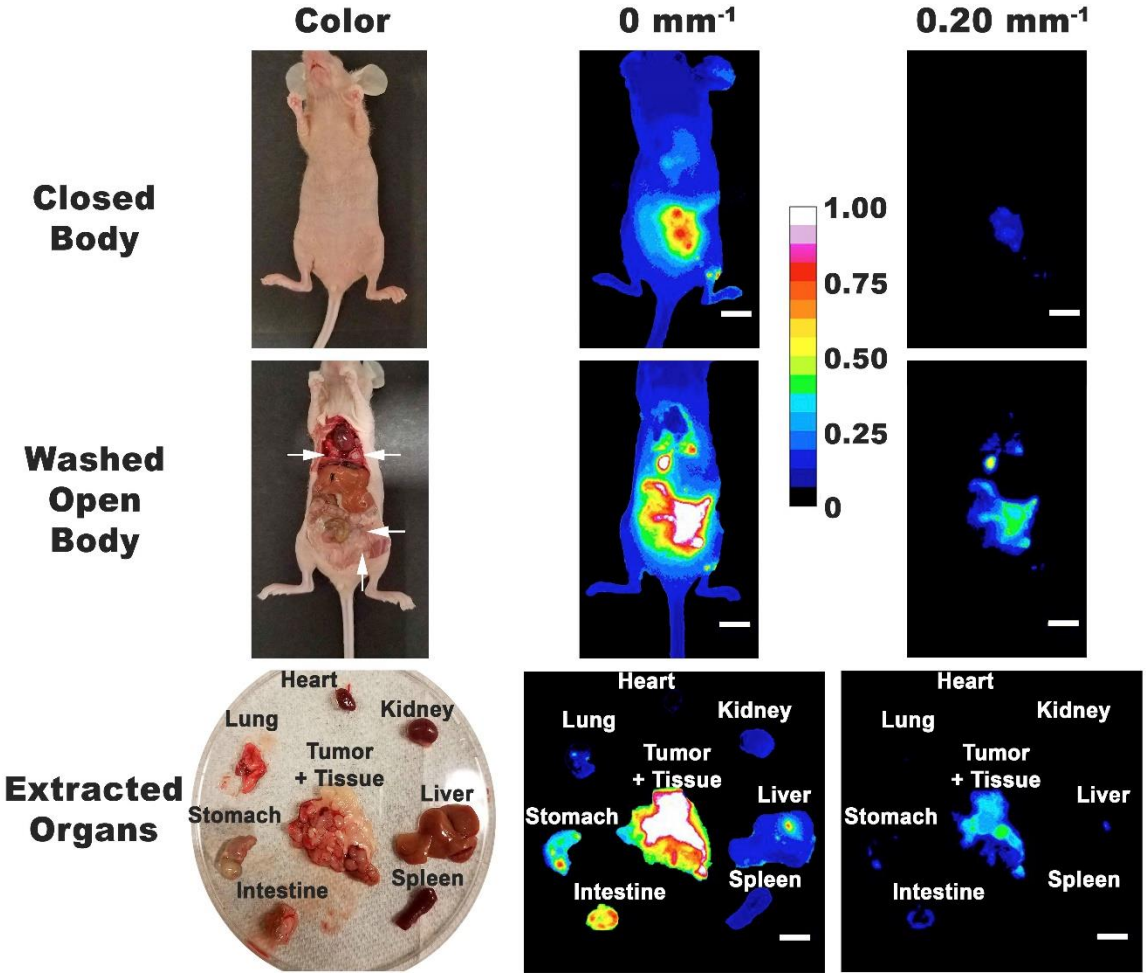

Figure 5.5 Representative color images and normalized fluorescent intensities for closed body (top panel, washed open body mouse (middle panel) and excised organs (bottom panel) with spatial frequencies of 0 and 0.2 mm^{-1}. Scale bar in the middle corresponds to normalized intensity of images for 0 or 0.2 mm^{-1}. Arrows indicate tumor locations. White scale bar on image corresponds to 10 mm.

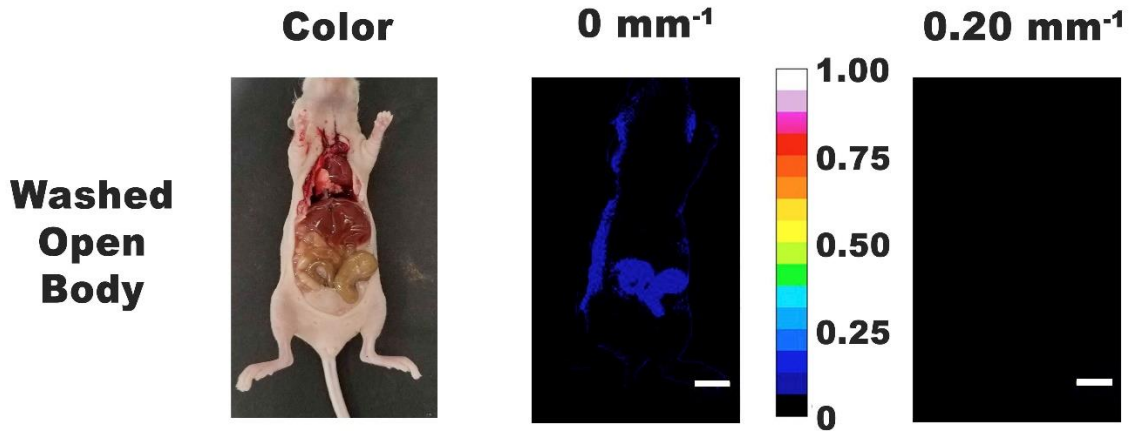

Figure 5.6 Representative color images and normalized fluorescent intensities for washed open body mouse for mice without tumors and with spatial frequencies of 0 and 0.2 mm^{-1}. Scale bar in the middle corresponds to normalized intensity of images for 0 or 0.2 mm^{-1}. White scale bar on image corresponds to 10 mm.

We removed the organs and fluorescently imaged them. Representative excised organs are shown in the bottom panel of **Figure 5.5**. Due to the difficulty in visually identifying the tumor margins from healthy tissue, we removed surrounding tissue around the tumor nodules. In addition to tumor masses growing independently, there were also tumor masses attached to the organs that were removed. Although we removed tumors that we could visually see, there were some organs were tumor cells may have extravasated into the other organs. Excised tumors had higher intensities when compared to the other organs for both f_x = 0 and 0.20 mm^{-1}. However, when visually examining images with f_x = 0.20 mm^{-1}, it was easier to identify the tumor from the rest of the organs. The fluorescence intensity from the stomach could be due to the presence of tumors within the organ, chlorophyll (alfalfa) in the rodent diet,[168] or from the NETs eliminated from the liver and excreted into the intestine via bile.[169]

To further explore the optimum f_x, we looked at the $C_{Tumor\text{-}Organ}$ for f_x = 0-0.50 mm^{-1} and tumor/organ ratios for extracted organs. We observed significantly higher $C_{Tumor\text{-}Intestine}$ for f_x = 0.10-0.05 mm^{-1} when compared to f_x = 0 mm^{-1} (**Figure 5.7a**). For example, with the highest significant frequency modulation of 0.20 mm^{-1}, there was ≈ 3-fold higher contrast than f_x = 0 mm^{-1}. This higher $C_{Tumor\text{-}Organ}$ can be attributed to reduced surface absorption due to the low sensitivity to absorption and high sensitivity to scattering for high frequency modulations.[170] Due to the significantly higher $C_{Tumor\text{-}Intestine}$ of 0.20 mm^{-1}, we chose to compare the tumor/organ contrast for all organs using f_x = 0 and 0.20 mm^{-1} (**Figure 5.7a,b**). For f_x = 0.20 mm^{-1}, there was greater $C_{Tumor\text{-}Organ}$ for all organs with significantly greater contrast for lung, intestine, heart and kidney (**Figure 5.7b**).

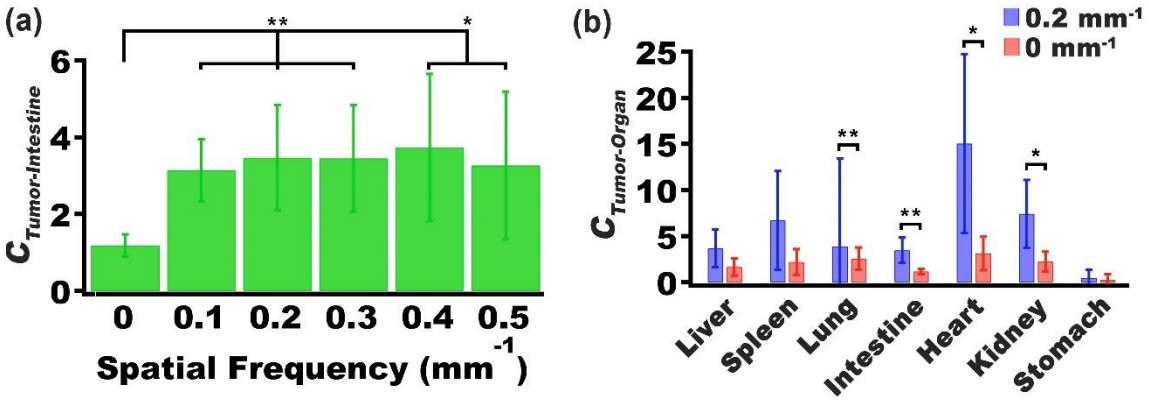

Figure 5.7 (a) Contrast mean and SD of tumor/intestine ratio for spatial frequencies of 0-0.5 mm^{-1}. (b) Contrast mean and SD of tumor against various organs for spatial frequencies of 0 and 0.2 mm^{-1}. In panels (a) and (b), statistically significant differences are indicated as *p < 0.05 and **p < 0.01.

Figure 5.8a shows representative images of the estimated ICG concentration in the mouse open body and *ex vivo* organs. The mean and SD estimated ICG concentrations for tumors were 0.098 ± 0.057 μM, which was significantly greater than the liver, spleen, lung, intestine, heart and kidney (**Figure 5.8b**). To determine the amount of ICG within the

organs, we digested the organs, measured the fluorescent of the lysate and compared against a calibration. The percent of initial dose (%ID) is shown in **Figure 5.8c**. Our quantitative organ analysis results compared had similar trend as the imaging concentration except for a slight increase for most of the organs except for the liver were there was a large increase. This increase is most likely due to the limitation in penetration depth due to the optical properties of the organ, which will underestimate thick organs with large values of μ_a.[171] Using the optical properties of rat liver (μ_a = 0.568 mm^{-1}, μ_s = 6.796 mm^{-1}, g = 0.935) and f_x = 0 mm^{-1}, we calculated δ'_{eff} to be ≈ 0.762 mm.[171] This value suggests there may deviation in estimated ICG concentration through imaging for high absorbing and thick organs. The %ID of the tumor was significantly greater than the spleen, lung, intestine, heart, and kidney with %ID mean and SD of 8.25 ± 3.30%. The %ID of the liver was not significantly different than the tumor with %ID mean and SD of 8.55 ± 1.63%.

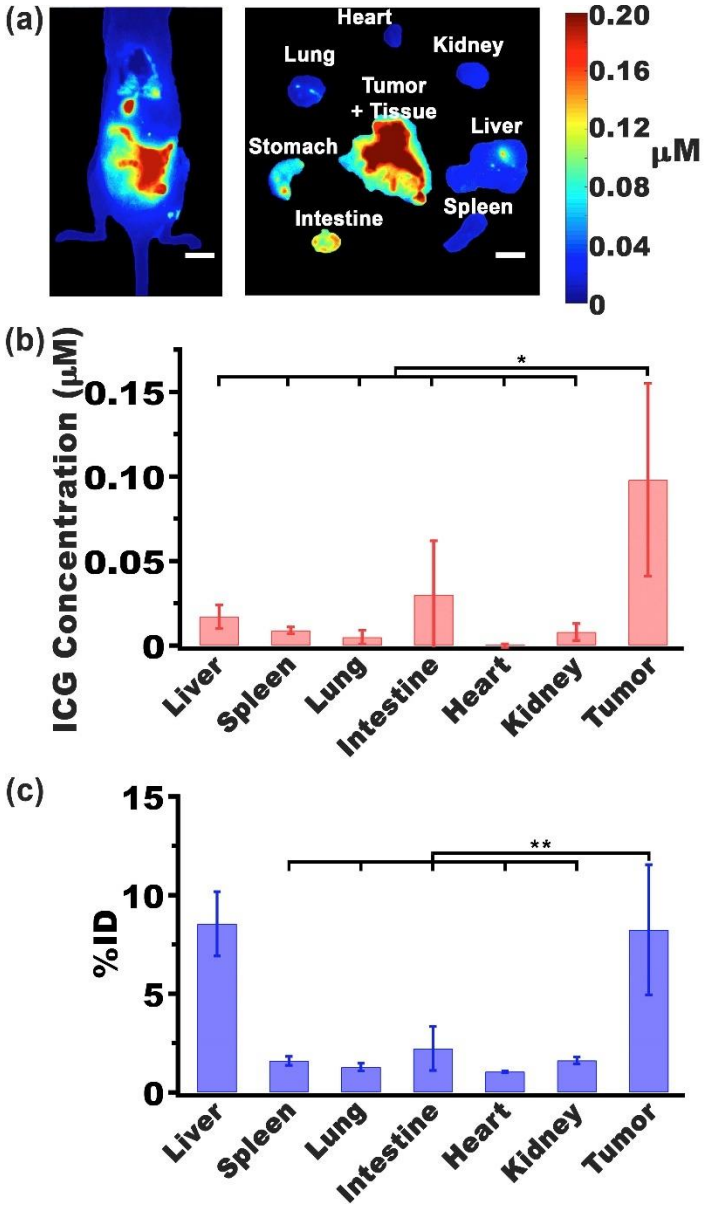

Figure 5.8 (a) Representative images of estimated ICG concentration for washed open body and excised organs. White scale bar on image corresponds to 10 mm. (b) Mean and SD of estimated ICG concentration determined by fluorescent images. (c) Mean and SD of estimated percent of ICG with respect to the initial dose injected using quantitative organ analysis. In panel (b) and (c), statistically significant differences are indicated as *$p < 0.05$ **$p < 0.01$.

When %ID was compared for mice with and without tumors and with NETs injected there was no significant difference for all organs with the exception of the lung (**Figure**

5.9). The liver is an import organ for elimination of nanoparticles with approximately 30-99% of administered nanoparticles ending up in this organ.[172] Liver sinusoidal endothelial cells form the lining of capillaries and create sinusoidal fenestrations with pore diameters of ≈ 175 nm.[172,173] If particles are smaller than the pore diameters sinusoidal containing Kupffer cell tissue macrophages can remove them from circulation.[174] In addition, particles can undergo endocytosis by hepatocytes, secreted into bile to the duodenum and eliminated from the body.[172] Nanoerythrosomes with diameters <100 nm have been reported to accumulate in both Kupffer cells and hepatocytes.[175]

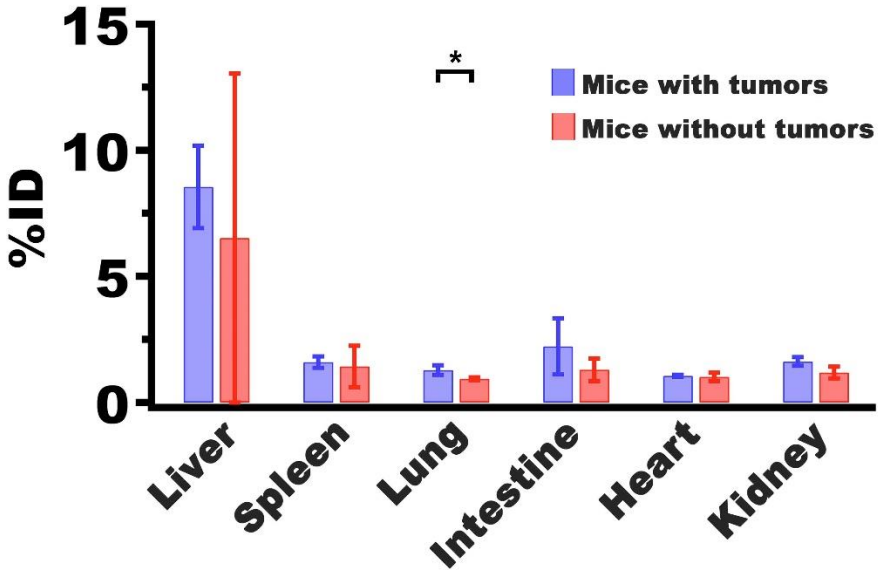

Figure 5.9 Mean and SD of estimated percent of ICG with respect to the initial dose injected using quantitative organ analysis for both mice with (n=5) and without tumors (n=3). Statistically significant differences are indicated as *p < 0.05 **p < 0.01.

Conclusion

In this study, we have presented the first demonstration of the use of NETs in conjunction with structured illumination to fluorescently detect ovarian tumor nodules. Our

results showed high accumulation of NETs within tumors 24 hours post-IP injection. We demonstrate enhanced contrast through the use of frequency modulations over conventional constant illumination. Lastly, our imaging results showed similar trends of concentration of ICG delivered by NETs when compare those values to quantitative organ analysis. These findings suggest that NETs can be used in conjunction with structured illumination for potential tumor imaging applications.

Conclusions

These theoretical and experimental studies have revealed that has erythrocyte derived particles doped with indocyanine green may be used for potential biomedical imaging and therapeutic applications of cancer and port wine stains. We reported, for the first time, the optical properties of NETs as a function of their diameters and the ICG concentration level used in fabricating them. Our results demonstrate that for a given NETs diameter, values of μ_a increased over the approximate spectral band of 630 – 860 nm with increasing ICG concentration. Micron-sized NETs produced the highest peak value of μ_a when using ICG concentrations of 10 and 20 μM as compared to nano-sized NETs. For these NETs, spectral profiles of μ_s' were minimally affected by ICG concentration used in fabricating the NETs. Micron-sized NETs had higher values of μ_s' as compared to nano-sized NETs. Knowledge of the NETs optical properties establishes a framework for development of mathematical models aimed at predicting the optical response of biological tissues containing NETs. Additionally, optical properties of NETs are important in guiding the selection of appropriate light dosimetry parameters for various light-based biomedical application of NETs.

Using theoretical models, we have demonstrated that NETs can be beneficial for NIR laser treatment of PWS. NETs can be fabricated with patient-specific optical properties to allow for a personalized treatment based on the size and depth of the blood vessels as well as the pigmentation of the individual's skin. The use of NIR lasers in combination with NETs addresses key challenges in vascular phototherapy by reducing epidermal damage and increasing penetration to deeper blood vessels.

We have demonstrated the photo-theranostic capabilities of NETs for fluorescence imaging and photo-destruction of cancer cells, and subcutaneous xenograft tumors in mice. NETs are internalized by cancer cells, and localized to the lysosomes. NETs remain available within tumors at 24 hours post intravenous injection, and mediate the destruction of cancer cells and xenograft tumors through synergistic photochemical and photothermal effects at the irradiation parameters investigated. Our results indicate that NETs are capable of mediating photo-induced tumor destruction initiated by their localization to lysosomes with subsequent activation of Caspase-3, and culminated in tumor apoptosis.

In this study, we have presented the first demonstration of the use of NETs in conjunction with structured illumination to fluorescently detect ovarian tumor nodules. Our results showed high accumulation of NETs within tumors 24 hours post-IP injection. We demonstrate enhanced contrast through the use of frequency modulations over conventional constant illumination. Lastly, our imaging results showed similar trends of concentration of ICG delivered by NETs when compare those values to quantitative organ analysis. These findings suggest that NETs can be used in conjunction with structured illumination for potential tumor imaging applications.

References

(1) Kim, H.; Chung, K.; Lee, S.; Kim, D. H.; Lee, H. Near-Infrared Light-Responsive Nanomaterials for Cancer Theranostics. *WIREs Nanomed Nanobiotechnol* **2016**, *8*, 23–45.

(2) Cheng, L.; Yuan, C.; Shen, S.; Yi, X.; Gong, H.; Yang, K.; Liu, Z. Bottom-Up Synthesis of Metal-Ion-Doped WS2 Nanoflakes for Cancer Theranostics. *ACS Nano* **2015**, *9*, 11090–11101.

(3) Shan, G.; Weissleder, R.; Hilderbrand, S. A. Upconverting Organic Dye Doped Core-Shell Nano-Composites for Dual-Modality NIR Imaging and Photo-Thermal Therapy. *Theranostics* **2013**, *3*, 267–274.

(4) Lee, M.-Y.; Lee, C.; Jung, H. S.; Jeon, M.; Kim, K. S.; Yun, S. H.; Kim, C.; Hahn, S. K. Biodegradable Photonic Melanoidin for Theranostic Applications. *ACS Nano* **2016**, *10*, 822–831.

(5) Lin, L.-S.; Yang, X.; Niu, G.; Song, J.; Yang, H.-H.; Chen, X. Dual-Enhanced Photothermal Conversion Properties of Reduced Graphene Oxide-Coated Gold Superparticles for Light-Triggered Acoustic and Thermal Theranostics. *Nanoscale* **2016**, *8*, 2116–2122.

(6) Win, K. Y.; Teng, C. P.; Ye, E.; Low, M.; Han, M. Y. Evaluation of Polymeric Nanoparticle Formulations by Effective Imaging and Quantitation of Cellular Uptake for Controlled Delivery of Doxorubicin. *Small* **2015**, *11*, 1197–1204.

(7) Frangioni, J. V. In Vivo Near-Infrared Fluorescence Imaging. *Curr. Opin. Chem. Biol.* **2003**, *7*, 626–634.

(8) Marshall, M. V.; Rasmussen, J. C.; Tan, I.-C.; Aldrich, M. B.; Adams, K. E.; Wang, X.; Fife, C. E.; Maus, E. A.; Smith, L. A.; Sevick-Muraca, E. M. Near-Infrared Fluorescence Imaging in Humans with Indocyanine Green: A Review and Update. *Open Surg Oncol J.* **2010**, *2*, 12–25.

(9) Hadjipanayis, C. G.; Jiang, H.; Roberts, D. W.; Yang, L. Current and Future Clinical Applications for Optical Imaging of Cancer: From Intraoperative Surgical Guidance to Cancer Screening. *Semin. Oncol.* **2011**, *38*, 109–118.

(10) Roessler, K.; Krawagna, M.; Dorfler, A.; Buchfelder, M.; Ganslandt, O. Essentials in Intraoperative Indocyanine Green Videoangiography Assessment for Intracranial Aneurysm Surgery: Conclusions from 295 Consecutively Clipped Aneurysms and Review of the Literature. *Neurosurg. Focus* **2014**, *36*, E7.

(11) Crane, L. M. A.; Themelis, G.; Arts, H. J. G.; Buddingh, K. T.; Brouwers, A. H.; Ntziachristos, V.; van Dam, G. M.; van der Zee, A. G. J. Intraoperative Near-Infrared Fluorescence Imaging for Sentinel Lymph Node Detection in Vulvar Cancer: First Clinical Results. *Gynecol. Oncol.* **2011**, *120*, 291–295.

(12) Hirche, C.; Murawa, D.; Mohr, Z.; Kneif, S.; Hunerbein, M. ICG Fluorescence-Guided Sentinel Node Biopsy for Axillary Nodal Staging in Breast Cancer. *Breast Cancer Res. Treat.* **2010**, *121*, 373–378.

(13) Ishikawa, K.; Yasuda, K.; Shiromizu, A.; Etoh, T.; Shiraishi, N.; Kitano, S. Laparoscopic Sentinel Node Navigation Achieved by Infrared Ray Electronic Endoscopy System in Patients with Gastric Cancer. *Surg. Endosc.* **2007**, *21*, 1131–

1134.
(14) Sevick-Muraca, E. M.; Sharma, R.; Rasmussen, J. C.; Marshall, M. V.; Wendt, J. A.; Pham, H. Q.; Bonefas, E.; Houston, J. P.; Sampath, L.; Adams, K. E.; *et al.* Imaging of Lymph Flow in Breast Cancer Patients after Microdose Administration of a Near-Infrared Fluorophore: Feasibility Study. *Radiology* **2008**, *246*, 734–741.
(15) van der Vorst, J. R.; Schaafsma, B. E.; Verbeek, F. P. R.; Swijnenburg, R. J.; Hutteman, M.; Liefers, G. J.; van de Velde, C. J. H.; Frangioni, J. V.; Vahrmeijer, A. L. Dose Optimization for Near-Infrared Fluorescence Sentinel Lymph Node Mapping in Patients with Melanoma. *Br. J. Dermatol.* **2013**, *168*, 93–98.
(16) Verbeek, F. P. R.; Troyan, S. L.; Mieog, J. S. D.; Liefers, G.-J.; Moffitt, L. A.; Rosenberg, M.; Hirshfield-Bartek, J.; Gioux, S.; van de Velde, C. J. H.; Vahrmeijer, A. L.; *et al.* Near-Infrared Fluorescence Sentinel Lymph Node Mapping in Breast Cancer: A Multicenter Experience. *Breast Cancer Res. Treat.* **2014**, *143*, 333–342.
(17) Zaidi, H. A.; Abla, A. A.; Nakaji, P.; Chowdhry, S. A.; Albuquerque, F. C.; Spetzler, R. F. Indocyanine Green Angiography in the Surgical Management of Cerebral Arteriovenous Malformations: Lessons Learned in 130 Consecutive Cases. *Neurosurgery* **2014**, *10 Suppl 2*, 246–251.
(18) Liggett, P. E.; Lavaque, A. J.; Chaudhry, N. A.; Jablon, E. P.; Quiroz-Mercado, H. Preliminary Results of Combined Simultaneous Transpupillary Thermotherapy and ICG-Based Photodynamic Therapy for Choroidal Melanoma. *Ophthalmic Surg. Lasers Imaging* **2005**, *36*, 463–470.
(19) Klein, A.; Baumler, H.; Buschmann, M.; Landthaler, M.; Babilas, P. A Randomized Controlled Trial to Optimize Indocyanine Green-Augmented Diode Laser Therapy of Capillary Malformations. *Lasers Surg. Med.* **2013**, *45*, 216–224.
(20) Klein, A.; Szeimies, R. M.; Baumler, W.; Zeman, F.; Schreml, S.; Hohenleutner, U.; Landthaler, M.; Koller, M.; Babilas, P. Indocyanine Green-Augmented Diode Laser Treatment of Port-Wine Stains: Clinical and Histological Evidence for a New Treatment Option from a Randomized Controlled Trial. *Br. J. Dermatol.* **2012**, *167*, 333–342.
(21) Kirchherr, A. K.; Briel, A.; Mäder, K. Stabilization of Indocyanine Green by Encapsulation within Micellar Systems. *Mol. Pharm.* **2009**, *6*, 480–491.
(22) Rodriguez, V. B., Henry, S. M., Hoffman, A. S. Encapsulation and Stabilization of Indocyanine Green within Poly(Styrene-Alt-Maleic Anhydride) Block-Poly(Styrene) Micelles for near-Infrared Imaging. *J. Biomed. Opt.* **2008**, *13*, 014025.
(23) Sharma, P.; Bengtsson, N. E.; Walter, G. A.; Sohn, H.-B.; Zhou, G.; Iwakuma, N.; Zeng, H.; Grobmyer, S. R.; Scott, E. W.; Moudgil, B. M. Gadolinium-Doped Silica Nanoparticles Encapsulating Indocyanine Green for near Infrared and Magnetic Resonance Imaging. *Small* **2012**, *8*, 2856–2868.
(24) Wu, L.; Fang, S.; Shi, S.; Deng, J.; Liu, B.; Cai, L. Hybrid Polypeptide Micelles Loading Indocyanine Green for Tumor Imaging and Photothermal Effect Study. *Biomacromolecules* **2013**, *14*, 3027–3033.
(25) Kraft, J. C.; Ho, R. J. Y. Interactions of Indocyanine Green and Lipid in Enhancing

Near-Infrared Fluorescence Properties: The Basis for near-Infrared Imaging in Vivo. *Biochemistry* **2014**, *53*, 1275–1283.
(26) Mordon, S.; Desmettre, T.; Devoisselle, J.-M.; Soulie, S. Thermal Damage Assessment of Blood Vessels in a Hamster Skin Flap Model by Fluorescence Measurement of a Liposome-Dye System. *Lasers Surg. Med.* **1997**, *20*, 131–141.
(27) Toyota, T.; Fujito, H.; Suganami, A.; Ouchi, T.; Ooishi, A.; Aoki, A.; Onoue, K.; Muraki, Y.; Madono, T.; Fujinami, M.; *et al.* Near-Infrared-Fluorescence Imaging of Lymph Nodes by Using Liposomally Formulated Indocyanine Green Derivatives. *Bioorg. Med. Chem.* **2014**, *22*, 721–727.
(28) Bahmani, B.; Gupta, S.; Upadhyayula, S.; Vullev, V. I.; Anvari, B. Effect of Polyethylene Glycol Coatings on Uptake of Indocyanine Green Loaded Nanocapsules by Human Spleen Macrophages in Vitro. *J. Biomed. Opt.* **2011**, *16*, 051303.
(29) Saxena, V.; Sadoqi, M.; Shao, J. Polymeric Nanoparticulate Delivery System for Indocyanine Green: Biodistribution in Healthy Mice. *Int. J. Pharm.* **2006**, *308*, 200–204.
(30) Yaseen, M. A.; Yu, J.; Wong, M. S.; Anvari, B. Stability Assessment of Indocyanine Green within Dextran-Coated Mesocapsules by Absorbance Spectroscopy. *J. Biomed. Opt.* **2007**, *12*, 064031.
(31) Zheng, X.; Zhou, F.; Wu, B.; Chen, W. R.; Xing, D. Enhanced Tumor Treatment Using Biofunctional Indocyanine Green-Containing Nanostructure by Intratumoral or Intravenous Injection. *Mol. Pharm.* **2012**, *9*, 514–522.
(32) Yoo, J.-W.; Irvine, D. J.; Discher, D. E.; Mitragotri, S. Bio-Inspired, Bioengineered and Biomimetic Drug Delivery Carriers. *Nat. Rev. Drug Discov.* **2011**, *10*, 521–535.
(33) Pierigè, F.; Serafini, S.; Rossi, L.; Magnani, M. Cell-Based Drug Delivery. *Adv. Drug Deliv. Rev.* **2008**, *60*, 286–295.
(34) Muzykantov, V. R. Drug Delivery by Red Blood Cells: Vascular Carriers Designed by Mother Nature. *Expert Opin. Drug Deliv.* **2010**, *7*, 403–427.
(35) Madsen, S. J.; Baek, S.-K.; Makkouk, A. R.; Krasieva, T.; Hirschberg, H. Macrophages as Cell-Based Delivery Systems for Nanoshells in Photothermal Therapy. *Ann. Biomed. Eng.* **2012**, *40*, 507–515.
(36) Kwon, Y. M.; Chung, H. S.; Moon, C.; Yockman, J.; Park, Y. J.; Gitlin, S. D.; David, A. E.; Yang, V. C. L-Asparaginase Encapsulated Intact Erythrocytes for Treatment of Acute Lymphoblastic Leukemia (ALL). *J. Control. Release* **2009**, *139*, 182–189.
(37) Antonelli, A.; Magnani, M. Red Blood Cells as Carriers of Iron Oxide-Based Contrast Agents for Diagnostic Applications. *J. Biomed. Nanotechnol.* **2014**, *10*, 1732–1750.
(38) Oldenborg, P. A. CD47: A Cell Surface Glycoprotein Which Regulates Multiple Functions of Hematopoietic Cells in Health and Disease. *ISRN Hematol* **2013**, *2013*, 614619.
(39) Rodriguez, P. L.; Harada, T.; Christian, D. A.; Pantano, D. A.; Tsai, R. K.; Discher, D. E. Minimal “Self” Peptides That Inhibit Phagocytic Clearance and

Enhance Delivery of Nanoparticles. *Science.* **2013**, *339*, 971–975.
(40) Brähler, M.; Georgieva, R.; Buske, N.; Müller, A.; Müller, S.; Pinkernelle, J.; Teichgräber, U.; Voigt, A.; Bäumler, H. Magnetite-Loaded Carrier Erythrocytes as Contrast Agents for Magnetic Resonance Imaging. *Nano Lett.* **2006**, *6*, 2505–2509.
(41) Antonelli, A.; Sfara, C.; Manuali, E.; Bruce, I. J.; Magnani, M. Encapsulation of Superparamagnetic Nanoparticles into Red Blood Cells as New Carriers of MRI Contrast Agents. *Nanomedicine* **2011**, *6*, 211–223.
(42) Chang, M.; Hsiao, J.-K.; Yao, M.; Chien, L.-Y.; Hsu, S.-C.; Ko, B.-S.; Chen, S.-T.; Liu, H.-M.; Chen, Y.-C.; Yang, C.-S.; *et al.* Homologous RBC-Derived Vesicles as Ultrasmall Carriers of Iron Oxide for Magnetic Resonance Imaging of Stem Cells. *Nanotechnology* **2010**, *21*, 235103.
(43) Ahn, S.; Jung, S. Y.; Seo, E.; Lee, S. J. Gold Nanoparticle-Incorporated Human Red Blood Cells (RBCs) for X-Ray Dynamic Imaging. *Biomaterials* **2011**, *32*, 7191–7199.
(44) Flower, R.; Peiretti, E.; Magnani, M.; Rossi, L.; Serafini, S.; Gryczynski, Z.; Gryczynski, I. Observation of Erythrocyte Dynamics in the Retinal Capillaries and Choriocapillaris Using ICG-Loaded Erythrocyte Ghost Cells. *Invest. Ophthalmol. Vis. Sci.* **2008**, *49*, 5510–5516.
(45) Milanick, M. A.; Ritter, S.; Meissner, K. Engineering Erythrocytes to Be Erythrosensors: First Steps. *Blood Cells Mol. Dis.* **2011**, *47*, 100–106.
(46) Ritter, S. C.; Milanick, M. A.; Meissner, K. E. Encapsulation of FITC to Monitor Extracellular PH: A Step towards the Development of Red Blood Cells as Circulating Blood Analyte Biosensors. *Biomed. Opt. Express* **2011**, *2*, 2012–2021.
(47) Bahmani, B.; Bacon, D.; Anvari, B. Erythrocyte-Derived Photo-Theranostic Agents: Hybrid Nano-Vesicles Containing Indocyanine Green for near Infrared Imaging and Therapeutic Applications. *Sci. Rep.* **2013**, *3*, 2180.
(48) Mac, J. T.; Nuñez, V.; Burns, J. M.; Guerrero, Y. A.; Vullev, V. I.; Anvari, B. Erythrocyte-Derived Nano-Probes Functionalized with Antibodies for Targeted near Infrared Fluorescence Imaging of Cancer Cells. *Biomed. Opt. Express* **2016**, *7*, 1311.
(49) Hu, C.-M. J.; Zhang, L.; Aryal, S.; Cheung, C.; Fang, R. H.; Zhang, L. Erythrocyte Membrane-Camouflaged Polymeric Nanoparticles as a Biomimetic Delivery Platform. *Proc. Natl. Acad. Sci. USA* **2011**, *108*, 10980–10985.
(50) Nakamura, H.; Jun, F.; Maeda, H. Development of Next-Generation Macromolecular Drugs Based on the EPR Effect: Challenges and Pitfalls. *Expert Opin. Drug Deliv.* **2015**, *12*, 53–64.
(51) Torchilin, V. Tumor Delivery of Macromolecular Drugs Based on the EPR Effect. *Adv. Drug Deliv. Rev.* **2011**, *63*, 131–135.
(52) Matsumura, Y.; Maeda, H. A New Concept for Macromolecular Therapeutics in Cnacer Chemotherapy: Mechanism of Tumoritropic Accumulatio of Proteins and the Antitumor Agents Smancs. *Cancer Res.* **1986**, *46*, 6387–6392.
(53) Cuccia, D. J.; Bevilacqua, F.; Durkin, A. J.; Ayers, F. R.; Tromberg, B. J. Quantitation and Mapping of Tissue Optical Properties Using Modulated Imaging. *J. Biomed. Opt.* **2009**, *14*, 024012.

(54) Cuccia, D. J.; Bevilacqua, F.; Durkin, A. J.; Tromberg, B. J. Modulated Imaging: Quantitative Analysis and Tomography of Turbid Media in the Spatial-Frequency Domain. *Opt. Lett.* **2005**, *30*, 1354–1356.
(55) Konecky, S. D.; Mazhar, A.; Cuccia, D.; Durkin, A. J.; Schotland, J. C.; Tromberg, B. J.; Owen, C. M.; Rice, T.; Valdés, P. a.; Kolste, K.; *et al.* Spatial Frequency Domain Tomography of Protoporphyrin IX Fluorescence in Preclinical Glioma Models. *J. Biomed. Opt.* **2012**, *17*, 056008.
(56) Sibai, M.; Fisher, C.; Veilleux, I.; Elliott, J. T.; Leblond, F.; Roberts, D. W.; Wilson, B. C. Preclinical Evaluation of Spatial Frequency Domain-Enabled Wide-Field Quantitative Imaging for Enhanced Glioma Resection. *J. Biomed. Opt.* **2017**, *22*, 076007.
(57) Clerc, S. G.; Thompson, T. E. A Possible Mechanism for Vesicle Formation by Extrusion. *Biophys. J.* **1994**, *67*, 475–476.
(58) Hunter, D. G.; Frisken, B. J. Effect of Extrusion Pressure and Lipid Properties on the Size and Polydispersity of Lipid Vesicles. *Biophys. J.* **1998**, *74*, 2996–3002.
(59) Lepherd, E. E. Obervations on Equine and Bovine Haematocrit Determinations. *Aust. Vet. J.* **1965**, *41*, 380–384.
(60) Prahl, S. A.; Gemert, M. J. C. . V.; Welch, A. J. Determining the Optical Properties of Turbid Media by Using the Adding-Doubling Method. *Appl. Opt.* **1993**, *32*, 559–568.
(61) Jacques, S. L. Optical Properties of Biological Tissues: A Review. *Phys. Med. Biol.* **2013**, *58*, R37–R61.
(62) Laser Microbeam and Medical Program (LAMMP). Virtual Photonics Technology Initiative http://www.virtualphotonics.org/.
(63) Majaron, B.; Milanič, M.; Premru, J. Monte Carlo Simulation of Radiation Transport in Human Skin with Rigorous Treatment of Curved Tissue Boundaries. *J. Biomed. Opt.* **2015**, *20*, 015002.
(64) Milanič, M.; Majaron, B. Three-Dimensional Monte Carlo Model of Pulsed-Laser Treatment of Cutaneous Vascular Lesions. *J. Biomed. Opt.* **2011**, *16*, 128002.
(65) Bosschaart, N.; Edelman, G. J.; Aalders, M. C. G.; Van Leeuwen, T. G.; Faber, D. J. A Literature Review and Novel Theoretical Approach on the Optical Properties of Whole Blood. *Lasers Med. Sci.* **2014**, *29*, 453–479.
(66) Adili, N.; Melizi, M. Preliminary Study of the Influence of Red Blood Cells Morphometry on the Species Determinism of Domestic Animals. *Vet. World* **2014**, *7*, 219–223.
(67) Nobbmann, U.; Morfesis, A. Light Scattering and Nanoparticles. *Mater. Today* **2009**, *12*, 52–54.
(68) Peer, D.; Karp, J. M.; Hong, S.; Farokhzad, O. C.; Margalit, R.; Langer, R. Nanocarriers as an Emerging Platform for Cancer Therapy. *Nat. Nanotechnol.* **2007**, *2*, 751–760.
(69) Jung, B.; Vullev, V. I.; Anvari, B. Revisiting Indocyanine Green: Effects of Serum and Physiological Temperature on Absorption and Fluorescence Characteristics. *IEEE J. Sel. Top. Quantum Electron.* **2014**, *20*, 149–157.
(70) Valdes-Aguiler, O.; Neckers, D. C. Aggregation Phenomena in Xanthene Dyes.

Accounts Chem. Res. **1989**, *22*, 171–177.
(71) Herz, A. H. Aggregation of Sensitizing Dyes in Solution and Their Adsorption onto Silver Halides. *Adv. Colloid Interface Sci.* **1977**, *8*, 237–298.
(72) Ogawa, M.; Kosaka, N.; Choyke, P. L.; Kobayashi, H. H-Type Dimer Formation of Fluorophores: A Mechanism for Activatable, in Vivo Optical Molecular Imaging. *ACS Chem. Biol.* **2009**, *4*, 535–546.
(73) Prahl, S. Optical Absorption of Hemoglobin http://omlc.org/spectra/hemoglobin/.
(74) Zonios, G.; Bykowski, J.; Kollias, N. Skin Melanin, Hemoglobin, and Light Scattering Properties Can Be Quantitatively Assessed in Vivo Using Diffuse Reflectance Spectroscopy. *J. Invest. Dermatol.* **2001**, *117*, 1452–1457.
(75) Prahl, S. Optical Absorption of Indocyanine Green (ICG) http://omlc.org/spectra/icg/.
(76) Yi, J.; Backman, V. Imaging a Full Set of Optical Scattering Properties of Biological Tissue by Inverse Spectroscopic Optical Coherence Tomography. *Opt. Lett.* **2012**, *37*, 4443–4445.
(77) Newman, C.; Jacques, S. L. Laser Penetration into Prostate for Various Wavelengths. *Lasers Surg. Med.* **1991**, *Suppl 3*, 75–76.
(78) Sandell, J. L.; Zhu, T. C. A Review of In-Vivo Optical Properties of Human Tissues and Its Impact on PDT. *J. Biophotonics* **2011**, *4*, 773–787.
(79) Anderson, R. R.; Beck, H.; Bruggemann, U.; Farinelli, W.; Jacques, S. L.; Parrish, J. a. Pulsed Photothermal Radiometry in Turbid Media: Internal Reflection of Backscattered Radiation Strongly Influences Optical Dosimetry. *Appl. Opt.* **1989**, *28*, 2256–2262.
(80) Kanada, K. N.; Merin, M. R.; Munden, A.; Friedlander, S. F. A Prospective Study of Cutaneous Findings in Newborns in the United States: Correlation with Race, Ethnicity, and Gestational Status Using Updated Classification and Nomenclature. *J. Pediatr.* **2012**, *161*, 240–245.
(81) Kautz, G.; Kautz, I.; Segal, J.; Zehren, S. Treatment of Resistant Port Wine Stains (PWS) with Pulsed Dye Laser and Non-Contact Vacuum: A Pilot Study. *Lasers Med. Sci.* **2010**, *25*, 525–529.
(82) Rajaratnam, R.; Laughlin, S. A.; Dudley, D. Pulsed Dye Laser Double-Pass Treatment of Patients with Resistant Capillary Malformations. *Lasers Med. Sci.* **2011**, *26*, 487–492.
(83) Jasim, Z. F.; Handley, J. M. Treatment of Pulsed Dye Laser-Resistant Port Wine Stain Birthmarks. *J. Am. Acad. Dermatol.* **2007**, *57*, 677–682.
(84) Greve, B.; Raulin, C. Prospective Study of Port Wine Stain Treatment with Dye Laser: Comparison of Two Wavelengths (585 Nm vs. 595 Nm) and Two Pulse Durations (0.5 Milliseconds vs. 20 Milliseconds). *Lasers Surg. Med.* **2004**, *34*, 168–173.
(85) Koster, P. H.; Bossuyt, P. M.; van der Horst, C. M.; Gijsbers, G. H.; Van Gemert, M. J. Assessment of Clinical Outcome after Flashlamp Pubmed Pulsed Dye Laser Treatment of Portwine Stains: A Comprehensive Questionnaire. *Plast. Reconstr. Surg.* **1998**, *102*, 42–48.
(86) Kelly, K. M.; Choi, B.; McFarlane, S.; Motosue, A.; Jung, B.; Khan, M. H.;

Ramirez-San-Juan, J. C.; Nelson, J. S. Description and Analysis of Treatments for Port-Wine Stain Birthmarks. *Arch. Facial Plast. Surg.* **2005**, *7*, 287–294.
(87) Montazerabadi, A. R.; Sazgarnia, A.; Bahreyni-Toosi, M. H.; Ahmadi, A.; Aledavood, A.; Reza, A.; Sazgarnia, A.; Bahreyni-Toosi, M. H.; Ahmadi, A.; Aledavood, A.; *et al.* The Effects of Combined Treatment with Ionizing Radiation and Indocyanine Green-Mediated Photodynamic Therapy on Breast Cancer Cells. *J. Photochem. Photobiol. B.* **2012**, *109*, 42–49.
(88) Desmettre, T.; Devoisselle, J. M.; Mordon, S. Fluorescence Properties and Metabolic Features of Indocyanine Green (ICG) as Related to Angiography. *Surv. Ophthalmol.* **2000**, *45*, 15–27.
(89) Kim, G.; Huang, S.-W.; Day, K. C.; O'Donnell, M.; Agayan, R. R.; Day, M. A.; Kopelman, R.; Ashkenazi, S. Indocyanine-Green-Embedded PEBBLEs as a Contrast Agent for Photoacoustic Imaging. *J. Biomed. Opt.* **2007**, *12*, 44020–44028.
(90) Burns, J. M.; Saager, R.; Majaron, B.; Jia, W.; Anvari, B. Optical Properties of Biomimetic Probes Engineered from Erythrocytes. *Nanotechnology* **2017**, *28*, 035101.
(91) Liu, G.; Jia, W.; Nelson, J. S.; Chen, Z.; Clinic, M. In Vivo, High-Resolution, Three-Dimensional Imaging of Port Wine Stain Microvasculature in Human Skin. *Lasers Surg. Med.* **2013**, *45*, 628–632.
(92) Jacques, S. L. Skin Optics http://omlc.ogi.edu/news/jan98/skinoptics.html.
(93) Lu, H.; Edwards, C.; Gaskell, S.; Pearse, A.; Marks, R. Melanin Content and Distribution in the Surface Corneocyte with Skin Phototypes. *Br. J. Dermatol.* **1996**, *135*, 263–267.
(94) Kienle, A.; Hibst, R. A New Optimal Wavelength for Treatment of Port Wine Stains? *Phys. Med. Biol.* **1995**, *40*, 1559–1576.
(95) Graaff, R.; Dassel, A. C. M.; Koelink, M. H.; de Mul, F. F. M.; Aarnoudse, J. G.; Zijlstra, W. G. Optical Properties of Human Dermis in Vitro and in Vivo. *Appl. Opt.* **1993**, *32*, 435–447.
(96) Nelson, J. S.; Milner, T. E.; Anvari, B.; Tanenbaum, B. S.; Kimel, S.; Svaasand, L. O.; Jacques, S. L. Dynamic Epidermal Cooling during Pulsed Laser Treatment of Port-Wine Stain. A New Methodology with Preliminary Clinical Evaluation. *Arch. Dermatol.* **1995**, *131*, 695–700.
(97) Pikkula, B. M.; Tunnell, J. W.; Chang, D. W.; Anvari, B. Effects of Droplet Velocity, Diameter, and Film Height on Heat Removal during Cryogen Spray Cooling. *Ann. Biomed. Eng.* **2004**, *32*, 1131–1140.
(98) Dai, T.; Pikkula, B. M.; Wang, L. V; Anvari, B. Comparison of Human Skin Opto-Thermal Response to near-Infrared and Visible Laser Irradiations: A Theoretical Investigation. *Phys. Med. Biol.* **2004**, *49*, 4861–4877.
(99) Tunnell, J. W.; Wang, L. V; Anvari, B. Optimum Pulse Duration and Radiant Exposure for Vascular Laser Therapy of Dark Port-Wine Skin: A Theoretical Study. *Appl. Opt.* **2003**, *42*, 1367–1378.
(100) Aguilar, G.; Majaron, B.; Pope, K.; Svaasand, L. O.; Lavernia, E. J.; Nelson, J. S. Influence of Nozzle-to-Skin Distance in Cryogen Spray Cooling for Dermatologic

Laser Surgery. *Lasers Surg. Med.* **2001**, *28*, 113–120.
(101) Majaron, B.; Svaasand, L. O.; Aguilar, G.; Nelson, J. S. Intermittent Cryogen Spray Cooling for Optimal Heat Extraction during Dermatologic Laser Treatment. *Phys. Med. Biol.* **2002**, *47*, 3275–3288.
(102) Weaver, J. A.; Stoll, A. M. Mathematical Model of Skin Exposed to Thermal Radiation. *Aerosp. Med.* **1969**, *40*, 24–30.
(103) Lepock, J. R.; Frey, H. E.; Bayne, H.; Markus, J. Relationship of Hyperthermia-Induced Hemolysis of Human Erythrocytes to the Thermal Denaturation of Membrane Proteins. *Biochim. Biophys. Acta* **1989**, *980*, 191–201.
(104) Izikson, L.; Anderson, R. R. Treatment Endpoints for Resistant Port Wine Stains with a 755 Nm Laser. *J. Cosmet. Laser Ther.* **2009**, *11*, 52–55.
(105) Lister, T.; Wright, P. A.; Chappell, P. H. A New Monte Carlo Program for Simulating Light Transport through Port Wine Stain Skin. *Lasers Surg. Med.* **2014**, *29*, 1017–1028.
(106) Pfefer, T. J.; Barton, J. K.; Smithies, D. J.; Milner, T. E.; Nelson, J. S.; Gemert, M. J. C. Van; Welch, A. J. Modeling Laser Treatment of Port Wine Stains With a Computer-Reconstructed Biopsy. *Lasers Med. Sci.* **1999**, *24*, 151–166.
(107) Piao, J. G.; Wang, L.; Gao, F.; You, Y. Z.; Xiong, Y.; Yang, L. Erythrocyte Membrane Is an Alternative Coating to Polyethylene Glycol for Prolonging the Circulation Lifetime of Gold Nanocages for Photothermal Therapy. *ACS Nano* **2014**, *8*, 10414–10425.
(108) Burger, P.; Hilarius-stokman, P.; Korte, D. De; Berg, T. K. Van Den; Bruggen, R. Van. CD47 Functions as a Molecular Switch for Erythrocyte Phagocytosis. *Blood* **2012**, *119*, 5512–5521.
(109) Rao, L.; Meng, Q. F.; Bu, L. L.; Cai, B.; Huang, Q.; Sun, Z. J.; Zhang, W. F.; Li, A.; Guo, S. S.; Liu, W.; *et al.* Erythrocyte Membrane-Coated Upconversion Nanoparticles with Minimal Protein Adsorption for Enhanced Tumor Imaging. *ACS Appl. Mater. Interfaces* **2017**, *9*, 2159–2168.
(110) Peng, J.; Yang, Q.; Li, W.; Tan, L.; Xiao, Y.; Chen, L.; Hao, Y.; Qian, Z. Erythrocyte-Membrane-Coated Prussian Blue/Manganese Dioxide Nanoparticles as H2O2-Responsive Oxygen Generators to Enhance Cancer Chemotherapy/Photothermal Therapy. *ACS Appl. Mater. Interfaces* **2017**, *9*, 44410–44422.
(111) Spiller, W.; Kliesch, H.; Wöhrle, D.; Hackbarth, S.; Röder, B.; Schnurpfeil, G. Singlet Oxygen Quantum Yields of Different Photosensitizers in Polar Solvents and Micellar Solutions. *J. Porphyrins Phthalocyanines* **1998**, *02*, 145–158.
(112) Costes, S. V.; Daelemans, D.; Cho, E. H.; Dobbin, Z.; Pavlakis, G.; Lockett, S. Automatic and Quantitative Measurement of Protein-Protein Colocalization in Live Cells. *Biophys. J.* **2004**, *86*, 3993–4003.
(113) Kalyanaraman, B.; Darley-Usmar, V.; Davies, K.; Dennery, P.; Forman, H.; Grisham, M.; Mann, G.; Moore, K.; Roberts II, L.; Ischiropoulos, H. Measuring Reactive Oxygen and Nitrogen Species with Fluorescent Probes: Challenges and Limitations. *Free Radic Biol Med.* **2012**, *52*, 1–6.
(114) Li, M. Y.; Cline, C. S.; Koker, E. B.; Carmichael, H. H.; Chingnell, C. F.; Bilski,

P. Quenching of Singlet Molecular Oxygen (1O2) by Azide Anion in Solvent Mixtures. *Photochem. Photobiol.* **2001**, *74*, 760–764.
(115) Yu, Z.; Sun, Q.; Pan, W.; Li, N.; Tang, B. A Near-Infrared Triggered Nanophotosensitizer Inducing Domino Effect on Mitochondrial Reactive Oxygen Species Burst for Cancer Therapy. *ACS Nano* **2015**, *9*, 11064–11074.
(116) Nam, G.; Rangasamy, S.; Ju, H.; Samson, A. A. S.; Song, J. M. Cell Death Mechanistic Study of Photodynamic Therapy against Breast Cancer Cells Utilizing Liposomal Delivery of 5,10,15,20-Tetrakis(Benzo[b]Thiophene) Porphyrin. *J. Photochem. Photobiol. B Biol.* **2017**, *166*, 116–125.
(117) Rizvi, I.; Anbil, S.; Alagic, N.; Celli, J. P.; Zheng, L. Z.; Palanisami, A.; Glidden, M. D.; Pogue, B. W.; Hasan, T. PDT Dose Parameters Impact Tumoricidal Durability and Cell Death Pathways in a 3D Ovarian Cancer Model. *Photochem. Photobiol.* **2013**, *89*, 942–952.
(118) Mac, J. T.; Nuñez, V.; Burns, J. M.; Guerrero, Y. A.; Vullev, V. I.; Anvari, B. Erythrocyte-Derived Nano-Probes Functionalized with Antibodies for Targeted near Infrared Fluorescence Imaging of Cancer Cells. *Biomed. Opt. Express* **2016**, *7*, 1311.
(119) Sibrian-Vazquez, M.; Escobedo, J. O.; Lowry, M.; Fronczek, F. R.; Strongin, R. M. Field Effects Induce Bathochromic Shifts in Xanthene Dyes. *J. Am. Chem. Soc.* **2012**, *134*, 10502–10508.
(120) Philip, R.; Penzkofer, A.; Baumler, W.; Szeimies, R. M.; Abels, C. Absorption and Fluorescence Spectroscopic Investigation of Indocyanine Green. *J. Photochem. Photobiol. AChemistry* **1996**, *96*, 137–148.
(121) Tan, X.; Luo, S.; Long, L.; Wang, Y.; Wang, D.; Fang, S.; Ouyang, Q.; Su, Y.; Cheng, T.; Shi, C. Structure-Guided Design and Synthesis of a Mitochondria-Targeting Near-Infrared Fluorophore with Multimodal Therapeutic Activities. *Adv. Mater.* **2017**, *29*, 1–9.
(122) Guo, R.; Peng, H.; Tian, Y.; Shen, S.; Yang, W. Mitochondria-Targeting Magnetic Composite Nanoparticles for Enhanced Phototherapy of Cancer. *Small* **2016**, *12*, 4541–4552.
(123) Kessel, D.; Luo, Y. Intracellular Sites of Photodamage as a Factor in Apoptotic Cell Death. *J. Porphyr. Phthalocyanines* **2001**, *5*, 181–184.
(124) Reiners Jr, J. J.; Caruso, J. A.; Mathieu, P.; Chelladurai, B.; Yin, X.-M.; Kessel, D. Release of Cytochrome c and Activation of Pro-Caspase-9 Following Lysosomal Photodamage Involves Bid Cleavage. *Cell Death Differ.* **2002**, *9*, 934–944.
(125) Wang, X. The Expanding Role of Mitochondria in Apoptosis. *Gene Dev* **2001**, *15*, 2922–2933.
(126) Wang, Y.; Tjandra, N. Structural Insights of TBid, the Caspase-8-Activated Bid, and Its BH3 Domain. *J. Biol. Chem.* **2013**, *288*, 35840–35851.
(127) Epand, R. F.; Martinou, J.-C.; Fornallaz-Mulhauser, M.; Hughes, D. W.; Epand, R. M. The Apoptotic Protein TBid Promotes Leakage by Altering Membrane Curvature. *J. Biol. Chem.* **2002**, *277*, 32632–32639.
(128) Grinberg, M.; Sarig, R.; Zaltsman, Y.; Frumkin, D.; Grammatikakis, N.; Reuveny, E.; Gross, A. TBID Homooligomerizes in the Mitochondrial Membrane to Induce

Apoptosis. *J. Biol. Chem.* **2002**, *277*, 12237–12245.
(129) Lovell, J. F.; Billen, L. P.; Bindner, S.; Shamas-Din, A.; Fradin, C.; Leber, B.; Andrews, D. W. Membrane Binding by TBid Initiates an Ordered Series of Events Culminating in Membrane Permeabilization by Bax. *Cell* **2008**, *135*, 1074–1084.
(130) Ott, M.; Norberg, E.; Zhivotovsky, B.; Orrenius, S. Mitochondrial Targeting of TBid/Bax: A Role for the TOM Complex? *Cell Death Differ.* **2009**, *16*, 1075–1082.
(131) Bogner, C.; Leber, B.; Andrews, D. W. Apoptosis: Embedded in Membranes. *Curr. Opin. Cell Biol.* **2010**, *22*, 845–851.
(132) Kim, H.; Tu, H.-C.; Ren, D.; Takeuchi, O.; Jeffers, J. R.; Zambetti, G. P.; Hsieh, J. J.-D.; Cheng, E. H.-Y. Stepwise Activation of BAX and BAK by TBID, BIM, and PUMA Initiates Mitochondrial Apoptosis. *Mol. Cell* **2009**, *36*, 487–499.
(133) Ai, X.; Mu, J.; Xing, B. Recent Advances of Light-Mediated Theranostics. *Theranostics* **2016**, *6*, 2439–2457.
(134) Kim, H.; Beack, S.; Han, S.; Shin, M.; Lee, T.; Park, Y.; Kim, K. S.; Yetisen, A. K.; Yun, S. H.; Kwon, W.; *et al.* Multifunctional Photonic Nanomaterials for Diagnostic, Therapeutic, and Theranostic Applications. *Adv. Mater.* **2018**, *30*, 1701460 (1-33).
(135) Jiang, X. M.; Wang, L. M.; Wang, J.; Chen, C. Y. Gold Nanomaterials: Preparation, Chemical Modification, Biomedical Applications and Potential Risk Assessment. *Appl. Biochem. Biotechnol.* **2012**, *166*, 1533–1551.
(136) Liu, Y.; Zhao, Y.; Sun, B.; Chen, C. Understanding the Toxicity of Carbon Nanotubes. *Acc. Chem. Res.* **2013**, *46*, 702–713.
(137) Oldenborg, P.-A.; Zheleznyak, A.; Fang, Y.-F.; Lagenaur, C. F.; Gresham, H. D.; Lindberg, F. P. Role of CD47 as a Marker of Self on Red Blood Cells. *Science.* **2000**, *288*, 2051–2054.
(138) Hwang, Y.; Yoon, H.; Choe, K.; Ahn, J.; Jung, J. H.; Park, J.-H.; Kim, P. In Vivo Cellular-Level Real-Time Pharmacokinetic Imaging of Free-Form and Liposomal Indocyanine Green in Liver. *Biomed. Opt. Express* **2017**, *8*, 4706–4716.
(139) Ren, H.; Liu, J.; Li, Y.; Wang, H.; Ge, S.; Yuan, A.; Hu, Y.; Wu, J. Oxygen Self-Enriched Nanoparticles Functionalized with Erythrocyte Membranes for Long Circulation and Enhanced Phototherapy. *Acta Biomater.* **2017**, *59*, 269–282.
(140) Holschneider, C. H.; Berek, J. S. Ovarian Cancer: Epidemiology, Biology, and Prognostic Factors. *Semin. Surg. Oncol.* **2000**, *19*, 3–10.
(141) American Cancer Society. Cancer Facts & Figures 2018. **2018**.
(142) Jemal, A.; Siegel, R.; Ward, E.; Hao, Y.; Xu, J.; Murray, T.; Thun, M. J. Cancer Statistics, 2008. *CA. Cancer J. Clin.* **2008**, *58*, 71–96.
(143) Bristow, R. E.; Tomacruz, R. S.; Armstrong, D. K.; Trimble, E. L.; Montz, F. J. Survival Effect of Maximal Cytoreductive Surgery for Advanced Ovarian Carcinoma during the Platinum Era: A Meta-Analysis. *J. Clin. Oncol.* **2002**, *20*, 1248–1259.
(144) Vergote, I.; Van Gorp, T.; Amant, F.; Leunen, K.; Neven, P.; Berteloot, P. Timing of Debulking Surgery in Advanced Ovarian Cancer. *Int. J. Gynecol. Cancer* **2008**, *18*, 11–19.

(145) Zivanovic, O.; Aldini, A.; Carlson, J. W.; Chi, D. S. Advanced Cytoreductive Surgery: American Perspective. *Gynecol. Oncol.* **2009**, *114*, S3–S9.
(146) Van Dam, G. M.; Themelis, G.; Crane, L. M. A.; Harlaar, N. J.; Pleijhuis, R. G.; Kelder, W.; Sarantopoulos, A.; De Jong, J. S.; Arts, H. J. G.; Van Der Zee, A. G. J.; *et al.* Intraoperative Tumor-Specific Fluorescence Imaging in Ovarian Cancer by Folate Receptor-α Targeting: First in-Human Results. *Nat. Med.* **2011**, *17*, 1315–1319.
(147) Sevick-Muraca, E. M.; Houston, J. P.; Gurfinkel, M. Fluorescence-Enhanced, near Infrared Diagnostic Imaging with Contrast Agents. *Curr. Opin. Chem. Biol.* **2002**, *6*, 642–650.
(148) Pansare, V.; Hejazi, S.; Faenza, W.; Prud'homme, R. K. Review of Long-Wavelength Optical and NIR Imaging Materials: Contrast Agents, Fluorophores and Multifunctional Nano Carriers. *Chem Mater.* **2012**, *24*, 812–827.
(149) Cho, K. R.; Shih, I.-M. Ovarian Cancer. *Annu. Rev. Pathol.* **2009**, *4*, 287–313.
(150) Nandy, S.; Mostafa, A.; Kumavor, P. D.; Sanders, M.; Brewer, M.; Zhu, Q. Characterizing Optical Properties and Spatial Heterogeneity of Human Ovarian Tissue Using Spatial Frequency Domain Imaging. *J. Biomed. Opt.* **2016**, *21*, 101402.
(151) Zhang, Y. M.; Shi, R.; Hou, J. C.; Liu, Z. R.; Cui, Z. L.; Li, Y.; Wu, D.; Shi, Y.; Shen, Z. Y. Liver Tumor Boundaries Identified Intraoperatively Using Real-Time Indocyanine Green Fluorescence Imaging. *J. Cancer Res. Clin. Oncol.* **2017**, *143*, 51–58.
(152) Tummers, Q. R. J. G.; Hoogstins, C. E. S.; Peters, A. A. W.; De Kroon, C. D.; Trimbos, J. B. M. Z.; Van De Velde, C. J. H.; Frangioni, J. V.; Vahrmeijer, A. L.; Gaarenstroom, K. N. The Value of Intraoperative Near-Infrared Fluorescence Imaging Based on Enhanced Permeability and Retention of Indocyanine Green: Feasibility and False-Positives in Ovarian Cancer. *PLoS One* **2015**, *10*, 1–12.
(153) Chijiiwa, K.; Watanabe, M.; Nakano, K.; Noshiro, H.; Tanaka, M. Biliary Indocyanine Green Excretion as a Predictor of Hepatic Adenosine Triphosphate Levels in Patients with Obstructive Jaundice. *Am. J. Surg.* **2000**, *179*, 161–166.
(154) Bahmani, B.; Lytle, C. Y.; Walker, A. M.; Gupta, S.; Vullev, V. I.; Anvari, B. Effects of Nanoencapsulation and PEGylation on Biodistribution of Indocyanine Green in Healthy Mice: Quantitative Fluorescence Imaging and Analysis of Organs. *Int. J. Nanomedicine* **2013**, *8*, 1609–1620.
(155) Yaseen, M. A.; Yu, J.; Wong, M. S.; Anvari, B. In-Vivo Fluorescence Imaging of Mammalian Organs Using Charge-Assembled Mesocapsule Constructs Containing Indocyanine Green. *Opt. Express* **2008**, *16*, 20577–20587.
(156) Burns, J. M.; Vankayala, R.; Mac, J. T.; Anvari, B. Erythrocyte-Derived Theranostic Nanoplatforms for Near Infrared Fluorescence Imaging and Photodestruction of Tumors. *ACS Appl. Mater. Interfaces* **2018**, *10*, 27621–27630.
(157) Sun, J.; Miller, J. P.; Akers, W. J.; Sun, J.; Miller, J. P.; Hathi, D.; Zhou, H.; Achilefu, S.; Shokeen, M. Enhancing in Vivo Tumor Boundary Delineation with Structured Illumination Fluorescence Molecular Imaging and Spatial Gradient Mapping. *J. Biomed. Opt.* **2016**, *21*, 080502.

(158) Neil, M. A. A.; Juskaitis, R.; Wilson, T. Method of Obtaining Optical Sectioning by Using Structured Light in a Conventional Microscope. *Opt. Lett.* **1997**, *22*, 1905–1907.
(159) Haskell, R. C.; Svaasand, L. O.; Tsay, T. T.; Feng, T. C.; McAdams, M. S.; Tromberg, B. J. Boundary Conditions for the Diffusion Equation in Radiative Transfer. *J. Opt. Soc. Am. A* **1994**, *11*, 2727–2741.
(160) Ebert, B.; Riefke, B.; Sukowski, U.; Licha, K. Cyanine Dyes as Contrast Agents for Near-Infrared Imaging in Vivo: Acute Tolerance, Pharmacokinetics, and Fluorescence Imaging. *J. Biomed. Opt.* **2011**, *16*, 066003.
(161) Aernouts, B.; Erkinbaev, C.; Watté, R.; Van Beers, R.; Do Trong, N. N.; Nicolai, B.; Saeys, W. Estimation of Bulk Optical Properties of Turbid Media from Hyperspectral Scatter Imaging Measurements: Metamodeling Approach. *Opt. Express* **2015**, *23*, 26049.
(162) Tang, J. C.; Partono, A.; Anvari, B. Near-Infrared-Fluorescent Erythrocyte-Mimicking Particles: Physical and Optical Characteristics. *IEEE Trans. Biomed. Eng.* **2018**.
(163) Marquez, G.; Wang, L. V; Lin, S.-P.; Schwartz, J. A.; Thomsen, S. L. Anisotropy in the Absorption and Scattering Spectra of Chicken Breast Tissue. *Appl. Opt.* **1998**, *37*, 798–804.
(164) O'Sullivan, T. D.; Cerussi, A. E.; Cuccia, D. J.; Tromberg, B. J. Diffuse Optical Imaging Using Spatially and Temporally Modulated Light. *J. Biomed. Opt.* **2012**, *17*, 071311.
(165) Li, M.; Al-jamal, K. T.; Kostarelos, K.; Reineke, J. Physiologically Based Pharmacokinetic Modeling of Nanoparticles. *ACS Nano* **2010**, *4*, 6303–6317.
(166) Lukas, G.; Brindle, S. D.; Greengard, P. The Route of Absorption of Intraperitoneally Administered Compounds. *J. Pharmacol. Exp. Ther.* **1971**, *178*, 562–566.
(167) Moghimi, S. M.; Bonnemain, B. Subcutaneous and Intravenous Delivery of Diagnostic Agents to the Lymphatic System: Applications in Lymphoscintigraphy and Indirect Lymphography. *Adv. Drug Deliv. Rev.* **1999**, *37*, 295–312.
(168) Kwon, S.; Davies-Venn, C.; Sevick-Muraca, E. M. In Vivo Dynamic Imaging of Intestinal Motions Using Diet-Related Autofluorescence. *J. Neurogastroenterol. Motil.* **2012**, *24*, 494–497.
(169) Cherrick, G. R.; Stein, S. W.; Leevy, C. M.; Davidson, C. S. Indocyanine Green : Observations on Its Physical Properties, Plasma Decay, and Hepatic Extraction. *J. Clin. Invest.* **1959**, *39*, 592–600.
(170) Yang, B.; Tunnell, J. W. Real-Time Absorption Reduced Surface Fluorescence Imaging. *J. Biomed. Opt.* **2014**, *19*, 090505.
(171) Parsa, P.; Jacques, S. L.; Nishioka, N. S. Optical Properties of Rat Liver between 350 and 2200 Nm. *Appl. Opt.* **1989**, *28*, 2325–2330.
(172) Zhang, Y. N.; Poon, W.; Tavares, A. J.; McGilvray, I. D.; Chan, W. C. W. Nanoparticle–liver Interactions: Cellular Uptake and Hepatobiliary Elimination. *J. Control. Release* **2016**, *240*, 332–348.
(173) Wisse, E.; Braet, F.; Luo, D.; De Zanger, R.; Jans, D.; Crabbé, E.; Vermoesen, A.

Structure and Function of Sinusoidal Cells in the Liver. *Toxicol. Pathol.* **1996**, *24*, 100–111.
(174) Janeway, C. A.; Travers, P.; Walport, M.; Shlomchik, M. J. *The Front Line of Host Defense*; 5th editio.; Garland Science: New York, 2001.
(175) Desilets, J.; Lejeune, A.; Mercer, J.; Gicquaud, C. Nanoerythrosomes, a New Derivative of Erythrocyte Ghost: IV. Fate of Reinjected Nanoerythrosomes. *Anticancer Res.* **2001**, *21*, 1741–1747.